

The dark Universe

Matthias Bartelmann*

*Institut für Theoretische Astrophysik, Zentrum für Astronomie der Universität Heidelberg,
Albert-Überle-Straße 2, 69120 Heidelberg, Germany*

(Published 18 February 2010)

For a few years now, cosmology has a standard model. By this term, we mean a consistent theoretical background which is at the same time simple and broad enough to offer coherent explanations for the vast majority of cosmological phenomena. This review will briefly summarize the cosmological model, then proceed to discuss what we know from observations about the evolution of the Universe and its contents and what we conclude about the origin and the future of the Universe and the structures it contains.

DOI: [10.1103/RevModPhys.82.331](https://doi.org/10.1103/RevModPhys.82.331)

PACS number(s): 98.80.-k, 95.35.+d, 95.36.+x

CONTENTS

I. The Cosmological Standard Model	332	4. Summary of results	347
A. Historical outline	332	V. The Matter Density in the Universe	347
B. Friedmann models	333	A. Mass in galaxies	347
1. The metric	333	1. Stars	347
2. Redshift and expansion	333	2. Galaxies	348
3. The radiation-dominated phase	334	3. The galaxy population	348
4. Age, distances, and horizons	335	B. Mass in galaxy clusters	349
C. Structures	335	1. Kinematic masses	349
1. Structure growth	335	2. Mass in the hot intracluster gas	349
2. The power spectrum	336	3. Alternative cluster mass estimates	350
3. Nonlinear evolution	337	C. Mass density from cluster evolution	351
II. The Age of the Universe	337	D. Conclusions	351
A. Nuclear cosmochronology	337	VI. The Cosmic Microwave Background	352
1. The age of the Earth	337	A. The isotropic CMB	352
2. The age of the Galaxy	338	1. Thermal history of the Universe	352
B. Stellar ages	339	2. Mean properties of the CMB	352
C. Cooling of white dwarfs	340	3. Decoupling of the CMB	353
D. Summary	340	B. Structures in the CMB	353
III. The Hubble Constant	340	1. The dipole	353
A. Hubble constant from Hubble's law	340	2. Expected amplitude of CMB fluctuations	354
1. Hubble's law	340	3. Expected CMB fluctuations	354
2. The distance ladder	341	4. CMB polarization	355
3. The HST key project	342	5. The CMB power spectrum	355
B. Gravitational lensing	342	6. Secondary anisotropies and foregrounds	356
C. Summary	343	7. Measurements of the CMB	356
IV. Big-Bang Nucleosynthesis	343	VII. Cosmic Structures	357
A. The origin and abundance of ^4He	343	A. Quantifying structures	357
1. Elementary considerations	343	1. Introduction	357
2. The Gamow criterion	344	2. Measuring the correlation function	358
3. Elements produced	344	3. Measuring the power spectrum	358
4. Helium abundance	345	4. Biasing	359
5. Expected abundances and abundance trends	345	5. Redshift-space distortions	359
B. Observed element abundances	346	6. Baryonic acoustic oscillations	360
1. Principles	346	B. Measurements and results	360
2. Evolutionary corrections	346	1. The power spectrum	360
3. Specific results	346	VIII. Cosmological Weak Lensing	361
		A. Cosmological light deflection	361
		1. Deflection angle, convergence, and shear	361
		2. Power spectra	362
		3. Correlation functions	363
		B. Cosmic-shear measurements	363
		1. Typical scales and requirements	363

*mbartelmann@ita.uni-heidelberg.de

2. Ellipticity measurements	364
3. Results	365
IX. Supernovae of Type Ia	365
A. Standard candles and distances	365
1. The principle	365
2. Requirements and degeneracies	366
B. Supernovae	367
1. Types and classification	367
2. Observations	368
3. Potential problems	370
X. The Normalization of the Power Spectrum	370
A. Introduction	370
B. Fluctuations in the CMB	371
1. The large-scale fluctuation amplitude	371
2. Translation to σ_8	371
C. Cosmological weak lensing	372
D. Galaxy clusters	373
1. The mass function	373
2. What is a cluster's mass?	373
E. The Lyman- α forest	375
XI. Inflation and Dark Energy	375
A. Cosmological inflation	375
1. Motivation	375
2. The idea of inflation	376
3. Slow roll, structure formation, and observational constraints	376
B. Dark energy	377
1. Motivation	377
2. Observational constraints?	378
Acknowledgments	379
References	379

I. THE COSMOLOGICAL STANDARD MODEL

A. Historical outline

This review will not follow the historical sequence of discoveries but rather present the arguments in perhaps a more logical order than history has allowed. We begin with a brief and necessarily fragmental historical outline.

Modern cosmology began in 1915 with Einstein's theory of general relativity, from which Friedmann in 1922 derived the homogeneous and isotropic class of world models which to this date forms the foundation of the cosmological standard model. His discovery that static world models were impossible confirmed Einstein in his introduction of the cosmological constant, which he abandoned in the 1930s after Slipher, Hubble, and Humason had discovered the cosmic expansion. Earlier, Lemaître had speculated about a primordial fireball which seemed the natural starting point of an expanding universe.

First evidence for dark matter was found by Zwicky in galaxy clusters and by Babcock and Oort in galaxies between 1933 and 1940. In 1946, Lifshitz worked out relativistic perturbation theory and started applying it to the linear growth of cosmic structures. In the late 1940s, Gamow, Alpher, and Herman worked out how nuclear fusion may have proceeded in the early Universe and

predicted a cosmic radiation background with a temperature of a few kelvin.

The cosmic microwave background (CMB) was discovered by Penzias and Wilson and explained by Dicke and collaborators in 1965. In 1970, Peebles and Yu as well as Sunyaev and Zel'dovich independently predicted structures in the CMB and found that they should have relative amplitudes near 10^{-4} , where subsequent searches did not find them. Peebles suggested in 1982 that a lower CMB fluctuation level could be explained if the dark matter could not interact with light. It was quickly realized by means of the numerical simulations by Davis, Efstathiou, Frenk, and White that cosmological structure formation could be explained within the emerging paradigm of cold dark matter (CDM). This paradigm experienced further strong support when temperature fluctuations at the revised level were finally found in the CMB with the Cosmic Background Explorer (COBE) satellite in 1992.

It was suggested by Guth in 1981 that a phase of inflationary expansion could solve the horizon and flatness problems of Friedmann cosmology. Mukhanov and Chibisov immediately saw that inflated quantum fluctuations could be the origin of cosmic structures. At least in simple scenarios, inflation requires a spatially flat universe and thus a total energy density equal to its critical value, but it became obvious that matter alone cannot be as dense. The difference was tentatively attributed to the cosmological constant, which was confirmed by several groups in the late 1990s through the accelerated cosmic expansion inferred from type-Ia supernovae. The cosmological standard model could be considered complete when recent measurements of the CMB temperature fluctuations confirmed that the Universe is spatially flat.

Modern cosmology is thoroughly described in many textbooks. To mention a few, see Padmanabhan (1993), Peebles (1993), Peacock (1999), Coles and Lucchin (2002), Dodelson (2003), Weinberg (2008), and the textbook on the CMB (Durrer, 2008).

This review is structured as follows. The Introduction proceeds by summarizing the framework of the Friedmann models in Sec. I.B and the growth of cosmic structures in Sec. I.C. Section II describes what we know about the age of the Universe from its ingredients through nuclear cosmochronology (Sec. II.A), stars (Sec. II.B), and the cooling of white dwarfs (Sec. II.C). In Sec. III, measurements of the Hubble constant from Hubble's law (Sec. III.A) and gravitational lensing (Sec. III.B) are reviewed. Big-Bang nucleosynthesis is the subject of Sec. IV, with sections on the production of light elements (Sec. IV.A) and the observed element abundances (Sec. IV.B). Section V gives an overview of the matter density in the Universe, as constrained by galaxies (Sec. V.A), galaxy clusters as individual objects (Sec. V.B), and as an evolving population (Sec. V.C). Section VI on the cosmic microwave background begins with the isotropic CMB (Sec. VI.A) and continues with its fluctuations (Sec. VI.B). Cosmic structures are reviewed in Sec. VII, which starts with the quantification of struc-

tures (Sec. VII.A) and continues with their measurement and results obtained (Sec. VII.B). Section VIII on cosmological weak lensing follows, in which gravitational light deflection is first summarized (Sec. VIII.A) before measurements are described (Sec. VIII.B). Supernovae of type Ia are the subject of Sec. IX, where the principles of their cosmological application (Sec. IX.A), the reasons thereof, and the observational results are described (Sec. IX.B). Section X on the normalization of the matter-fluctuation power spectrum begins with an introduction (Sec. X.A) and continues describing constraints from CMB fluctuations (Sec. X.B), cosmological weak lensing (Sec. X.C), galaxy clusters (Sec. X.D), and the Lyman- α forest (Sec. X.E). Section XI discusses the motivation and the evidence for cosmological inflation (Sec. XI.A) and ends with remarks on dark energy (Sec. XI.B).

B. Friedmann models

1. The metric

Cosmology studies the physical properties of the Universe as a whole. The only one of the four known interactions which can play a role on cosmic length scales is gravity. Electromagnetism, the only other interaction with infinite range, has sources of opposite charge which tend to shield each other on comparatively very small scales. Cosmic magnetic fields can perhaps reach coherence lengths on the order of ≥ 10 Mpc, but they are far too weak for them to be important for the cosmic evolution. The weak and strong interactions, of course, have microscopic range and must thus be unimportant for cosmology as a whole.

The best current theory of gravity is Einstein’s theory of general relativity, which relates the geometry of a four-dimensional space-time manifold to its material and energy content. Cosmological models must thus be constructed as solutions of Einstein’s field equations. Symmetry assumptions greatly simplify this process. Guided by observations to be specified later, we assume that the Universe appears approximately identical in all directions of observation; in other words, it is assumed to be isotropic on average. While this assumption is obviously incorrect in our cosmological neighborhood, it holds with increasing precision if observations are averaged on increasingly large scales. The assumption of isotropy can only be valid in a preferred reference frame which is at rest with respect to the mean cosmic motion. The motion of the Earth within this rest frame must be subtracted before any observation can be expected to appear isotropic.

The second assumption asserts that the Universe should appear equally isotropic about any of its points. Then, it is homogeneous. Isotropic and homogeneous solutions for Einstein’s field equations admit the Robertson-Walker metric whose line element is

$$ds^2 = -c^2 dt^2 + a^2(t)[dw^2 + f_K^2(w)(d\theta^2 + \sin^2 \theta d\phi^2)], \tag{1}$$

with the radial coordinate w and the radial function

$$f_K(w) = \begin{cases} K^{-1/2} \sin(K^{1/2}w) & (K > 0) \\ w & (K = 0) \\ |K|^{-1/2} \sinh(|K|^{1/2}w) & (K < 0). \end{cases} \tag{2}$$

The curvature parameter K , which can be positive, negative, or zero, has the dimension of an inverse squared length. The scale factor $a(t)$ isotropically stretches or shrinks the three-dimensional spatial sections of the four-dimensional space-time. The scale factor is commonly normalized to $a_0=1$ at the present time. As usual, the line element ds gives the proper time measured by an observer moving by $(dw, f_K(w)d\theta, f_K(w)\sin \theta d\phi)$ within the *coordinate time* interval dt . For light, $ds=0$.

Observers attached to the coordinate grid (w, θ, ϕ) on the spatial hypersurfaces for constant cosmological time t are called comoving. The cosmic expansion does not change the comoving coordinates \vec{x} , but the physical coordinates $\vec{r}=a\vec{x}$.

2. Redshift and expansion

The changing scale of the Universe causes the cosmological redshift z . The wavelength of light from a distant comoving source seen by a comoving observer changes by the same amount as the Universe changes its scale while the light is traveling. Thus, the emitted and observed wavelengths λ and λ_0 , respectively, are related by

$$\frac{\lambda_0}{\lambda} = \frac{a_0}{a} = \frac{1}{a}, \tag{3}$$

where a is the scale factor at the time of emission. The *relative* wavelength change is the redshift,

$$z \equiv \frac{\lambda_0 - \lambda}{\lambda} = \frac{1}{a} - 1, \tag{4}$$

thus

$$1 + z = a^{-1}, \quad a = (1 + z)^{-1}. \tag{5}$$

When the metric is inserted into Einstein’s field equations, two ordinary differential equations result,

$$\left(\frac{\dot{a}}{a}\right)^2 = \frac{8\pi G}{3}\rho - \frac{Kc^2}{a^2} + \frac{\Lambda c^2}{3}, \tag{6}$$

$$\frac{\ddot{a}}{a} = -\frac{4\pi G}{3}\left(\rho + \frac{3p}{c^2}\right) + \frac{\Lambda c^2}{3}, \tag{7}$$

relating \dot{a} and \ddot{a} to the density ρ , the pressure p , the cosmological constant Λ , and the curvature K . Equation (7) can be eliminated and replaced by

$$\frac{d}{dt}(\rho c^2 a^3) + p \frac{d(a^3)}{dt} = 0, \tag{8}$$

from which the change of ρ with a can be inferred once p is given. Relativistic matter (r , “radiation”) has $p = \rho c^2/3$, while nonrelativistic matter (m , “dust”) is characterized by $\rho c^2 \gg p \approx 0$. Thus

TABLE I. Cosmological parameters obtained from the 5-yr data release of WMAP (Komatsu *et al.*, 2009), without and with the additional constraints imposed by baryonic acoustic oscillations (BAOs) (Sec. VII.A.6) and type-Ia supernovae (SNe) (Sec. IX). The dimensionless Hubble constant h is defined in Eq. (11), the normalization parameter σ_8 in Eq. (267), and the spectral index in Eq. (28). Reionization is discussed in Sec. X.B.2. Note that spatial flatness ($K=0$) was assumed in deriving most of these values, as mentioned in last column.

Parameter	Symbol	WMAP-5		Comment
		Alone	+BAO+SNe (reference)	
CMB temperature	T_{CMB}	2.728 ± 0.004 K		From Fixsen <i>et al.</i> , 1996
Total energy density	Ω_{tot}	$1.099^{+0.100}_{-0.085}$	1.0052 ± 0.0064	
Matter density	Ω_{m0}	0.258 ± 0.03	0.279 ± 0.015	Assuming spatial flatness
Baryon density	Ω_{b0}	0.0441 ± 0.0030	0.0462 ± 0.0015	Here and below
Cosmological constant	$\Omega_{\Lambda 0}$	0.742 ± 0.03	0.721 ± 0.015	
Hubble constant	h	$0.719^{+0.026}_{-0.027}$	0.701 ± 0.013	
Power-spectrum normalization	σ_8	0.796 ± 0.036	0.817 ± 0.026	
Age of the Universe in Gyr	t_0	13.69 ± 0.13	13.73 ± 0.12	
Decoupling redshift	z_{dec}	1087.9 ± 1.2	1088.2 ± 1.1	
Reionization optical depth	τ	0.087 ± 0.017	0.084 ± 0.016	
Spectral index	n_s	$0.963^{+0.014}_{-0.015}$	$0.960^{+0.014}_{-0.013}$	

$$\rho_r \propto a^{-4}, \quad \rho_m \propto a^{-3}. \quad (9)$$

For a model universe containing only matter, radiation, and the cosmological constant, Eq. (6) can be brought into the form

$$H^2 = H_0^2 \left[\frac{\Omega_{r0}}{a^4} + \frac{\Omega_{m0}}{a^3} + \Omega_{\Lambda 0} + \frac{1 - \Omega_{m0} - \Omega_{r0} - \Omega_{\Lambda 0}}{a^2} \right] \\ \equiv H_0^2 E^2(a). \quad (10)$$

This is commonly called Friedmann's equation, in which the relative expansion rate \dot{a}/a is replaced by the Hubble function $H(a)$ whose present value is the Hubble constant $H_0 \equiv H(a_0) = H(1)$, and the matter-energy content is described by the three density parameters Ω_{r0} , Ω_{m0} , and $\Omega_{\Lambda 0}$.

H_0 is often expressed in dimensionless form by

$$h \equiv \frac{H_0}{100 \text{ km s}^{-1} \text{ Mpc}^{-1}}. \quad (11)$$

Since lengths in the Universe are typically measured with respect to the Hubble length, they are often given in units of h^{-1} Mpc. Similarly, luminosities are typically obtained by multiplying fluxes with squared luminosity distances and are thus often given in units of $h^{-2} L_{\odot}$. We avoid this notation where possible in the following and insert $h=0.7$ where appropriate.

The dimensionless parameters Ω_{m0} and Ω_{r0} describe the densities of matter and radiation today in units of the critical densities

$$\rho_{\text{cr}} \equiv \frac{3H^2}{8\pi G}, \quad \rho_{\text{cr}0} \equiv \frac{3H_0^2}{8\pi G}. \quad (12)$$

A Robertson-Walker metric whose scale factor satisfies Friedmann's equation is called a Friedmann-Lemaître-Robertson-Walker metric. The cosmological standard model asserts that the Universe at large is described by such a metric and is thus characterized by the four parameters Ω_{m0} , Ω_{r0} , $\Omega_{\Lambda 0}$, and H_0 . Since the critical density and the densities themselves evolve in time, so do the density parameters.

The remainder of this review article is devoted to answering two essential questions: (1) What are the values of the parameters characterizing Friedmann's equation? (2) How can we understand the *deviations* of the real Universe from a purely homogeneous and isotropic space-time?

Table I, adapted from Komatsu *et al.* (2009), summarizes the most important cosmological parameters and the values adopted below unless stated otherwise.

3. The radiation-dominated phase

It is an empirical fact that the Universe is expanding. Earlier in time, therefore, the scale factor must have been smaller than today, $a < 1$. In principle, it is possible for Friedmann models to never reach a vanishing scale, $a=0$, within finite time into the past. However, a few crucial observational results suffice to rule out such "bouncing" models. This implies that a Universe like ours which is expanding today must have started from $a=0$ a finite time ago; thus, there must have been a big bang.

Equation (10) shows that the radiation density increases like a^{-4} as the scale factor decreases, while the matter density increases with one power of a less. Even though the radiation density is much smaller today than the matter density, there must have been a period in the

early evolution of the Universe when radiation dominated the energy density. The scale factor when both densities were equal is called a_{eq} . This *radiation-dominated era* is very important for several observational aspects of the cosmological standard model. Since the radiation retains the Planckian spectrum which it acquired in the very early Universe in the intense interactions with charged particles, its energy density is fully characterized by its temperature T . As the energy density is proportional to both T^4 and a^{-4} , its temperature falls like $T \propto a^{-1}$.

At the times relevant for our purposes, only photons and neutrinos need to be considered as relativistic species. Since photons are heated by electron-proton annihilation after neutrinos decoupled from the cosmic fluid, the photons are heated above the neutrinos by a factor $(11/4)^{1/3}$, which follows directly from entropy conservation. If T is the temperature of the cosmic microwave background after electron-positron annihilation, the energy densities in the photons and the three neutrino species are

$$\rho_{r,\text{CMB}} = \frac{\pi^2 (kT)^4}{15 (\hbar c)^3}, \quad \rho_{r,\nu} = 3 \times \frac{7}{8} \times \left(\frac{4}{11}\right)^{4/3} \rho_{r,\text{CMB}} \quad (13)$$

or, as long as all neutrino species are relativistic,

$$\rho_r = \rho_{r,\text{CMB}} \left[1 + \frac{21}{8} \left(\frac{4}{11}\right)^{4/3} \right] \approx 1.68 \rho_{r,\text{CMB}}. \quad (14)$$

4. Age, distances, and horizons

Since Friedmann's equation gives the relative expansion rate \dot{a}/a , we can use it to infer the cosmic time,

$$t = \int_0^t dt' = \int_0^{a(t)} \frac{da}{\dot{a}} = \int_0^{a(t)} \frac{da}{aH(a)} = \frac{1}{H_0} \int_0^{a(t)} \frac{da}{aE(a)}, \quad (15)$$

which illustrates that the age scale is the inverse Hubble constant H_0^{-1} . A simple example is given by the Einstein–de Sitter model, which (unrealistically) assumes $\Omega_{m0}=1$, $\Omega_{r0}=0$, and $\Omega_{\Lambda}=0$. Then, from Eq. (10), $E(a)=a^{-3/2}$ and

$$t = \frac{1}{H_0} \int_0^1 \sqrt{a} da = \frac{2}{3H_0}. \quad (16)$$

The cosmic age is $t_0=t(a_0)=t(1)$. The cosmic time and the lookback time t_0-t are shown in Fig. 1 as functions of the redshift.

Distances can be defined in many ways which typically lead to different expressions. The proper distance D_{prop} is the distance measured by the light-travel time, thus

$$dD_{\text{prop}} = c dt \Rightarrow D_{\text{prop}} = \frac{c}{H_0} \int \frac{da}{aE(a)}, \quad (17)$$

where the integral has to be evaluated between the scale factors of emission and observation of the light signal.

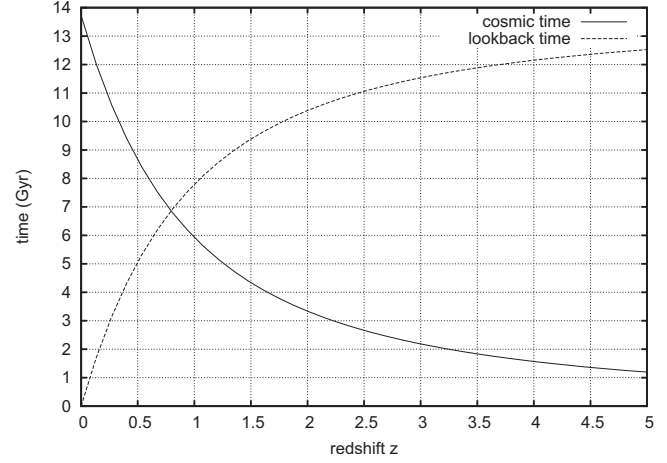


FIG. 1. Cosmic time (solid curve) and lookback time (present age of the Universe minus cosmic time) in Gyr as functions of redshift. Here and below, the parameters labeled as “reference” in Table I are used.

The comoving radial coordinate w is the comoving distance measured along a radial light ray. Since light rays propagate with zero proper time, $ds=0$, this gives

$$dw = \frac{cdt}{a} \Rightarrow w = c \int \frac{da}{a\dot{a}} = \frac{c}{H_0} \int \frac{da}{a^2 E(a)}. \quad (18)$$

The angular-diameter distance D_{ang} is defined such that the same relation as in Euclidean space holds between the physical size of an object and its angular size. It turns out to be

$$D_{\text{ang}}(a) = af_K[w(a)], \quad (19)$$

with $f_K(w)$ given by Eq. (2). The luminosity distance D_{lum} is analogously defined to reproduce the Euclidean relation between the bolometric luminosity of an object and its observed flux. This results in

$$D_{\text{lum}}(a) = \frac{D_{\text{ang}}(a)}{a^2} = \frac{f_K[w(a)]}{a}. \quad (20)$$

Figure 2 shows the angular diameter and the proper distance as functions of redshift.

These distance measures rapidly diverge for scale factors $a < 1$. For small distances, i.e., for $a \approx 1$, they all reproduce the linear relation

$$D(z) = cz/H_0. \quad (21)$$

Since time is finite in a universe with a big bang, any particle can only be influenced by and can only influence events within finite regions, called *horizons*. Several different definitions of horizons exist. They are typically characterized by some speed, e.g., the light speed, times the inverse Hubble function which sets the time scale.

C. Structures

1. Structure growth

The hierarchy of cosmic structures is assumed to have grown from primordial seed fluctuations in the process

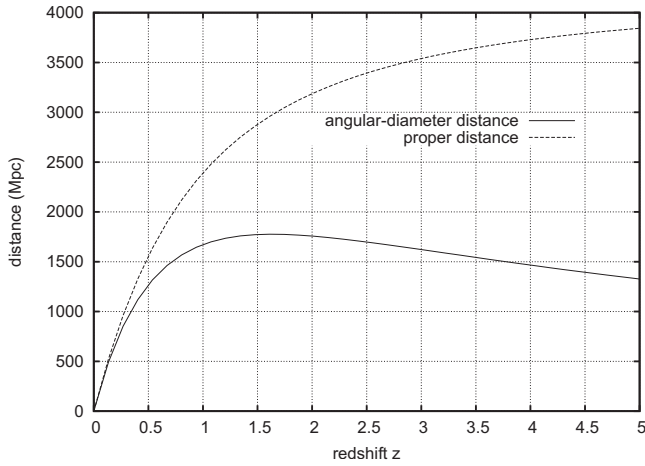


FIG. 2. Angular-diameter distance (solid curve) and proper distance in Mpc as functions of redshift.

of gravitational collapse: overdense regions attract material and grow. They are described by the density contrast $\delta(\vec{x}, t)$ as a function of the comoving coordinates \vec{x} , which is the density fluctuation relative to the mean density $\bar{\rho}(t)$,

$$\delta(\vec{x}, t) \equiv \frac{\rho(\vec{x}, t) - \bar{\rho}(t)}{\bar{\rho}(t)}. \quad (22)$$

Linear perturbation theory shows that, during the matter-dominated era, the density contrast δ of subhorizon perturbations is described by the second-order differential equation

$$\ddot{\delta} + 2H\dot{\delta} - 4\pi G\bar{\rho}\delta = 0 \quad (23)$$

if the dark matter is cold, i.e., if dark-matter flows have negligible velocity dispersion. Equation (23) has two solutions, one growing and one decaying. While the latter is irrelevant for structure growth, the growing mode is described by the growth factor $D_+(a)$, defined such that the density contrast at the scale factor a is related to the density contrast today δ_0 by $\delta(a) = \delta_0 D_+(a)$. In most cases of practical relevance, the growth factor is accurately described by

$$D_+(a) = G(a)/G(1) \quad (24)$$

with the fitting formula

$$G(a) \equiv a\Omega_m \left[\Omega_m^{4/7} - \Omega_\Lambda + \left(1 + \frac{\Omega_m}{2} \right) \left(1 + \frac{\Omega_\Lambda}{70} \right) \right]^{-1}, \quad (25)$$

where the density parameters have to be evaluated at the scale factor a . For a standard cosmological model, Eq. (25) deviates from the accurate solution by $\leq 0.2\%$ for $a \in [0.01, 1]$. The linear growth factor is shown in Fig. 3 together with the fractional cosmic age t/t_0 .

An important length scale for cosmic structure growth is set by the horizon size at the end of the radiation-dominated phase. Structures smaller than that became causally connected while radiation was still dominating.

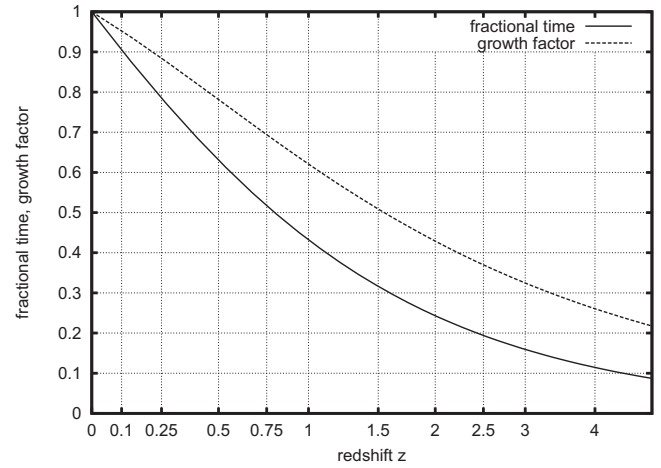


FIG. 3. Fractional cosmic age t/t_0 (solid curve) and structure growth as functions of redshift.

The fast expansion due to the radiation density inhibited further growth of such structures until the matter density started dominating. Small structures are thus suppressed compared to large structures, which became causally connected only after radiation domination. The horizon radius w_{eq} at the end of the radiation-dominated era thus separates larger structures which could grow without inhibition from smaller structures which were suppressed during radiation domination. In comoving coordinates,

$$w_{\text{eq}} = 2(\sqrt{2} - 1) \frac{c}{H_0} \left(\frac{a_{\text{eq}}}{\Omega_{m0}} \right)^{1/2}. \quad (26)$$

2. The power spectrum

It is physically plausible that the density contrast in the Universe is a Gaussian random field, i.e., that the probability for finding a density contrast between δ and $\delta + d\delta$ is given by a Gaussian distribution. The principal reason for this is the central limit theorem. A Gaussian random process is characterized by two numbers, the mean and the variance. By construction, the mean of the density contrast vanishes, such that the variance defines it completely.

In linear approximation, density perturbations grow in place, as Eq. (23) shows because the density contrast at one comoving position \vec{x} does not depend on the density contrast at another. As long as structures evolve linearly, their scale will be preserved, which implies that it is advantageous to study structure growth in Fourier rather than real space. The variance of the density contrast $\hat{\delta}(\vec{k})$ at the comoving wave vector \vec{k} in Fourier space is called the power spectrum

$$\langle \hat{\delta}(\vec{k}) \hat{\delta}^*(\vec{k}') \rangle \equiv (2\pi)^3 P_\delta(k) \delta_D(\vec{k} - \vec{k}'), \quad (27)$$

where the Dirac function δ_D ensures that modes with different wave vectors are independent.

Once the power spectrum is known, the statistical properties of the linear density contrast are completely

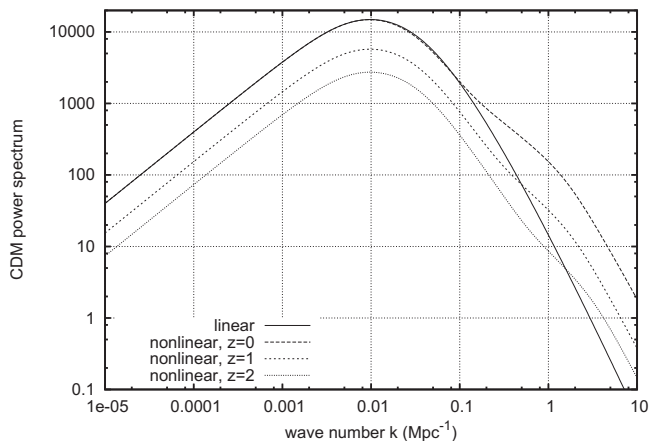


FIG. 4. Linearly and nonlinearly evolved CDM power spectra. The linear CDM spectrum is shown for $a=1$ and scales like $D_{\mp}^2(a)$.

specified. It is a remarkable fact that two simple assumptions about the nature of the cosmic structures and the dark matter constrain the shape of $P_{\delta}(k)$ completely. If the rms mass fluctuation enclosed by the horizon is independent of time and if the dark matter is cold, the power spectrum will behave as

$$P_{\delta}(k) \propto \begin{cases} k^{n_s} & (k \ll k_{\text{eq}}) \\ k^{n_s-4} & (k \gg k_{\text{eq}}), \end{cases} \quad (28)$$

with the spectral index $n_s=1$ (Harrison, 1970; Peebles and Yu, 1970; Zel'dovich, 1972; Peebles, 1982; Weinberg, 2008). The comoving wave number $k_{\text{eq}}=0.01 \text{ Mpc}^{-1}$ of the peak location in the power spectrum is set by the comoving horizon radius at matter-radiation equality w_{eq} given in Eq. (26). The steep decline for structures smaller than w_{eq} reflects the suppression of structure growth during radiation domination. Figure 4 shows the linearly and the nonlinearly evolved power spectra of CDM.

3. Nonlinear evolution

As the density contrast approaches unity, its evolution becomes nonlinear. In the course of nonlinear evolution, overdensities contract, causing matter to flow from larger to smaller scales. Power in the density-fluctuation field is thus transported toward smaller modes or toward larger wave numbers k . This *mode coupling* process deforms the power spectrum on small scales, i.e., for large k . Detailed studies of the nonlinear evolution of cosmic structures require numerical simulations, which need to cover large scales and to resolve small scales well at the same time. Much progress has been achieved in this field within the last two decades due to the fortunate combination of increasing computer power with highly sophisticated numerical algorithms, such as particle-mesh and tree codes, and adaptive mesh refinement techniques (Efstathiou *et al.*, 1985; Barnes and Hut, 1986; Hockney and Eastwood, 1988; Springel and Hernquist, 2002; Monaghan, 2005).

The onset of nonlinear evolution can be described by

the so-called *Zel'dovich approximation*, which approximately describes particle trajectories (Zel'dovich, 1970). Although the Zel'dovich approximation breaks down as the nonlinear evolution proceeds, it is remarkable for two applications. First, it allows a computation of the shapes of collapsing dark-matter structures and arrives at the conclusion that the collapse must be anisotropic, leading to the formation of sheets and filaments (Doroshkevich, 1970). Filamentary structures thus appear as a natural consequence of gravitational collapse in a Gaussian random field. Second, it provides an explanation for the origin of the angular momentum of cosmic structures.

II. THE AGE OF THE UNIVERSE

A. Nuclear cosmochronology

1. The age of the Earth

How old is the Universe? We have no direct way to measure how long ago the Big Bang happened, but there are various ways to set lower limits to the age of the Universe. They are all based on the same principle: since the Universe cannot be younger than any of its parts, it must be older than the oldest objects it contains. Three methods for age determination have been developed. One is based on the radioactive decay of long-lived isotopes, another constrains the age of globular clusters, and the third is based on the age of white dwarfs.

Nuclear cosmochronology compares the measured abundances of certain long-lived radioactive isotopes with their initial abundances, which are eliminated by comparing abundances in different probes.

To give a specific example, consider the two uranium isotopes ^{235}U and ^{238}U . They both decay into stable lead isotopes, $^{235}\text{U} \rightarrow ^{207}\text{Pb}$ through the actinium series and $^{238}\text{U} \rightarrow ^{206}\text{Pb}$ through the radium series. The abundance of any of these two lead isotopes is the sum of the initial abundance plus the amount produced by the uranium decay, e.g.,

$$N_{207} = N_{207,0} + N_{235}(e^{\lambda_{235}t} - 1) \quad (29)$$

for ^{207}Pb , where N_{235} is the abundance of ^{235}U nuclei today. A similar equation with 235 replaced by 238 and 207 replaced by 206 holds for the decay of ^{238}U to ^{206}Pb . The decay constants for the two uranium isotopes are measured as

$$\lambda_{235} = (1.015 \text{ Gyr})^{-1}, \quad \lambda_{238} = (6.45 \text{ Gyr})^{-1}. \quad (30)$$

The idea is now that ores on Earth or meteorites formed during a period very short compared to the age of the Earth t_e , so that their abundances can be assumed to have been locked up instantaneously and simultaneously a time t_e ago. Chemical fractionation has given different abundances to different samples but could not distinguish between different isotopes of the same element. Thus, we expect different samples to show differ-

ent isotope *abundances*, but identical *abundance ratios* between different isotopes.

The unstable lead isotope ^{204}Pb has no long-lived parents and is therefore a measure for the primordial lead abundance. Thus, the abundance ratios between ^{206}Pb and ^{207}Pb to ^{204}Pb calibrate the abundances in different samples. Suppose we have two independent samples a and b , in which the abundance ratios

$$R_{206} \equiv N_{206}/N_{204} \quad \text{and} \quad R_{207} \equiv N_{207}/N_{204} \quad (31)$$

are measured. They are given by

$$R_i = R_{i,0} + \frac{N_j}{N_{204}} (e^{\lambda_j t_e} - 1), \quad (32)$$

with $(i,j)=(206,238)$ or $(207,235)$. The present lead abundance ratios $R_{206,0}$ and $R_{207,0}$ should be the same in the two samples and cancel when the difference between the ratios in the two samples is taken. Then, the ratio of differences can be written as

$$\frac{R_{207}^a - R_{207}^b}{R_{206}^a - R_{206}^b} = \frac{N_{235} e^{\lambda_{235} t_e} - 1}{N_{238} e^{\lambda_{238} t_e} - 1}. \quad (33)$$

Once the lead abundance ratios have been measured in the two samples, and the present uranium isotope ratio

$$N_{235}/N_{238} = 0.00725 \quad (34)$$

is known, the age of the Earth t_e is the only unknown in Eq. (33). This method yields (Patterson, 1956; Wasserburg *et al.*, 1977)

$$t_e = 4.6 \pm 0.1 \text{ Gyr}. \quad (35)$$

2. The age of the Galaxy

A variant of this method can be used to estimate the age of the Galaxy, but this requires a model for how the radioactive elements were formed during the lifetime of the Galaxy until they were locked up in samples where we can measure their abundances today. Again, we can assume that the Galaxy formed quickly compared to its age t_g .

Suppose there was an instantaneous burst of star formation and subsequent supernova explosions a time t_g ago and no further production thereafter. Then, the radioactive elements found on Earth today decayed for the time $t_g - t_e$ until they were locked up when the Solar System formed. If we can infer from supernova theory the initially produced abundance ratio N_{235}/N_{238} , we can conclude from its present value [Eq. (34)] and the age of the Earth what the age of the Galaxy must be.

The situation is slightly more complicated because element production did not stop after the initial burst. Suppose that a fraction f of the total number N_p of the heavy nuclei locked up in the Solar System was produced in a burst at $t=0$ and the remaining fraction $1-f$ was added at a steady rate until $t=t_g - t_e$ when the Earth was formed. Given the constant production rate p , the abundance of a radioactive element with decay constant λ is

$$N = C e^{-\lambda t} + p/\lambda \quad (36)$$

before $t_g - t_e$, with a constant C to be suitably chosen, and

$$N = N_0 e^{-\lambda[t - (t_g - t_e)]} \quad (37)$$

thereafter, where N_0 is the abundance of the element locked up in the Solar System, as before. The initial conditions then require

$$N(0) = C + p/\lambda = f N_p \quad (38)$$

after the burst at $t=0$, thus

$$N(t_g - t_e) = e^{-\lambda(t_g - t_e)} \left[f N_p + \frac{p}{\lambda} (e^{\lambda(t_g - t_e)} - 1) \right] \quad (39)$$

when the Earth formed and

$$N(t_g) = e^{-\lambda t_g} \left[f N_p + \frac{p}{\lambda} (e^{\lambda(t_g - t_e)} - 1) \right] \quad (40)$$

today when the Galaxy reaches its age t_g . Since the production rate must be

$$p = (1-f) N_p / (t_g - t_e), \quad (41)$$

the present abundance is

$$N = N_p e^{-\lambda t_g} \left[f + \frac{(1-f)}{\lambda(t_g - t_e)} (e^{\lambda(t_g - t_e)} - 1) \right] \quad (42)$$

in terms of the produced abundance N_p . Supernova theory says that the *produced* abundance ratio of the isotopes ^{235}U and ^{238}U is (Cowan *et al.*, 1987, 1991)

$$N_{235,p}/N_{238,p} = 1.4 \pm 0.2. \quad (43)$$

Taking the ratio of Eq. (42) for the present abundances of ^{235}U and ^{238}U and inserting the decay constants from Eq. (30), the abundance ratios from Eqs. (34) and (43) and the age of the Earth t_e from Eq. (35) yield an equation which contains only the age of the Galaxy t_g in terms of the assumed fraction f . This gives

$$t_g = \begin{cases} 6.3 \pm 0.2 \text{ Gyr}, & f = 1 \\ 8.0 \pm 0.6 \text{ Gyr}, & f = 0.5 \\ 12 \pm 2 \text{ Gyr}, & f = 0. \end{cases} \quad (44)$$

More detailed models (Meyer and Schramm, 1986; Cowan *et al.*, 1987, 1991; Fowler, 1989) yield comparable results. Common assumptions and results from galaxy-formation theory assert that at least 1 Gyr is necessary before galactic disks could have been assembled. Therefore, nuclear cosmochronology constrains the age of the Galaxy to fall approximately within

$$7 \lesssim t_g \lesssim 13 \text{ Gyr}. \quad (45)$$

Interestingly, nuclear cosmochronology has also been applied to metal-poor and therefore presumably very old stars, in which heavy elements are nonetheless overabundant. For example, Cayrel *et al.* (2001) constrained the age of such a star to 12.5 ± 3 Gyr.

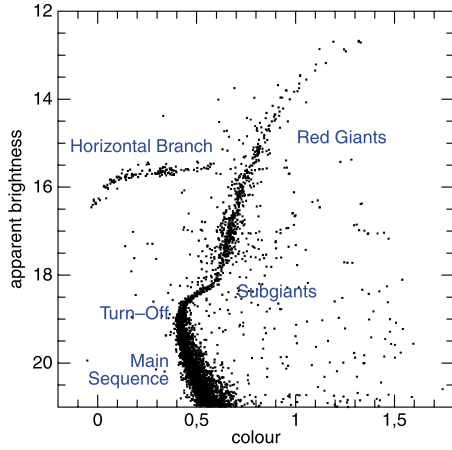


FIG. 5. (Color online) Hertzprung-Russell or color-magnitude diagram of the globular cluster M 68. The magnitude is a logarithmic measure of the luminosity; colors are defined as magnitude differences. Stars populate the main sequence while burning hydrogen, then turn away from it toward the giant branch. The main sequence turnoff is clearly visible. Courtesy of Achim Weiß.

B. Stellar ages

Another method for measuring the age of the Universe caused much trouble for cosmologists for a long time. It is based on stellar evolution and exploits the fact that the time spent by stars on the main sequence of the Hertzprung-Russell or color-magnitude diagram (see Fig. 5) depends sensitively on their mass and thus on their color.

Stars are described by the stellar-structure equations, which relate the mass M , the density ρ , and the pressure p to the radius r and specify the temperature T and the luminosity L . They are

$$\frac{dp}{dr} = -\frac{GM\rho}{r^2}, \quad \frac{dM}{dr} = 4\pi r^2 \rho, \quad (46)$$

which simply state hydrostatic equilibrium and mass conservation, and

$$\frac{dT}{dr} = \frac{3L\kappa\rho}{4\pi r^2 a_{\text{SB}} c T^3}, \quad \frac{dL}{dr} = 4\pi r^2 \rho \epsilon, \quad (47)$$

which describe radiative energy transport and energy production. κ is the opacity of the stellar material, ϵ is the energy production rate per unit mass, and a_{SB} is the Stefan-Boltzmann constant. Assuming κ is independent of temperature, the energy-transport equation, the mass conservation, the hydrostatic equilibrium, and the equation of state for an ideal gas yield the scaling relations

$$L \sim \frac{RT^4}{\rho}, \quad M \sim \rho R^3, \quad p \sim \frac{\rho M}{R}, \quad p \sim \rho T. \quad (48)$$

The second pair of equations gives $T \sim M/R$, which yields $L \sim M^3$ when inserted into the first pair.

The total lifetime τ of a star on the main sequence must scale as $L\tau \sim M$ because the total energy radiated $L\tau$ must be a fraction of the total rest-mass energy. Together with the earlier result, we find

$$\tau \sim M/L \sim M^{-2} \sim L^{-2/3}. \quad (49)$$

According to the Stefan-Boltzmann law, the star's luminosity must be

$$L \sim R^2 T^4 \Rightarrow R^2 \sim M^3/T^4, \quad (50)$$

but we also know from above that $T \sim M/R$. Thus

$$R^2 \sim \frac{M^3 R^4}{M^4} \sim \frac{R^4}{M} \Rightarrow R \sim M^{1/2}, \quad T \sim M^{1/2}, \quad (51)$$

and the lifetime τ on the main sequence turns out to scale as $\tau \sim T^{-1}$ by Eq. (49). Afterwards, stars move away from the main sequence toward the giant branch. Thus, as a coeval stellar population ages, the point in its Hertzprung-Russell diagram up to which the main sequence remains populated moves toward lower luminosities and temperatures along $(L, T) \sim (\tau^{-3/2}, \tau^{-1})$. Old coeval stellar populations exist: they are the globular clusters which surround the center of the Galaxy in an approximately spherical halo. Therefore, the main-sequence turn-off points can be used to derive lower limits to the age of the Galaxy and the Universe.

In practice, such age determinations proceed by adapting simulated stellar-evolution tracks to the Hertzprung-Russell diagrams of globular clusters and assigning the age of the best-fitting stellar-evolution model to the cluster (Renzini and Fusi Pecci, 1988; Straniero and Chieffi, 1991; Vandenberg, 2000). The simulated stellar-evolution tracks depend on the assumed metallicity of the stellar material, which changes the opacity and thus the energy transport through the stars.

Since observations cannot tell the luminosity of the turn-off point on the main sequence, but only its apparent brightness, age determinations from globular clusters require observations measuring both the apparent brightness of the main sequence turnoff and the distance to the globular cluster. There are several ways for estimating cluster distances. One uses the period-luminosity relation of a class of variable stars, the RR Lyrae stars, which are similar to the Cepheids that will play a central role in the next section. Another method exploits that stars on the horizontal branch have a typical luminosity and can thus be used to calibrate the cluster distance.

Therefore, uncertainties in the distance determinations directly translate to uncertainties in the age determinations. If the distance is overestimated, so is the luminosity, which implies that the age is underestimated and vice versa. Globular clusters typically appeared to have ages well above estimates based on the cosmological parameters assumed (Vandenberg, 1983; Sandage and Cacciari, 1990). In the past decade or so, this has changed because improvements in stellar-evolution theory and direct distance measurements with the Hipparcos satellite have lowered the globular-cluster ages,

while recently determined cosmological parameters yield a higher age for the Universe as assumed before (Salaris, degl'Innocenti, and Weiss, 1997; Chaboyer *et al.*, 1998). Now, globular-cluster ages imply

$$t_0 \gtrsim 12.5 \pm 1.3 \text{ Gyr} \quad (52)$$

for the age of the Universe, allowing for a Gyr between the Big Bang and the formation of the globular clusters (Chaboyer, 1998). The uncertainty in this result may still be considerable though [see, e.g., Grundahl *et al.* (2000)].

C. Cooling of white dwarfs

A third method for cosmic age determinations is based on the cooling of white dwarfs [see Hansen and Liebert (2003) for a review]. They are the end products in the evolution of low-mass stars and form when the nuclear fuel in the stellar cores is exhausted. This happens typically when a core of carbon and oxygen has formed and temperature necessary for further fusion cannot be reached. The C-O core then shrinks until it is stabilized by electron degeneracy pressure. At this point, the mean free path of the electrons becomes effectively infinite and the core turns isothermal.

The pressure of a degenerate electron gas is independent of temperature and depends only on the density. In the nonrelativistic limit, $p \propto \rho^{5/3}$ or

$$p \propto \frac{M^{5/3}}{R^5} \quad \text{and} \quad \frac{p}{R} \sim \frac{GM\rho}{R^2} \sim \frac{GM^2}{R^5}, \quad (53)$$

where the latter two equations express hydrostatic equilibrium. Together, these relations imply $R \propto M^{-1/3}$, showing that more massive white dwarfs have smaller radii. Their surface gravity

$$g \propto M/R^2 \propto M^{5/3}, \quad (54)$$

which can be determined from their spectra, is thus a direct measure for their mass. It turns out that the vast majority of white dwarfs are born with similar masses, $M_{\text{wd}} \approx (0.55 \pm 0.05)M_{\odot}$ (Cool *et al.*, 1996), which is a conspiracy of stellar evolution: more massive stars lose more mass through stellar winds before they turn into white dwarfs.

Except for the latent heat of crystallization, white dwarfs cool passively by radiating the thermal energy stored by their mass. Being born with essentially the same mass, they start with very similar amounts of thermal energy. Their temperatures and luminosities are determined by the radiation processes and the opacities of their atmospheres, which in turn depend on their metallicities. Age inferences from white dwarfs thus require that their metallicities be known and the energy transport through their atmospheres be modeled.

After an initial short phase of rapid neutrino cooling, the energy loss slows down. This change in cooling time causes the white dwarfs to pile up at the temperature and the luminosity where the energy loss due to neutrinos falls below that due to radiative cooling. Thus, as time proceeds, their luminosity distribution develops a

peak which is later slowly depopulated. Models for the white-dwarf cooling sequence allow the construction of time-dependent theoretical luminosity distributions from which, by comparison with the observed luminosity distribution, the age of a white-dwarf population can be determined. This method yields

$$t_{\text{wd}} \approx 9.5 \pm 1 \text{ Gyr} \quad (55)$$

for the age of white dwarfs in the galactic disk (Oswalt *et al.*, 1996; Salaris, Dominguez, *et al.*, 1997; Chaboyer, 1998). If we assume that massive spiral disks form at redshifts below $z \lesssim 3$, the implied age of the Universe is

$$t_0 \approx 11 \pm 1.4 \text{ Gyr}. \quad (56)$$

The age of the white-dwarf population in the globular cluster M 4 has been measured to be ~ 12.1 Gyr (Hansen *et al.*, 2004).

D. Summary

Combining results, we see that the age of the Universe, as measured by its supposedly oldest parts, is at least $\gtrsim 11$ Gyr, and this places serious cosmological constraints. In the framework of the Friedmann-Lemaître models, they can be interpreted as limits on the cosmological parameters. Suppose we lived in an Einstein-de Sitter universe with $\Omega_{m0}=1$ and $\Omega_{\Lambda 0}=0$. Then, we know from Eq. (16) that

$$t_0 = 2/3 H_0 \gtrsim 11 \text{ Gyr} \Rightarrow H_0 \lesssim 2 \times 10^{-18} \text{ s} \quad (57)$$

or $H_0 \lesssim 61 \text{ km s}^{-1} \text{ Mpc}^{-1}$ in conventional units. The Hubble constant is measured to be larger than this, which can immediately be interpreted as an indication that we are not living in an Einstein-de Sitter universe.

III. THE HUBBLE CONSTANT

A. Hubble constant from Hubble's law

1. Hubble's law

Slipher discovered preceding 1920 that distant galaxies typically move away from us (Slipher, 1927). Hubble found that their recession velocity grows with distance,

$$v = H_0 D, \quad (58)$$

and determined the constant of proportionality as $H_0 \approx 559 \text{ km s}^{-1} \text{ Mpc}^{-1}$ (Hubble and Humason, 1931). We had seen in Eq. (21) that all distance measures in a Friedmann-Lemaître universe follow the linear relation

$$D = cz/H_0 \quad (59)$$

to first order in $z \ll 1$. Since $cz = v$ is the velocity according to the linearized relation between redshift and velocity, Eq. (59) is exactly the relation Hubble found.

The problem with any measurement of the Hubble constant from Eq. (58) is that, while Eq. (59) holds for an idealized, homogeneous, and isotropic universe, real galaxies have peculiar motions on top of their Hubble velocity which are caused by the attraction from local den-

sity inhomogeneities. For instance, galaxies in our neighborhood feel the gravitational pull of a cosmologically nearby supercluster called the great attractor and accelerate toward it. The galaxy M31 in Andromeda is moving within the local group of galaxies and approaches the Milky Way.

Thus, the peculiar velocities of the galaxies either must be known well enough, for which a model for the velocity field is necessary, or they must be observed at such large distances that any peculiar motion is unimportant compared to their Hubble velocity. Requiring that the typical peculiar velocities, of order $300\text{--}600\text{ km s}^{-1}$, be less than 10% of the Hubble velocity, galaxies with redshifts

$$z \gtrsim 10 \times \frac{(300 - 600) \text{ km s}^{-1}}{c} \approx 0.01 - 0.02 \quad (60)$$

need to be observed. This is already so distant that it is hard or impossible to apply simple geometric distant estimators. This illustrates why accurate measurements of the Hubble constant are so difficult: nearby galaxies, whose distances are more accurately measurable, do not follow the Hubble expansion well, but the distances to galaxies far enough to follow the Hubble law are very hard to measure [see Sandage and Tammann (1974) for an account of the difficulties].

2. The distance ladder

Measurements of the Hubble constant from Hubble's law thus require accurate distance measurements out to cosmologically relevant distance scales. Since this is impossible in one step, the so-called distance ladder must be applied, in which each step calibrates the next.

The most fundamental distance measurement in the astrophysical toolbox is the trigonometric parallax caused by the annual motion of the Earth around the Sun. By definition, a star at a distance of a parsec perpendicular to the Earth's orbital plane has a parallax of 1 arc sec. Astrometric measurement accuracies of order $10^{-5}''$ are thus necessary to measure distances of order 10 kpc. Although the astrometric satellite Hipparcos could measure distances only to ≤ 1 kpc, its results were used to calibrate the distance ladder with nearby stars. In this way, it was possible to determine the distance to the Large Magellanic Cloud as $D_{\text{LMC}} = 54.0 \pm 2.5$ kpc (Feast and Catchpole, 1997). An independent distance estimate based on the elliptical ring that appeared around the supernova 1987A gave $D_{\text{LMC}} = 46.77 \pm 0.04$ kpc (Gould 1995; see also Panagia *et al.*, 1991).

The next important step in the distance ladder is formed by the Cepheids. These are stars in late evolutionary stages which undergo periodic variability. The underlying instability is driven by the temperature dependence of the atmospheric opacity in these stars, which is caused by the transition between singly and doubly ionized helium. The cosmologically important aspect of the Cepheids is that their variability period τ and their luminosity L are related,

$$L \propto \tau^{1.1} \quad (61)$$

in the V band (Feast and Walker, 1987; Madore and Freedman, 1991; Udalski *et al.*, 1999), hence their luminosity can be inferred from their variability period and their distance from the ratio of their luminosity to the flux S observed from them,

$$D = \sqrt{L/4\pi S}. \quad (62)$$

At the relevant distances, any distinction between differently defined distance measures is irrelevant.

It is important here that the calibration of the period-luminosity relation depends on the metallicity of the pulsating variables used and thus on the stellar population they belong to. Hubble's originally much too high result for H_0 was corrected when Baade realized that he had confused a metal-poor class of variable stars with the metal-rich Cepheids (Baade, 1956).

Measuring the periods of Cepheids and comparing their apparent brightnesses in different galaxies thus allow determination of the relative distances to the galaxies. For example, comparisons between Cepheids in the LMC and the Andromeda galaxy M31 show (Feast and Catchpole, 1997)

$$D_{\text{M31}}/D_{\text{LMC}} = 16.4 \pm 1.1, \quad (63)$$

while Cepheids in the member galaxies of the Virgo cluster yield (Freedman *et al.*, 2001)

$$D_{\text{Virgo}}/D_{\text{LMC}} = 305 \pm 16. \quad (64)$$

Of course, for the Cepheid method to be applicable, it must be possible to resolve at least the outer parts of distant galaxies into individual stars and to reliably identify Cepheids among them. This was one reason why the *Hubble Space Telescope* (HST) was proposed (Freedman *et al.*, 1994) to apply the superb resolution of an orbiting telescope to the measurement of H_0 . Cepheid distance measurements are possible to distances ≤ 30 Mpc.

Scaling relations within classes of galaxies provide additional distance indicators. In the three-dimensional parameter space spanned by the velocity dispersion σ_v of their stars, the radius R_e enclosing half the luminosity, and the surface brightness I_e within R_e , elliptical galaxies populate the tight *fundamental plane* (Djorgovski and Davis, 1987; Dressler *et al.*, 1987) defined by

$$R_e \propto \sigma_v^{1.4} I_e^{-0.85}. \quad (65)$$

Since the luminosity must be

$$L \propto I_e R_e^2, \quad (66)$$

the fundamental-plane relation implies

$$L \propto \sigma_v^{2.8} I_e^{-0.7}. \quad (67)$$

Such a relation follows directly from the virial theorem if the mass-to-light ratio in elliptical galaxies increases gently with mass,

$$M/L \propto M^{0.2}. \quad (68)$$

Thus, if it is possible to measure the surface brightness I_e and the velocity dispersion σ_v of an elliptical galaxy, the fundamental-plane relation gives the luminosity, which can be compared to the flux to find the distance.

An interesting way for determining distances to galaxies uses the fluctuations in their surface brightness (Tonry and Schneider, 1988; Tonry *et al.*, 1997, 2000). The idea behind this method is that the fluctuations in the surface brightness will be dominated by the rare brightest stars and that the optical luminosity of the entire galaxy will be proportional to the number N of such stars. Assuming Poisson statistics, the fluctuation level will be proportional to \sqrt{N} , from which N and $L \propto N$ can be determined once the method has been calibrated with galaxies whose distance is known otherwise. Again, the distance is then found by comparing the flux to the luminosity.

Planetary nebulae, which are late stages in the evolution of massive stars, have a luminosity function with a steep upper cutoff (Jacoby, 1980; Hui *et al.*, 1993). Moreover, their spectra are dominated by sharp nebular emission lines which facilitate their detection even at large distances because they appear as bright objects in narrow-band filters tuned to the emission lines. Since the cutoff luminosity is known, it can be converted to a distance.

An important class of distance indicators is supernovae of type Ia. As described in Sec. IX.B, their luminosities can be standardized, allowing their distances to be inferred from their fluxes.

Although they are not standard (or standardizable) candles, core-collapse supernovae of type II can also be used as distance indicators through the Baade-Wesselink method (Baade, 1926; Wesselink 1946). Suppose the spectrum of the supernova photosphere can be approximated by a Planck curve whose temperature can be determined from the spectral lines. Then, the Stefan-Boltzmann law fixes the total luminosity,

$$L = \sigma_{\text{SB}} R^2 T^4. \quad (69)$$

The photospheric radius, however, can be inferred from the expansion velocity of the photosphere, which is measurable by the Doppler shift in the emission lines, times the time after the explosion. When applied to the supernova SN 1987A in the Large Magellanic Cloud, the Baade-Wesselink method yields a distance of

$$D_{\text{LMC}} = 49 \pm 3 \text{ kpc} \quad (70)$$

based on infrared photometry (Schmidt *et al.*, 1992) which agrees with the direct distance measurements (Gould, 1995). Note that the Baade-Wesselink method gives a one-step geometrical distance indicator bypassing the distance ladder.

3. The HST key project

All these distance indicators were used in the *HST* key project (Freedman *et al.*, 2001) to determine accurate

distances to 26 galaxies between 3 and 25 Mpc and five very nearby galaxies for testing and calibration.

Double-blind photometry was applied to the identified distance indicators. Since Cepheids tend to lie in star-forming regions and are thus attenuated by dust and since their period-luminosity relation depends on metallicity, respective corrections had to be carefully applied. Then, the measured velocities had to be corrected by the peculiar velocities, which were estimated by a model for the flow field. The estimated luminosities of the distance indicators could then be compared with the extinction-corrected fluxes to determine distances, whose proportionality with the velocities corrected by the peculiar motions finally gave the Hubble constant. A weighed average over all distance indicators is (Freedman *et al.*, 2001)

$$H_0 = 72 \pm 8 \text{ km s}^{-1} \text{ Mpc}^{-1}, \quad (71)$$

where the error is the square root of the systematic and statistical errors summed in quadrature. An alternative interpretation of the data is summarized by Sandage *et al.* (2006), who found a 14% smaller value for H_0 because of a different calibration. Recently observations in the near infrared of 240 Cepheids were used to improve the value of the Hubble constant to

$$H_0 = 74.2 \pm 3.6 \text{ km s}^{-1} \text{ Mpc}^{-1} \quad (72)$$

(Riess *et al.*, 2009).

B. Gravitational lensing

A completely different method for determining the Hubble constant uses gravitational lensing. Masses bend passing light paths toward themselves and therefore act similarly to convex glass lenses. As in ordinary geometrical optics, this effect can be described applying Fermat's principle to a medium with an index of refraction (Schneider *et al.*, 1992)

$$n = 1 - 2\Phi/c^2, \quad (73)$$

where Φ is the Newtonian gravitational potential.

If it is strong enough, the bending of the light paths causes multiple images to appear from single sources. Compared to the straight light paths in absence of the deflecting mass distribution, the curved paths are geometrically longer, and they have to additionally propagate through a medium whose index of refraction is $n > 1$. This gives rise to a time delay (Blandford and Narayan, 1986) which has a geometrical and a gravitational component,

$$\tau = \frac{1 + z_d}{c} \frac{D_d D_{ds}}{D_s} \left[\frac{1}{2} (\vec{\theta} - \vec{\beta})^2 - \psi(\vec{\theta}) \right], \quad (74)$$

where $\vec{\theta}$ are angular coordinates on the sky and $\vec{\beta}$ is the angular position of the source. ψ is the appropriately scaled Newtonian gravitational potential of the deflector, projected along the line of sight. According to Fermat's principle, images occur where τ is extremal, i.e., $\vec{\nabla}_0 \tau = 0$. The prefactor contains the distances $D_{d,s,ds}$ from

the observer to the deflector, to the source, and from the deflector to the source, respectively, and the redshift z_d of the lens.

The projected lensing potential ψ is related to the surface-mass density Σ of the deflector by

$$\nabla^2 \psi = 2\Sigma/\Sigma_{\text{cr}} \equiv 2\kappa, \quad (75)$$

where the critical surface-mass density is

$$\Sigma_{\text{cr}} \equiv \frac{c^2}{4\pi G} \frac{D_s}{D_d D_{ds}}. \quad (76)$$

The dimensionless time delay τ from Eq. (74) is related to the true physical time delay t by

$$t \propto \tau/H_0, \quad (77)$$

where the proportionality constant is a dimensionless combination of the distances $D_{d,s,ds}$ with the Hubble radius cH_0^{-1} and the deflector redshift $1+z_d$. Equation (77) shows that the true time delay is proportional to the Hubble time, as it can intuitively be expected (Refsdal, 1964).

Time delays are measurable in multiple images of a variable source. The variable signal arrives after different times in the images seen by the observer. If the deflector is a galaxy, time delays are typically of the order of days to months and therefore observable with a reasonable monitoring effort.

Interestingly, it can be shown in a lengthy calculation (Kochanek, 2002) that measured time delays can be inverted to find the Hubble constant from

$$H_0 \approx A(1 - \langle \kappa \rangle) + B\langle \kappa \rangle(\eta - 1), \quad (78)$$

where A and B are constants depending on the measured image positions and time delays, $\langle \kappa \rangle$ is the mean scaled surface-mass density of the deflector averaged within an annulus bounded by the image positions, and $\eta \approx 2$ is the logarithmic slope of the deflector's density profile.

Therefore, if a model exists for the gravitationally lensing galaxy, the Hubble constant can be found from the positions and time delays of the images. Applying this technique to five different lens systems, Kochanek (2002) found

$$H_0 = 73 \pm 8 \text{ km s}^{-1} \quad (79)$$

assuming that the lensing galaxies have radially constant mass-to-light ratios.

This result is remarkable because it was obtained in one step without any reference to the extragalactic distance ladder. On the other hand, it is also problematic because it is obtained only if significantly more concentrated density profiles of the lensing galaxies are assumed than obtained, e.g., from the kinematics of the stars in galaxies. If less concentrated lenses are adopted which agree with the kinematic constraints, H_0 derived from gravitational time delays drops substantially to values near 50 km s^{-1} (Kochanek, 2003). This hints at an as

yet unexplained discrepancy between measurements of H_0 and the measured time delays within the CDM framework.

C. Summary

The results given so far are in excellent agreement with the value

$$H_0 = 70.1 \pm 1.3 \text{ km s}^{-1} \text{ Mpc}^{-1}, \quad (80)$$

derived from CMB measurements (see Sec. VI and Table I) assuming spatial flatness, $K=0$. Adopting it, we can calibrate several important numbers that scale with some power of the Hubble constant. First, in cgs units, the Hubble constant is

$$H_0 = (2.26 \pm 0.04) \times 10^{-18} \text{ s}, \quad (81)$$

which implies the Hubble time

$$H_0^{-1} = 14.01 \pm 0.26 \text{ Gyr} \quad (82)$$

and the Hubble radius

$$\frac{c}{H_0} = (1.327 \pm 0.025) \times 10^{28} \text{ cm} = 4.299 \pm 0.08 \text{ Gpc}. \quad (83)$$

The critical density of the Universe turns out to be

$$\rho_{\text{cr}0} = \frac{3H_0^2}{8\pi G} = (9.15 \pm 0.3) \times 10^{-30} \text{ g cm}^{-3}. \quad (84)$$

It corresponds to 5 protons/m³ or approximately 1 galaxy/Mpc³.

IV. BIG-BANG NUCLEOSYNTHESIS

A. The origin and abundance of ⁴He

1. Elementary considerations

Stellar spectra show that the abundance of ⁴He in stellar atmospheres is in the range $0.2 \lesssim Y \lesssim 0.3$ by mass (the Sun has $Y=0.263$), i.e., about a quarter of the baryonic mass in the Universe is composed of ⁴He. It is produced in stars in the course of hydrogen burning. Per ⁴He nucleus, the amount of energy released corresponds to 0.7% of the masses involved or

$$\begin{aligned} \Delta E &= \Delta mc^2 = 0.007(2m_p + 2m_n)c^2 \approx 0.028m_p c^2 \\ &\approx 26 \text{ MeV} \approx 4.2 \times 10^{-5} \text{ erg}. \end{aligned} \quad (85)$$

Suppose a galaxy such as ours, the Milky Way, shines with a luminosity of $L \approx 10^{10} L_\odot \approx 3.8 \times 10^{43} \text{ erg s}^{-1}$ for a good fraction of the age of the Universe, say for $\tau=5 \times 10^9 \text{ yr} \approx 1.5 \times 10^{17} \text{ s}$. Then, it releases a total energy of

$$E_{\text{tot}} \approx L\tau \approx 5.7 \times 10^{60} \text{ ergs}. \quad (86)$$

The number of ⁴He nuclei required to produce this energy is

$$\Delta N = \frac{E}{\Delta E} \approx \frac{5.7 \times 10^{60}}{4.2 \times 10^{-5}} \approx 1.4 \times 10^{65}, \quad (87)$$

which amounts to a ${}^4\text{He}$ mass of

$$M_{\text{He}} \approx 4m_p \Delta N \approx 9.3 \times 10^{41} \text{ g}. \quad (88)$$

Assume further that the galaxy's stars were all composed of pure hydrogen initially and that they are all more or less similar to the Sun. Then, the mass in hydrogen was $M_{\text{H}} \approx 10^{10} M_{\odot} \approx 2 \times 10^{43} \text{ g}$ initially and the final ${}^4\text{He}$ abundance by mass expected from the energy production is

$$Y_* \approx \frac{9.3 \times 10^{41}}{2 \times 10^{43}} \approx 5\%, \quad (89)$$

much less than the ${}^4\text{He}$ abundance actually observed. This discrepancy is exacerbated by the fact that ${}^4\text{He}$ is destroyed in later stages of the evolution of massive stars, a process affected also by mixing in stellar interiors.

We thus see that the amount of ${}^4\text{He}$ observed in stars was highly unlikely produced by these stars themselves under reasonable assumptions during the lifetime of the galaxies. We must therefore consider that most of the ${}^4\text{He}$ which is now observed may have existed already well before the galaxies formed.

Nuclear fusion of ${}^4\text{He}$ and similar light nuclei in the early Universe is possible only if the Universe was hot enough for a sufficiently long period during its early evolution. The nuclear binding energies of order $\sim \text{MeV}$ imply that temperatures had to have fallen below $T \sim 10^6 \text{ MeV} \times 1.16 \times 10^4 \text{ K/MeV} = 1.16 \times 10^{10} \text{ K}$ before nucleosynthesis could begin. On the other hand, temperatures needed to be still high enough for charged nuclei to surmount the Coulomb barrier. Typical temperatures during primordial nucleosynthesis were of order $kT \lesssim 100 \text{ keV}$. Since the temperature of the (photon background in the) Universe is now $T_0 \sim 3 \text{ K}$ as we see later, this corresponds to times when the scale factor of the Universe was

$$a_{\text{nuc}} \gtrsim 3/1.16 \times 10^9 \approx 2.59 \times 10^{-9}. \quad (90)$$

At times so early, the actual mass density and a possible cosmological constant are entirely irrelevant for the expansion of the Universe, which is only driven by the radiation density. Thus, the expansion function can be simplified to $E(a) = \Omega_{r0}^{1/2} a^{-2}$, and we find for the cosmic time according to Eq. (15),

$$t(a) = \frac{1}{\Omega_{r0}^{1/2} H_0} \int_0^a a' da' = \frac{a^2}{2\Omega_{r0}^{1/2} H_0} \approx 2.40 \times 10^{19} a^2 \text{ s}, \quad (91)$$

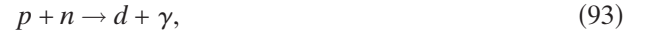
where we have inserted the Hubble constant from Eq. (80) and the radiation-density parameter today, $\Omega_{r0} \approx 8.51 \times 10^{-5}$, which will be justified later [see Eq. (158)]. The function contains contributions from photons and three neutrino species, which are the particles relativistic at the relevant time.

Inserting a_{nuc} from Eq. (90) into Eq. (91) yields a time scale for nucleosynthesis of order a few minutes. It is instructive for later purposes to establish a relation between time and temperature based on Eq. (91). Since $T = T_0/a$,

$$t = 2.40 \times 10^{19} \left(\frac{T_0}{T} \right)^2 \text{ s} \approx 0.89 \left(\frac{T}{\text{MeV}} \right)^{-2} \text{ s}. \quad (92)$$

2. The Gamow criterion

A crucially important step in the fusion of ${}^4\text{He}$ is the fusion of deuterium d ,



because the direct fusion of ${}^4\text{He}$ from two neutrons and two protons is extremely unlikely. The conditions in the early Universe must have been such that deuterium could be formed efficiently enough for the subsequent fusion of ${}^4\text{He}$ but not too efficiently because otherwise too much deuterium would be left over after the end of nucleosynthesis. Realizing this Gamow (1948) suggested that the amount of deuterium produced had to be “just right,” which he translated into the intuitive criterion

$$n_B \langle \sigma v \rangle t \approx 1, \quad (94)$$

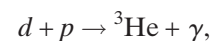
where n_B is the baryon number density, $\langle \sigma v \rangle$ is the velocity-averaged cross section for reaction (93), and t is the time available for the fusion, which we have seen in Eq. (92) to be set by the present temperature of the cosmic radiation background T_0 and the temperature T required for deuterium fusion.

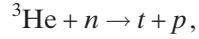
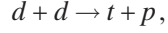
Thus, from an estimate of the baryon density n_B in the Universe, from the known velocity-averaged cross section $\langle \sigma v \rangle$, and from the known temperature required for deuterium fusion, Gamow's criterion enables an estimate of the present temperature T_0 of the cosmic radiation background. Based on this, Alpher and Herman (1949) were able to predict $T_0 \approx 1\text{--}5 \text{ K}$. After these remarkably simple and far-reaching conclusions, we now study primordial nucleosynthesis and consequences thereof in more detail.

3. Elements produced

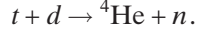
The fusion of deuterium [Eq. (93)] is the crucial first step. Since the photodissociation cross section of d is large, destruction of d is very likely because of the intense photon background until the temperature has dropped way below the binding energy of d , which is only 2.2 MeV , corresponding to $2.6 \times 10^{10} \text{ K}$. In fact, substantial d fusion is delayed until the temperature falls to $T = 9 \times 10^8 \text{ K}$ or $kT \approx 78 \text{ keV}$. As Eq. (92) shows, this happens, $t \approx 150 \text{ s}$, after the Big Bang.

From deuterium, ${}^3\text{He}$ and tritium t can be built, which can both be processed to ${}^4\text{He}$. These reactions are now fast, immediately converting the newly formed d . In detail, these reactions are



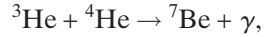


followed by

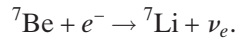


Fusion reactions with neutrons are irrelevant because free neutrons are immediately locked up in deuterons once deuterium fusion begins, and passed on to t , ${}^3\text{He}$, and ${}^4\text{He}$ in the further fusion steps.

Since there are no stable elements with atomic weight $A=5$, addition of protons to ${}^4\text{He}$ is unimportant. Fusion with d is unimportant because its abundance is very low due to the efficient follow-up reactions. We can therefore proceed only by fusing ${}^4\text{He}$ with t and ${}^3\text{He}$ to build up elements with $A=7$,



followed by



Some ${}^7\text{Li}$ is destroyed by



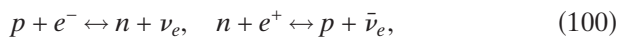
The fusion of two ${}^4\text{He}$ nuclei leads to ${}^8\text{Be}$, which is unstable. Further fusion of ${}^8\text{Be}$ in the reaction



is virtually impossible because the low density of the reaction partners essentially excludes that a ${}^8\text{Be}$ nucleus meets a ${}^4\text{He}$ nucleus during its lifetime. While reaction (99) is possible and extremely important in stars, it is suppressed below any importance in the early Universe. The absence of stable elements with $A=8$ thus prohibits any primordial element fusion beyond ${}^7\text{Li}$.

4. Helium abundance

Once stable hadrons can form from the quark-gluon plasma in the very early Universe, neutrons and protons are kept in thermal equilibrium by the weak interactions,



until the interaction rate falls below the expansion rate of the Universe. While equilibrium is maintained, the abundances n_n and n_p are controlled by the Boltzmann factor

$$\frac{n_n}{n_p} = \left(\frac{m_n}{m_p}\right)^{3/2} \exp\left(-\frac{Q}{kT}\right) \approx \exp\left(-\frac{Q}{kT}\right), \quad (101)$$

where $Q=1.3$ MeV is the energy equivalent of the mass difference between the neutron and the proton.

The weak interaction freezes out when $T \approx 10^{10}$ K or $kT \approx 0.87$ MeV, which is reached $t \approx 2$ s after the Big Bang. At this time, the n abundance by mass is

$$\begin{aligned} X_n(0) &\equiv \frac{n_n m_n}{n_n m_n + n_p m_p} \\ &\approx \frac{n_n}{n_n + n_p} \\ &= \left[1 + \exp\left(\frac{Q}{kT_n}\right)\right]^{-1} \approx 0.17. \end{aligned} \quad (102)$$

Afterwards, the free neutrons undergo β decay with a half-life¹ of $\tau_n = 885.7 \pm 0.8$ s, thus

$$X_n = X_n(0) e^{-t/\tau_n}. \quad (103)$$

When d fusion finally sets in at $t_d \approx 150$ s after the Big Bang, the neutron abundance has dropped to

$$X_n(t_d) \approx X_n(0) e^{-t_d/\tau_n} \approx 0.14. \quad (104)$$

Now, essentially all these neutrons are collected into ${}^4\text{He}$ because the abundances of the other elements can be neglected to first order. This simple estimate yields a ${}^4\text{He}$ abundance by mass of

$$Y \approx 2X_n(t_d) \approx 0.28 \quad (105)$$

because the neutrons are locked up in pairs to form ${}^4\text{He}$ nuclei. The Big-Bang model thus allows the prediction that ${}^4\text{He}$ must have been produced such that its abundance is approximately 28% by mass, which is in remarkable agreement with the observed abundance and thus a strong confirmation of the Big-Bang model.

5. Expected abundances and abundance trends

Precise abundances of the light elements as produced by the primordial fusion must be calculated solving rate equations based on the respective fusion cross sections. Uncertainties involved concern the exact values of the cross sections and their energy dependence and the precise lifetime of the free neutrons. Since primordial nucleosynthesis happens during the radiation-dominated era, the expansion rate is exclusively set by the radiation density. Then, the only other parameter controlling the primordial fusion processes is the baryon density if the neutron lifetime is taken for granted.

A recent review of these matters is [Steigman \(2007\)](#), to which we refer for further detail.

Ignoring possible modifications by nonstandard temperature evolution, the only relevant parameter defining the primordial abundances is the ratio between the number densities of baryons and photons. Since both densi-

¹Particle Data Group, <http://pdg.lbl.gov/>

ties scale like a^{-3} or, equivalently, like T^3 , their ratio η is constant. Anticipating the photon number density to be determined from the temperature of the CMB,

$$\eta = n_B/n_\gamma = 10^{-10} \eta_{10}, \quad \eta_{10} \equiv 273 \Omega_B h^2. \quad (106)$$

Thus, once we know the photon number density and once we can determine the parameter η from the primordial element abundances, we can infer the baryon number density. Typical 2σ uncertainties at a fiducial η parameter of $\eta_{10}=5$ are 0.4% for ${}^4\text{He}$, 15% for d and ${}^3\text{He}$, and 42% for ${}^7\text{Li}$. The ${}^4\text{He}$ abundance depends only very weakly on η because the largest fraction of free neutrons is swept up into ${}^4\text{He}$ without strong sensitivity to the detailed conditions.

The principal effects determining the abundances of d , ${}^3\text{He}$, and ${}^7\text{Li}$ are the following: with increasing η , they can more easily be burned to ${}^4\text{He}$ and so their abundances drop as η increases. At low η , an increase in the proton density causes ${}^7\text{Li}$ destruction in reaction (98), while the precursor nucleus ${}^7\text{Be}$ is more easily produced if the baryon density increases further. This creates a characteristic “valley” of the predicted ${}^7\text{Li}$ abundance near $\eta \approx (2-3) \times 10^{-10}$.

B. Observed element abundances

1. Principles

Of course, the main problem with any comparison between light-element abundances predicted by primordial nucleosynthesis and their observed values is that much time has passed since the primordial fusion ceased and further fusion processes have happened since. Seeking to determine the primordial abundances, observers must therefore select objects in which little or no contamination by later nucleosynthesis can reasonably be expected, in which the primordial element abundance may have been locked up and separated from the surroundings, or whose observed element abundances can be corrected for their enrichment during cosmic history in some way.

Deuterium can be observed in cool neutral-hydrogen gas (HI regions) via resonant UV absorption from the ground state, in radio wavebands via the hyperfine spin-flip transition, or in the submillimeter regime via $d\text{H}$ molecule lines. These methods all employ the fact that the heavier d nucleus causes small changes in the energy levels of electrons bound to it. ${}^3\text{He}$ is observed through the hyperfine transition in its ion ${}^3\text{He}^+$ in radio wavebands or through its emission and absorption lines in HII regions. ${}^4\text{He}$ is of course most abundant in stars, but the fusion of ${}^4\text{He}$ in stars is virtually impossible to be corrected precisely. Rather, ${}^4\text{He}$ is probed via the emission from optical recombination lines in HII regions (Izotov and Thuan, 2004). Measurements of ${}^7\text{Li}$ must be performed in old local stellar populations. This restricts observations to cool low-mass stars because of their long lifetime and to stars in the galactic halo to allow precise spectra to be taken despite the low ${}^7\text{Li}$ abundance.

2. Evolutionary corrections

Stars brooded heavy elements as early as $z \sim 6$ or even higher (Ciardi and Ferrara, 2005). Any attempts at measuring primordial element abundances must therefore concentrate on gas with a metal abundance as low as possible. The dependence of the element abundances on metallicity allows extrapolations to zero enrichment.

Such evolutionary corrections are low for d because it is observed in the Lyman- α forest lines, which arise from absorption in low-density cool gas clouds at high redshift. Likewise, they are low for the measurements of ${}^4\text{He}$ because it is observed in low-metallicity extragalactic HII regions. Probably, little or no correction is required for the ${}^7\text{Li}$ abundances determined from the spectra of very metal-poor halo stars (Charbonnel and Primas, 2005), but a lively discussion is on going (Asplund *et al.*, 2006; Korn *et al.*, 2006).

Inferences from ${}^3\text{He}$ are different because ${}^3\text{He}$ is produced from d in stars during the pre-main-sequence evolution. It is burnt to ${}^4\text{He}$ during the later phases of stellar evolution in stellar cores but conserved in stellar exteriors. Observations indicate that a net destruction of ${}^3\text{He}$ must happen, possibly due to extra mixing in stellar interiors. For these uncertainties, ${}^3\text{He}$ is commonly excluded from primordial abundance measurements.

3. Specific results

Due to the absence of strong evolutionary effects and its steep monotonic abundance decrease with increasing η , d is perhaps the most trustworthy baryometer. Since it is produced in the early Universe and destroyed by later fusion in stars, all d abundance determinations are lower bounds to its primordial abundance. Measurements of the d abundance at high redshift are possible through absorption lines in quasistellar object (QSO) spectra, which are likely to probe gas with primordial element composition or close to it. Such measurements are challenging in detail because the tiny isotope shift in the d lines needs to be distinguished from velocity-shifted hydrogen lines, H abundances from saturated H lines need to be corrected by comparison with higher-order lines, and high-resolution spectroscopy is required for accurate continuum subtraction.

A deuterium abundance of

$$n_d/n_{\text{H}} = (2.68_{-0.25}^{+0.27}) \times 10^{-5} \quad (107)$$

in high-redshift QSOs relative to hydrogen appears consistent with most relevant QSO spectra, although substantially lower values have been derived (Pettini and Bowen, 2001). A substantial depletion from the primordial value is unlikely because any depletion should be caused by d fusion and thus be accompanied by an increase in metal abundances, which should be measurable.

Some spectra which were interpreted as having less than or approximately equal to ten times the d abun-

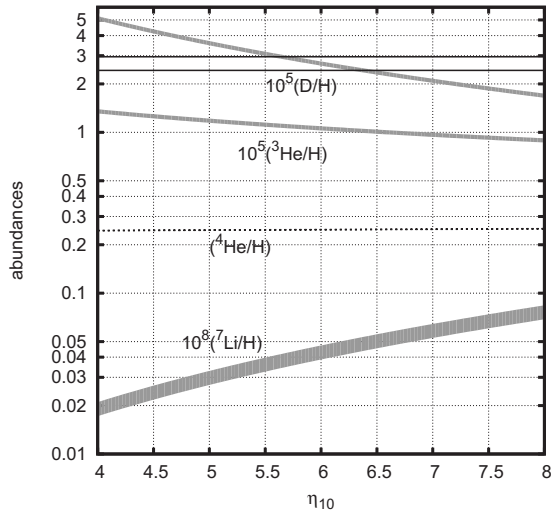


FIG. 6. Theoretically expected abundances of the light elements deuterium, ^3He , ^4He , and ^7Li as functions of η_{10} (following Steigman, 2007). The observed deuterium abundance is marked by the two horizontal solid lines.

dance from Eq. (108) may be due to lack of spectral resolution. The d abundance in the local interstellar medium is typically lower,

$$n_d/n_H \sim 1.5 \times 10^{-5}, \quad (108)$$

which is consistent with d consumption due to fusion processes. Conversely, the d abundance in the Solar System is higher because d is locked up in the ice on the giant planets.

In low-metallicity systems, ^4He should be near its primordial abundance and a metallicity correction can be applied. Possible systematic uncertainties are due to modifications by underlying stellar absorption, collisional excitation of observed recombination lines, and the exact regression toward zero metallicity. Values between $Y_p = 0.240 \pm 0.006$ and 0.2477 ± 0.0029 are considered realistic and likely (Peimbert *et al.*, 2007) (see Fig. 6).

Observations of the ^7Li abundance aim at the oldest stars in the Galaxy, which are halo (Pop-II) stars with very low metallicity. They should have locked up very nearly primordial gas but may have processed it (Salaris and Weiss, 2001; Pinsonneault *et al.*, 2002). Cool stellar atmospheres are difficult to model, and ^7Li may have been produced by cosmic-ray spallation on the interstellar medium (Steigman and Walker, 1992).

In the limit of low stellar metallicity, the observed ^7Li abundances group around an approximately flat line [the so-called Spite plateau (Spite and Spite, 1982)], which is asymptotically independent of metallicity,

$$A(^7\text{Li}) = 12 + \log_{10}(n_{\text{Li}}/n_{\text{H}}) = 2.2 \pm 0.1, \quad (109)$$

and show very little dispersion. Stellar rotation is important here because it enhances mixing in stellar interiors (Pinsonneault *et al.*, 2002).

The Spite plateau is unlikely to reflect the primordial ^7Li abundance, but corrections are probably moderate.

A possible increase of ^7Li with the iron abundance indicates low production of ^7Li , but the probable net effect is a depletion with respect to the primordial abundance by no more than ~ 0.2 dex. A conservative estimate yields

$$2.1 \leq A(^7\text{Li}) \leq 2.5. \quad (110)$$

In absence of depletion, this value falls into the valley expected in the primordial ^7Li at the boundary between destruction by protons and production from ^8Be . However, if ^7Li was in fact depleted, its primordial abundance was higher than value (110), and then two values for η_{10} are possible.

4. Summary of results

Through relation (106), the density of *visible* baryons alone implies $\eta_{10} \geq 1.5$. The deuterium abundance derived from absorption systems in the spectra of high-redshift QSOs indicates $\eta_{10} = 5.65\text{--}6.38$. The ^7Li abundance predicted from this value of η is then $A(^7\text{Li})_p = 3.81\text{--}4.86$, which is at least in mild conflict with the observed value $A(^7\text{Li}) = 2.1\text{--}2.3$, even if a depletion by 0.2 dex due to stellar destruction is allowed.

The predicted primordial abundance of ^4He is then $Y_p = 0.2477\text{--}0.2489$, which overlaps with the measured value $Y_p = 0.228\text{--}0.248$. Thus, the light-element abundances draw a consistent picture starting from the observed deuterium abundance.

We thus find that big-bang nucleosynthesis *alone* implies

$$0.0207 \leq \Omega_B h^2 \leq 0.0234 \quad \text{or} \quad 0.0399 \leq \Omega_B \leq 0.045 \quad (111)$$

if conclusions are predominantly based on the deuterium abundance in high-redshift absorption systems. We later see that this result is in agreement with independent estimates of the baryon density obtained from the analysis of structures in the CMB.

At this point it is important to note that primordial nucleosynthesis depends on the number of relativistic particle species and thus on the number of light neutrino families. The theoretical abundances given here assume three lepton families in the standard model of the electroweak interaction. In fact, light-element abundances had been used to constrain the number of lepton families before it was measured in particle detectors (Steigman *et al.*, 1977; Yang *et al.*, 1984).

V. THE MATTER DENSITY IN THE UNIVERSE

A. Mass in galaxies

1. Stars

Given the luminosity of a stellar population, what is its mass? If all stars were like the Sun, the answer was trivial, but this is not the case. We focus the discussion here on stars which fall on the main sequence of the color-magnitude diagram. Stars are formed with an ini-

tial mass distribution, the “initial mass function,” which is for our purposes reasonably approximated by the Salpeter form (Salpeter, 1955),

$$dN/d \ln M \propto M^{-1.35}. \quad (112)$$

Expressing the mass M in solar units, $m \equiv M/M_\odot$, and normalizing the mass distribution to unity in the mass range $m_0 \leq m < \infty$ yield

$$dN/dm = 1.35 \left(\frac{m_0}{m} \right)^{2.35} \frac{dm}{m_0}. \quad (113)$$

The accepted lower-mass limit for a star is $m_0 = 0.08$ because nuclear fusion cannot set in in objects of lower mass. However, we are interested in stars that are able to produce visible or near-infrared light so that we can translate the respective measured luminosities into mass. For a simple estimate, assume that stars have approximate Planck spectra, for which Wien’s law holds, relating the wavelength λ_{\max} of the peak in the Planck curve to the temperature T ,

$$\lambda_{\max} = 0.29 \left(\frac{\text{K}}{T} \right) \text{ cm}. \quad (114)$$

The effective solar temperature $T_\odot = 5780$ K implies $\lambda_{\max} = 5.0 \times 10^{-5}$ cm. Stars releasing the majority of their energy in the optical and near-infrared regime should have $\lambda_{\max} \leq 1 \mu\text{m} = 10^{-4}$ cm and thus $T \geq 2900$ K $\approx 0.5T_\odot$. We saw in Eq. (51) that the temperature scales as $T \sim M^{1/2}$; thus, $T \geq 0.5T_\odot$ implies $m_0 \approx 0.25$.

We also saw following Eq. (48) that the luminosity scales as $L \sim M^3$. With $l \equiv L/L_\odot$, the mean mass-to-light ratio of the visible stellar population is thus expected to be

$$\left\langle \frac{m}{l} \right\rangle = \int_{m_0}^{\infty} \frac{dN}{dm} \left(\frac{m}{l} \right) dm = \int_{m_0}^{\infty} \frac{dN}{dm} \frac{dm}{m^2} = \frac{1.35}{3.35m_0^2} \approx 6.4. \quad (115)$$

This shows that an average stellar population visible in the optical and near-infrared spectral ranges is expected to require ≈ 6.4 solar masses for one solar luminosity. In order to produce, say, $10^{10}L_\odot$, a galaxy thus needs to have a mass of at least $\approx 6.4 \times 10^{10}M_\odot$. This estimate assumes a homogeneous stellar population at the beginning of its evolution and neglects corrections from the exact spectral-energy distribution of the stars and the emission of giant stars, but $\langle m/l \rangle \geq 6.4$ still seems appropriate for evolved populations.

2. Galaxies

The rotation velocities of stars orbiting in spiral galaxies are observed to rise quickly with radius and then to remain roughly constant (Sofue and Rubin, 2001). If measurements are continued with neutral hydrogen beyond the radii out to which stars can be seen, these *rotation curves* are observed to continue at an approximately constant level (Kregel and van der Kruit, 2004).

In a spherically symmetric mass distribution, test particles on circular orbits have orbital velocities of

$$v_{\text{rot}}^2(r) = GM(r)/r. \quad (116)$$

Flat rotation curves thus imply that $M(r) \propto r$, requiring the density to drop like $\rho(r) \propto r^{-2}$. This is much flatter than the light distribution, which shows that spiral galaxies are characterized by an increasing amount of dark matter as the radius increases.

A mass distribution with $\rho \propto r^{-2}$ has formally infinite mass, which is physically implausible. However, at finite radius, the density of the Galaxy falls below the mean density of the surrounding Universe. The spherical-collapse model (Gunn and Gott, 1972) often invoked in cosmology shows that a spherical mass distribution can be considered in dynamical equilibrium if its mean overdensity is approximately 200 times higher than the mean density $\bar{\rho}$. Let R be the radius enclosing this overdensity and M be the mass enclosed, then

$$\frac{M}{V} = \frac{3M}{4\pi R^3} = 200\bar{\rho} \Rightarrow \frac{M}{R} = \frac{800\pi\bar{\rho}R^2}{3}. \quad (117)$$

At the same time, Eq. (116) needs to be satisfied, hence

$$\frac{800\pi\bar{\rho}R^2}{3} = \frac{v_{\text{rot}}^2}{G} \Rightarrow R = \left(\frac{3v_{\text{rot}}^2}{800\pi G\bar{\rho}} \right)^{1/2}. \quad (118)$$

Inserting typical numbers yields

$$R = 290 \text{ kpc} \left(\frac{v_{\text{rot}}}{200 \text{ km s}^{-1}} \right). \quad (119)$$

With Eq. (116), this implies

$$M = \frac{Rv_{\text{rot}}^2}{G} = 2.7 \times 10^{12} M_\odot \left(\frac{v_{\text{rot}}}{200 \text{ km s}^{-1}} \right)^3. \quad (120)$$

Typical luminosities of spiral galaxies are given by the Tully-Fisher relation (Tully and Fisher, 1977),

$$L = L_* \left(\frac{v_{\text{rot}}}{220 \text{ km s}^{-1}} \right)^{3-4}, \quad (121)$$

with $L_* \approx 2.4 \times 10^{10}L_\odot$. Thus, the mass-to-light ratio of a massive spiral galaxy is found to be

$$m/l \approx 150 \quad (122)$$

in solar units, where it is assumed that the Galaxy extends out to the virial radius of ≈ 290 kpc with the same density profile r^{-2} . Evidently, this exceeds the *stellar* mass-to-light ratio by far. Of course, the mass-to-light ratio of galaxies depends on the limiting radius assumed. Values of $m/l \approx 30$ are often quoted, which are typically based on the largest radii out to which rotation curves can be measured.

3. The galaxy population

Galaxy luminosities are observed to be distributed according to the Schechter function (Schechter, 1976),

$$\frac{dN}{dL} = \frac{\Phi_*}{L_*} \left(\frac{L}{L_*} \right)^{-\alpha} \exp\left(-\frac{L}{L_*}\right), \quad (123)$$

where the normalizing factor is $\Phi_* \approx 3.7 \times 10^{-3} \text{ Mpc}^{-3}$, the scale luminosity is L_* given by Eq. (121), and the power-law exponent is $\alpha \approx 1$ (Madgwick *et al.*, 2002). Irrespective of which physical processes this distribution originates from, its functional form turns out to characterize mixed galaxy populations very well, even in galaxy clusters.

The luminosity density in galaxies is found to be

$$\begin{aligned} \mathcal{L}_g &= \int_0^\infty L \frac{dN}{dL} dL = \Phi_* L_* \int_0^\infty l^{1-\alpha} e^{-l} dl = \Gamma(2-\alpha) \Phi_* L_* \\ &\approx \Phi_* L_* \approx 7.4 \times 10^7 \frac{L_\odot}{\text{Mpc}^3}, \end{aligned} \quad (124)$$

The average mass-to-light ratio [Eq. (122)] then allows converting this number into a mass density,

$$\begin{aligned} \langle \rho_g \rangle &= \left\langle \frac{m}{l} \right\rangle \mathcal{L}_g \approx 1.1 \times 10^{-4} \frac{M_\odot}{\text{Mpc}^3} \\ &\approx 7.5 \times 10^{-31} \text{ g cm}^{-3} \end{aligned} \quad (125)$$

and thus, with $\rho_{\text{cr0}} = 9.15 \times 10^{-30} \text{ g cm}^{-3}$ from Eq. (84),

$$\Omega_{g0} \approx 0.08. \quad (126)$$

Of course, estimates based on the more conservative mass-to-light ratio $m/l \approx 30$ find values which are lower by a factor of ~ 5 . In summary, this shows that the total mass expected to be contained in the dark-matter halos hosting galaxies contributes of order 8% to the critical density in the Universe.

B. Mass in galaxy clusters

1. Kinematic masses

The next step upward in the cosmic hierarchy are galaxy clusters, which were first identified as significant galaxy overdensities in relatively small areas of the sky (Herschel, 1786, 1789). Although the majority of galaxies is not in galaxy clusters, rich galaxy clusters contain several hundred galaxies, which by themselves contain a total amount of mass

$$M_g \lesssim 10^2 L_* \langle m/l \rangle \approx 3 \times 10^{14} M_\odot. \quad (127)$$

The mass in stars is of course considerably lower. With the mean stellar mass-to-light ratio of $m/l \approx 6.4$ from Eq. (115), the same luminosity implies

$$M_* \lesssim 1.3 \times 10^{13} M_\odot. \quad (128)$$

The stellar mass of the Coma cluster, for instance, is inferred to be $M_{*,\text{Coma}} \approx (1.4 \pm 0.3) \times 10^{13} M_\odot$ (White *et al.*, 1993).

The galaxies in rich galaxy clusters move with typical velocities of order $\lesssim 10^3 \text{ km s}^{-1}$, measured from the red-

shifts in their spectra. Therefore, only one component of the galaxy velocity is observed. Its distribution is characterized by the velocity dispersion σ_v .

If these galaxies were not gravitationally bound to the clusters, the clusters would disperse within $\lesssim 1 \text{ Gyr}$. Since they exist over cosmological time scales, clusters need to be (at least in some sense) gravitationally stable. Assuming virial equilibrium, the potential energy of the cluster galaxies should be minus two times the kinetic energy or

$$GM/R \approx 3\sigma_v^2, \quad (129)$$

where M and R are the total mass and the virial radius of the cluster, and the factor 3 arises because the velocity dispersion represents only one of the three velocity components. We combine Eq. (129) with Eq. (117) to find

$$R = \left(\frac{9\sigma_v^2}{800\pi G\bar{\rho}} \right)^{1/2} \approx 2.5 \text{ Mpc} \left(\frac{\sigma_v}{1000 \text{ km s}^{-1}} \right), \quad (130)$$

and, with Eq. (129),

$$M \approx 1.7 \times 10^{15} M_\odot \left(\frac{\sigma_v}{1000 \text{ km s}^{-1}} \right)^3. \quad (131)$$

Hence, the mass required to keep cluster galaxies bound despite their high velocities exceeds the mass in galaxies by about one order of magnitude, even if the entire virial mass of the Galactic halos is accounted for (Zwicky, 1933, 1937). The stellar mass apparently contributes just about 1% to the total cluster mass.

2. Mass in the hot intracluster gas

Galaxy clusters are diffuse sources of thermal x-ray emission. Their x-ray continuum is caused by thermal bremsstrahlung, whose bolometric volume emissivity is

$$j_X = Z^2 g_{\text{ff}} C_X n^2 \sqrt{T} \quad (132)$$

in cgs units, where Z is the ion charge, g_{ff} is the Gaunt factor, n is the ion number density, T is the gas temperature, and

$$C_X = 2.68 \times 10^{-24} \quad (133)$$

in cgs units if T is measured in keV.

A common simple axisymmetric model for the gas-density distribution in clusters, adapted to x-ray observations, is

$$n(x) = \frac{n_0}{(1+x^2)^{3\beta/2}}, \quad x \equiv \frac{r}{r_c} = \frac{\theta}{\theta_c}, \quad (134)$$

where r_c and θ_c are the physical and angular core radii. The line-of-sight projection of the x-ray emissivity yields the x-ray surface brightness as a function of the angular radius θ ,

$$S_X(\theta) = \int_{-\infty}^{\infty} j_X dz = \frac{\sqrt{\pi}\Gamma(3\beta-1/2)}{\Gamma(3\beta)} \frac{Z^2 g_{\text{ff}} C_X r_c n_0^2 \sqrt{T}}{[1+x^2]^{3\beta-1/2}}, \quad (135)$$

where we have combined Eqs. (132) and (134) and assumed for simplicity that the cluster is isothermal, so T does not change with radius. The latter equation shows that two parameters of the density profile (134), namely, the slope β and the (angular) core radius θ_c , can be read off the observable surface-brightness profile.

The missing normalization constant can be obtained from the x-ray luminosity,

$$L_X = 4\pi \int_0^R j_X r^2 dr = 4\pi r_c^3 Z^2 g_{\text{ff}} C_X \sqrt{T} n_0^2 \frac{\sqrt{\pi}\Gamma(3\beta-3/2)}{4\Gamma(3\beta)}, \quad (136)$$

and a spectral determination of the temperature T . Finally, the total mass of the x-ray gas enclosed in spheres of radius R is

$$M_X(R) = 4\pi \int_0^R n(r) r^2 dr, \quad (137)$$

which is a complicated function for general β . For $\beta = 2/3$, which is a commonly measured value,

$$M_X(R) = 4\pi r_c^3 n_0 \left(\frac{R}{r_c} - \arctan \frac{R}{r_c} \right), \quad (138)$$

which is of course formally divergent for $R \rightarrow \infty$ because the density falls off $\propto r^{-2}$ for $\beta = 2/3$ and $r \rightarrow \infty$.

Inserting typical numbers, we set $Z=1=g_{\text{ff}}$, $\beta=2/3$ and assume a hypothetic cluster with $L_X=10^{45}$ erg s $^{-1}$, a temperature of $kT=10$ keV, and a core radius of $r_c=250$ kpc $=7.75 \times 10^{23}$ cm. Then, Eq. (136) yields the central ion density

$$n_0 = 5 \times 10^{-3} \text{ cm}^{-3} \quad (139)$$

and thus the central gas mass density

$$\rho_0 = m_p n_0 = 8.5 \times 10^{-27} \text{ g cm}^{-3}. \quad (140)$$

Based on the virial radius [Eq. (130)] and on the mass [Eq. (138)], we find the total gas mass

$$M_X \approx 1.0 \times 10^{14} M_{\odot}. \quad (141)$$

This is of the same order as the cluster mass in galaxies and approximately one order of magnitude less than the total cluster mass.

It is reasonable to believe that clusters are closed systems in the sense that there cannot have been much material exchange between their interior and their surroundings (White *et al.*, 1993). If this is indeed the case and the mixture between dark matter and baryons in clusters is typical for the entire Universe, the matter-density parameter should be

$$\Omega_{m0} \approx \Omega_{b0} \frac{M}{M_* + M_X} \approx 10\Omega_{b0} \approx 0.4, \quad (142)$$

given determination (111) of Ω_{b0} from primordial nucleosynthesis. More precise estimates based on detailed investigations of individual clusters yield

$$\Omega_{m0} \approx 0.3. \quad (143)$$

3. Alternative cluster mass estimates

Cluster masses can be estimated in several other ways. One of them is directly related to the x-ray emission discussed above. The hydrostatic Euler equation for a gas sphere in equilibrium with the spherically symmetric gravitational potential of a mass $M(r)$ requires

$$\frac{1}{\rho} \frac{dp}{dr} = - \frac{GM(r)}{r^2}, \quad (144)$$

where ρ and p are the gas density and pressure, respectively. Assuming an ideal gas, the equation of state is $p = nkT$, where $n = \rho / \mu m_p$ is the particle density and T is the temperature. μ is the mean particle mass in units of the proton mass m_p . A mixture of hydrogen and helium with helium fraction Y has $\mu = 4/(8-5Y)$ or $\mu \approx 0.59$ for $Y=0.25$. If we further simplify the problem assuming an isothermal gas distribution, we can write

$$\frac{kT}{\mu m_p \rho} \frac{d\rho}{dr} = - \frac{GM(r)}{r^2} \quad (145)$$

or solving for the mass

$$M(r) = - \frac{rkT}{G\mu m_p} \frac{d \ln \rho}{d \ln r}. \quad (146)$$

For the β model introduced in Eq. (134), the logarithmic density slope is

$$\frac{d \ln \rho}{d \ln r} = \frac{d \ln n}{d \ln r} = -3\beta \frac{x^2}{1+x^2}. \quad (147)$$

Thus the cluster mass is determined from the slope of the x-ray surface brightness and the cluster temperature,

$$M(r) = \frac{3\beta rkT}{G\mu m_p} \frac{x^2}{1+x^2}. \quad (148)$$

With the typical numbers used before, i.e., $R \approx 2.5$ Mpc, $\beta \approx 2/3$, and $kT=10$ keV, the x-ray mass estimate gives

$$M(R) \approx 1.8 \times 10^{15} M_{\odot}, \quad (149)$$

in reassuring agreement with the mass estimate (131) from galaxy kinematics and again one order of magnitude larger than either the gas mass or the stellar mass.

A third completely independent way of measuring cluster masses is provided by gravitational lensing. Without going into any detail, we mention here that it can generate image distortions from which the projected lensing mass distribution can be reconstructed. Mass estimates obtained in this way confirm those from x-ray

emission and galaxy kinematics, although interesting discrepancies exist in detail (Cypriano *et al.*, 2004; Hoekstra, 2007).

None of the cluster mass estimates is particularly reliable because they are all to some degree based on stability and symmetry assumptions. For mass estimates based on galaxy kinematics, for instance, assumptions have to be made on the shape of the galaxy orbits, the symmetry of the gravitational potential, and the mechanical equilibrium between orbiting galaxies and the body of the cluster. Numerous assumptions also enter x-ray based mass determinations, such as hydrostatic equilibrium, spherical symmetry, and, in some cases, isothermality of the intracluster gas. Gravitational lensing does not need any equilibrium assumption, but inferences from strongly distorted images depend sensitively on the assumed symmetry of the mass distribution, and measure only the mass enclosed by the lensed images.

C. Mass density from cluster evolution

A conceptually interesting constraint on the cosmic mass density is based on the evolution of cosmic structures. Abell's cluster catalog (Abell *et al.*, 1989) covers the redshift range $0.02 \leq z \leq 0.2$, which encloses a volume of $\approx 9 \times 10^8 \text{ Mpc}^3$. There are 1894 clusters in that volume, which yield an estimate for the spatial cluster density of

$$n_c \approx 2 \times 10^{-6} \text{ Mpc}^{-3}. \quad (150)$$

It is a central assumption in cosmology that structures formed from Gaussian random density fluctuations. The spherical-collapse model then asserts that gravitationally bound objects of mass M form where the linear density contrast, smoothed within spheres of radius R enclosing the average mass M , exceeds a critical threshold of $\delta_c \approx 1.686$, quite independent of cosmology. The probability for this to happen in a Gaussian random field with a standard deviation $\sigma_R(z)$ is

$$p_c(z) = \frac{1}{2} \operatorname{erfc}\left(\frac{\delta_c}{\sqrt{2}\sigma_R(z)}\right), \quad (151)$$

where

$$\sigma_R(z) = \sigma_{R0} D_+(z) \quad (152)$$

because the linear growth of the density contrast is determined by the growth factor, for which a fitting formula was given in Eq. (25).

Now, the present-day standard deviation σ_{R0} must be chosen such as to reproduce the observed number density of clusters given in Eq. (150). The fraction of cosmic matter contained in clusters is given by

$$p'_c = Mn_c \rho_{\text{cr}0} \Omega_{m0} \approx 3 \times 10^{-3} \Omega_{m0}^{-1}. \quad (153)$$

The standard deviation σ in Eq. (151) must now be chosen such that this number is reproduced, which yields

$$\sigma_{R0} \approx \begin{cases} 0.61, & \Omega_{m0} = 1.0 \\ 0.72, & \Omega_{m0} = 0.3. \end{cases} \quad (154)$$

Equations (151) and (152) can now be used to estimate how the cluster abundance should change with redshift. Simple evaluation reveals that the comoving cluster abundance is expected to drop very rapidly with increasing redshift if Ω_{m0} is high and much more slowly if Ω_{m0} is low. Qualitatively, this behavior is easily understood. If, in a low-density universe, clusters do not form early, they cannot form at all because the rapid expansion due to the low matter density prevents them from growing late in the cosmic evolution. From the observed slow evolution of the cluster population as a whole, it can be concluded that the matter density must be low. Estimates arrive at

$$\Omega_{m0} \approx 0.3, \quad (155)$$

in good agreement with the preceding determinations.

D. Conclusions

What does it all mean? The preceding discussion should have demonstrated that the matter density in the Universe is considerably less than its critical value, approximately one-third of it. Since only a small fraction of this matter is visible, we call the invisible majority *dark matter*.

What is this dark matter composed of? Can it be baryons? Tight limits are set by primordial nucleosynthesis, which predicts that the density in baryonic matter should be $\Omega_B \approx 0.04$ [cf. Eq. (111)]. In the framework of the Friedmann-Lemaître models, the baryon density in the Universe can be higher than this only if baryons are locked up in some way before nucleosynthesis commences. They could form black holes before, but their mass is limited by the mass enclosed within the horizon at, say, up to 1 min after the Big Bang. According to Eq. (91), the scale factor at this time was $a \approx 10^{-10}$, and thus the matter density was of order $\rho_m \approx 10^{30} \rho_{\text{cr}0} \approx 10 \text{ g cm}^{-3}$. The horizon size is $r_H \approx ct \approx 1.8 \times 10^{12} \text{ cm}$; thus the mass enclosed by the horizon is $\approx 3 \times 10^4 M_\odot$, which limits possible black-hole masses from above.

Gravitational microlensing was used to constrain the amount of dark compact objects of subsolar mass in the halo of the Milky Way. Although they were found to contribute part of the mass, they can certainly not account for all of it (Alcock *et al.*, 2000; Lasserre *et al.*, 2000). Black holes with masses of the order $10^6 M_\odot$ should have been found through their microlensing effects (Wambsganss and Paczynski, 1992). The abundance of lower-mass black holes is limited by stellar-dynamics arguments in particular by the presence of cold disks (Rix and Lake, 1993; Klessen and Burkert, 1996).

We are thus guided to the conclusion that the dark matter is most probably not baryonic and not composed of compact dark objects. We see in Sec. VI.B.2 why the most favored hypothesis now holds that it is composed of weakly interacting massive particles.

Neutrinos, however, are ruled out because their total mass has been measured to be way too low (<2 eV).² Their correspondingly high velocities require objects more massive than galaxies to keep them bound. The formation of galaxies would be much delayed in this case until larger-scale objects could fragment into smaller pieces. This is the opposite of the observed hierarchy of cosmic structure formation, which shows that galaxies appear substantially earlier than galaxy clusters. Therefore, the conclusion seems inevitable that the dark matter must be cold, i.e., consisting of particles moving nonrelativistically (Peebles, 1982). A sequence of numerical simulations has shown that structure formation in a universe filled with cold dark matter can be brought into agreement with the observed large-scale cosmic structures (Davis *et al.*, 1985; White *et al.*, 1987).

VI. THE COSMIC MICROWAVE BACKGROUND

A. The isotropic CMB

1. Thermal history of the Universe

How does the Universe evolve thermally? We have seen that the abundance of ^4He shows that the Universe must have gone through an early phase which was hot enough for the nuclear fusion of light elements. But was there thermal equilibrium? Thus, can we speak of the “temperature of the Universe?”

From isotropy, we must conclude that the Universe expanded *adiathermally*: no net heat can have flowed between any two volume elements in the Universe because any flow would have singled out a direction, which is forbidden by isotropy. An *adiathermal* process is *adiabatic* if it proceeds slow enough for equilibrium to be maintained. Then, it is also *reversible* and *isentropic*. Of course, irreversible processes must have occurred during the evolution of the Universe. However, as we see later, the entropy in the Universe is so overwhelmingly dominated by the photons of the microwave background radiation that no entropy production by irreversible processes can have added a significant amount of entropy. Thus, we assume that the Universe has in fact expanded adiabatically.

As the Universe expands and cools, particles are diluted and interaction rates drop, so thermal equilibrium must break down at some point for any particle species because collisions become too rare. Very early in the Universe, however, the expansion rate was very high, and it is important to check whether thermal equilibrium can have been maintained despite the rapid expansion. The collision probability between any two particle species will be proportional to their number densities squared, $\propto n^2$, because collisions are dominated by two-body encounters. The collision rate, i.e., the number of collisions experienced by an individual particle with others, will be $\propto n$, which is $\propto a^{-3}$ for nonrelativistic particles. Thus, the collision time scale was $\tau_{\text{coll}} \propto a^3$.

According to Friedmann’s equation, the expansion rate in the very early Universe was determined by the radiation density and thus given by $\dot{a}/a \propto a^{-2}$, and the expansion time scale was $\tau_{\text{exp}} \propto a^2$. Equilibrium could be maintained as long as the collision time scale was sufficiently shorter than the expansion time scale,

$$\tau_{\text{coll}} \ll \tau_{\text{exp}}, \quad (156)$$

which turns out to be well satisfied in the early Universe when $a \ll 1$. Thus, even though the expansion rate was very high in the early Universe, the collision rates were even higher, and thermal equilibrium could indeed be maintained.

The final assumption is that the components of the cosmic fluid behave as ideal gases. By definition, this requires that their particles interact only via short-ranged forces, which implies that partition sums can be written as powers of one-particle partition sums and that the internal energy of the fluids does not depend on the volume occupied. This is a natural assumption which holds even for charged particles because they shield opposite charges on length scales small compared to the size of the observable universe.

It is thus well justified to assume that there was thermal equilibrium between all particle species in the early Universe, that the constituents of the cosmic “fluid” can be described as ideal gases, and that the expansion of the Universe can be seen as an adiabatic process. In later stages of the cosmic evolution, particle species will drop out of equilibrium when their interaction rates fall below the expansion rate of the Universe. As long as all species in the Universe are kept in thermodynamic equilibrium, there is a single temperature characterizing the cosmic fluid. Once particle species drop out of thermal equilibrium because their interaction rates decrease, their temperatures, if defined, may begin deviating. Even then, we characterize the thermal evolution of the Universe by the temperature of the photon background.

2. Mean properties of the CMB

As discussed, the CMB had been predicted in order to explain the abundance of the light elements, in particular of ^4He (Gamow, 1948; Alpher and Herman, 1949). It was serendipitously discovered by Penzias and Wilson in 1965 (Penzias and Wilson, 1965). Measurements of the energy density in this radiation were mostly undertaken at long (radio) wavelengths, i.e., in the Rayleigh-Jeans part of the CMB spectrum. To firmly establish that the spectrum is indeed the Planck spectrum expected for thermal blackbody radiation, the far-infrared absolute spectrophotometer (FIRAS) experiment was placed on board the COBE satellite, where it measured the best realization of a Planck spectrum ever observed (Mather *et al.*, 1994; Fixsen and Mather, 2002).

The temperature of the Planck curve best fitting the latest measurement of the CMB spectrum by the COBE satellite is

²Particle Data Group, <http://pdg.lanl.gov/>

$$T_0 = 2.726 \text{ K}, \quad (157)$$

which implies the mean number density $n_{\text{CMB}} = 405 \text{ cm}^{-3}$ of CMB photons and the energy density $u_{\text{CMB}} = 4.17 \times 10^{-13} \text{ erg cm}^{-3}$ in the CMB, equivalent to a mass density of $\rho_{r,\text{CMB}} = 4.63 \times 10^{-34} \text{ g cm}^{-3}$. Using Eq. (14), the density parameter in radiation is

$$\Omega_{r0} = 8.51 \times 10^{-5}, \quad (158)$$

which shows that the scale factor at matter-radiation equality was

$$a_{\text{eq}} = \frac{\Omega_{m0}}{\Omega_{r0}} \approx \frac{1}{3280} \approx 3.0 \times 10^{-4}. \quad (159)$$

This calculation includes three neutrino species besides the photons, which were relativistic at the time of matter-radiation equality.

The number density of baryons in the Universe is

$$n_B \approx \Omega_{B0} \rho_{\text{cr}} / m_p \approx 2.3 \times 10^{-7} \text{ cm}^{-3}, \quad (160)$$

confirming that the photon-to-baryon ratio is extremely high,

$$\eta^{-1} \approx \frac{405}{2.3 \times 10^{-7}} \approx 1.8 \times 10^9. \quad (161)$$

3. Decoupling of the CMB

When and how was the CMB set free? While the Universe was sufficiently hot to keep electrons and protons separated (we neglect heavier elements here for simplicity), the photons scattered off the charged particles, their mean free path was short, and the photons could not propagate. When the Universe cooled below a certain temperature, electrons and protons combined to form hydrogen, free charges disappeared, the mean free path became virtually infinite, and photons could freely propagate.

The recombination reaction



can thermodynamically be described by Saha's equation for the ionization fraction x ,

$$\begin{aligned} \frac{x^2}{1-x} &= \frac{\sqrt{\pi}}{4\sqrt{2}\zeta(3)\eta} \left(\frac{m_e c^2}{kT} \right)^{3/2} e^{-\chi/kT} \\ &\approx \frac{0.26}{\eta} \left(\frac{m_e c^2}{kT} \right)^{3/2} e^{-\chi/kT}, \end{aligned} \quad (163)$$

where χ is the ionization energy of hydrogen, $\chi = 13.6 \text{ eV}$, and ζ is the Riemann zeta function.

Notice that Saha's equation contains the inverse of the η parameter [Eq. (161)], which is a huge number due to the high photon-to-baryon ratio in the Universe. This counteracts the exponential which would otherwise guarantee that recombination happens when $kT \approx \chi$, i.e., at $T \approx 1.6 \times 10^5 \text{ K}$. Recombination is thus delayed by the high photon number, which illustrates that newly formed hydrogen atoms are effectively reionized by sufficiently

energetic photons until the temperature has dropped well below the ionization energy. Setting $x \approx 0.5$ in Eq. (163) yields a recombination temperature of

$$kT_{\text{rec}} \approx 0.3 \text{ eV}, \quad T_{\text{rec}} \approx 3000 \text{ K} \quad (164)$$

and thus a recombination redshift of $z_{\text{rec}} \approx 1100$. Since this is in the early matter-dominated era, the age of the Universe was then

$$\begin{aligned} t &= \int_0^{a_{\text{rec}}} \frac{da}{aH(a)} = \frac{2a_{\text{rec}}^{3/2}}{3H_0\sqrt{\Omega_{m0}}} [\sqrt{1+\alpha}(1-2\alpha) + 2\alpha^{3/2}] \\ &\approx 374 \text{ kyr} \end{aligned} \quad (165)$$

[cf. Eq. (15)], where $\alpha := a_{\text{eq}}/a_{\text{rec}} \approx 0.33$.

Recombination does not proceed instantaneously. The ionization fraction x drops from 0.9 to 0.1 within a temperature range of $\sim 200 \text{ K}$, corresponding to a redshift range of

$$\Delta z \approx \left. \frac{dz}{dT} \right|_{z_{\text{rec}}} \Delta T \approx \left. \frac{d}{dT} \left(\frac{T}{T_0} - 1 \right) \right|_{z_{\text{rec}}} \Delta T \approx \frac{\Delta T}{T_0} \approx 75 \quad (166)$$

or a time interval of

$$\Delta t \approx \frac{\Delta a}{aH} \approx \frac{\Delta z}{H_0\sqrt{\Omega_{m0}}(1+z)^{5/2}} \approx 50 \text{ kyr}. \quad (167)$$

We are thus led to conclude that the CMB was released when the Universe was $\sim 374\,000 \text{ yr}$ old, during a phase that lasted $\sim 50\,000 \text{ yr}$. We have derived this result merely using the present temperature of the CMB, the photon-to-baryon ratio, the Hubble constant, and the matter-density parameter Ω_{m0} . The cosmological constant or a possible curvature of the Universe does not matter here.

B. Structures in the CMB

1. The dipole

The Earth is moving around the Sun, the Sun is orbiting around the galactic center, and the Galaxy is moving within the local group, which is falling toward the Virgo cluster of galaxies. We can thus not expect the Earth to be at rest with respect to the CMB. We denote the net velocity of the Earth with respect to the CMB rest frame by v_{\oplus} . Lorentz transformation shows that, to lowest order in v_{\oplus}/c , the Earth's motion imprints a dipolar intensity pattern on the CMB with an amplitude of

$$\Delta T/T_0 = v_{\oplus}/c. \quad (168)$$

The dipole's amplitude has been measured to be $\approx 1.24 \text{ mK}$, from which the Earth's velocity is inferred to be (Fixsen *et al.*, 1996)

$$v_{\oplus} \approx 371 \pm 1.5 \text{ km s}^{-1}. \quad (169)$$

This is the highest-order deviation from isotropy in the CMB, but it is irrelevant for our purposes since it does not allow any conclusions on the Universe at large.

2. Expected amplitude of CMB fluctuations

It is reasonable to expect that density fluctuations in the CMB should match density fluctuations in the matter because photons were tightly coupled to baryons by Thomson scattering before recombination. For adiabatic fluctuations, the density contrast δ in matter is $3/4$ that in radiation. Since the radiation density is $\propto T^4$, a density contrast δ is thus expected to produce relative temperature fluctuations of order

$$\delta = \frac{3}{4} \frac{T^3 \delta T}{T^4} \Rightarrow \frac{\delta T}{T} \approx \frac{\delta}{3}. \quad (170)$$

Obviously, there are large-scale structures in the Universe today whose density contrast reaches or even substantially exceeds unity. Assuming linear structure growth on scales where $\delta_0 \approx 1$ and knowing the scale factor at recombination, we can thus infer that relative temperature fluctuations of order

$$\frac{\delta T}{T} \approx \frac{1}{3} \left(\frac{\delta_0}{D_+(a_{\text{rec}})} \right) \approx \frac{1}{3a_{\text{rec}}} \approx 10^{-3} \quad (171)$$

should be seen in the CMB, i.e., fluctuations of order mK, similar to the dipole. Such fluctuations, however, were not observed, although cosmologists kept searching increasingly desperately for decades after 1965 [see [Uson and Wilkinson \(1984\)](#) for an example].

Why do they not exist? The estimate above is valid only under the assumption that matter and radiation were tightly coupled. Should this not have been the case, density fluctuations did not need to leave such a pronounced imprint on the CMB. In order to avoid the tight coupling, the majority of matter must not interact electromagnetically. Thus, we conclude from the absence of mK fluctuations in the CMB that matter in the Universe must be dominated by something that does not interact with light ([Peebles, 1982](#)). This is perhaps the strongest argument in favor of not-electromagnetically interacting dark matter.

3. Expected CMB fluctuations

Before we come to the results of CMB observations and their significance for cosmology, we summarize which physical effects we expect to imprint structures on the CMB ([Peebles and Yu, 1970](#); [Sunyaev and Zeldovich, 1970](#); [Bond and Efstathiou, 1984](#); [Hu and Sugiyama, 1996](#); [Seljak and Zaldarriaga, 1996](#)). The basic hypothesis is that the cosmic structures that we see today formed via gravitational instability from seed fluctuations in the early Universe, whose inflationary origin is likely but yet unclear. This implies that there had to be density fluctuations at the time when the CMB was released. Via Poisson's equation, these density fluctuations were related to fluctuations in the Newtonian potential. Photons released in a potential fluctuation $\delta\Phi$ lost energy if the fluctuation was negative and gained energy when the fluctuation was positive. This energy change can be translated to the temperature change

$$\frac{\delta T}{T} = \frac{1}{3} \frac{\delta\Phi}{c^2}, \quad (172)$$

which is called the Sachs-Wolfe effect ([Sachs and Wolfe, 1967](#)). The factor $1/3$ is caused by the gravitational redshift being offset by time retardation in the gravitational field of the perturbation.

We now look into the expected statistics of the Sachs-Wolfe effect. We introduced the power spectrum of the density fluctuations in Eq. (27) as the variance of the density contrast in Fourier space. Poisson's equation implies

$$\delta\hat{\Phi} \propto -\hat{\delta}/k^2 \quad (173)$$

for the Fourier modes of the gravitational potential. Thus the power spectrum of the temperature fluctuations due to the Sachs-Wolfe effect is

$$P_T \propto P_\Phi \propto \frac{\langle \hat{\delta}\hat{\delta}^* \rangle}{k^4} \propto \frac{P_\delta}{k^4} \propto \begin{cases} k^{-3}, & k \ll k_{\text{eq}} \\ k^{-7}, & k \gg k_{\text{eq}} \end{cases} \quad (174)$$

according to Eq. (28) with $n_s=1$. This shows that the Sachs-Wolfe effect can only be important at small k , i.e., on large scales, and dies off quickly toward smaller scales.

The main constituents of the cosmic fluid were dark matter, baryons, electrons, and photons. Overdensities in the dark matter compressed the fluid due to their gravity until the rising pressure in the tightly coupled baryon-electron-photon fluid was able to counteract gravity and drive the fluctuations apart. In due course, the pressure sank, gravity won again, and so forth: the baryon-electron-photon fluid underwent acoustic oscillations but not the dark matter, which was decoupled. Since the pressure was dominated by the photons, whose pressure is a third of their energy density, a good approximation to the sound speed of the tightly coupled photon-baryon fluid was

$$c_s \approx \sqrt{\frac{p}{\rho}} = \frac{c}{\sqrt{3}} \approx 0.58c. \quad (175)$$

Only such density fluctuations could undergo acoustic oscillations which were small enough to be crossed by sound waves in the available time. The largest comoving length that could be traveled by sound waves was the comoving sound horizon,

$$w_s = \int_0^{t_{\text{rec}}} \frac{c_s dt}{a} = \frac{2c_s \sqrt{a_{\text{rec}}}}{H_0 \sqrt{\Omega_{m0}}} (\sqrt{1+\alpha} - \sqrt{\alpha}) = 163.3 \text{ Mpc}. \quad (176)$$

Larger-scale density fluctuations could not oscillate. We saw in Eqs. (18) and (19) that the *comoving* angular-diameter distance from today to scale factor a_{rec} is $f_K[w(a_{\text{rec}})] = w(a_{\text{rec}})$ if we assume spatial flatness, $K=0$. In good approximation,

$$f_K[w(a_{\text{rec}})] = w(a_{\text{rec}}) = 3.195 \frac{c}{H_0} \left(\frac{\Omega_{m0}}{0.3} \right)^{-0.4}. \quad (177)$$

Thus, the sound horizon sets an angular scale of

$$\theta_s = w_s/w(a_{\text{rec}}) = 0.66^\circ. \quad (178)$$

This angular scale can be read off the first acoustic peak in the CMB power spectrum (see Sec. VI.B.5 below). Its relation to the physical sound horizon [Eq. (176)] depends almost precisely on the sum of Ω_{m0} and $\Omega_{\Lambda 0}$ if all else remains fixed. Thus, the location of the first acoustic peak determines the spatial curvature of the cosmological model. When combined with measurements of H_0 , latest data (cf. Table I) show that $K=0$ to high precision.

A third effect influencing structures in the CMB is caused by the fact that, as recombination proceeds, the mean-free path of the photons increases. If $n_e = xn_B$ is the electron number density and σ_T is the Thomson cross section, the comoving mean-free path is

$$\lambda \approx (xn_B\sigma_T)^{-1}. \quad (179)$$

As the ionization fraction x drops toward zero, the mean-free path approaches infinity. After N scatterings, the photons will have diffused by

$$\lambda_D \approx \sqrt{N}\lambda \quad (180)$$

on average. The number of scatterings per unit time is

$$dN \approx xn_B\sigma_T c dt, \quad (181)$$

and thus the diffusion scale is given by

$$\lambda_D^2 \approx \int \lambda^2 dN \approx \int \frac{cdt}{xn_B\sigma_T}. \quad (182)$$

Inserting $x \approx 1/2$ as a typical value into the latter integrand, we find

$$\lambda_D^2 \approx \frac{2c\Delta t}{n_B\sigma_T}. \quad (183)$$

Numerical evaluation returns a comoving damping length of order 50 Mpc, corresponding to angular scales of $\theta_D \approx 10'$ on the sky. The effect of this diffusion process is called Silk damping (Silk, 1968). We thus expect three principal mechanisms to shape the appearance of the microwave sky: the Sachs-Wolfe effect on the largest scales, the acoustic oscillations on scales smaller than the sound horizon, and Silk damping on scales smaller than a few arcminutes.

4. CMB polarization

If the CMB does indeed arise from Thomson scattering, interesting effects must occur because the Thomson scattering cross section is polarization sensitive and can thus convert unpolarized into linearly polarized radiation. Suppose an electron is illuminated by unpolarized radiation from the left, then radiation scattered toward the observer will be linearly polarized in the perpendicular direction. Likewise, unpolarized radiation incoming from the top will be linearly polarized horizontally after

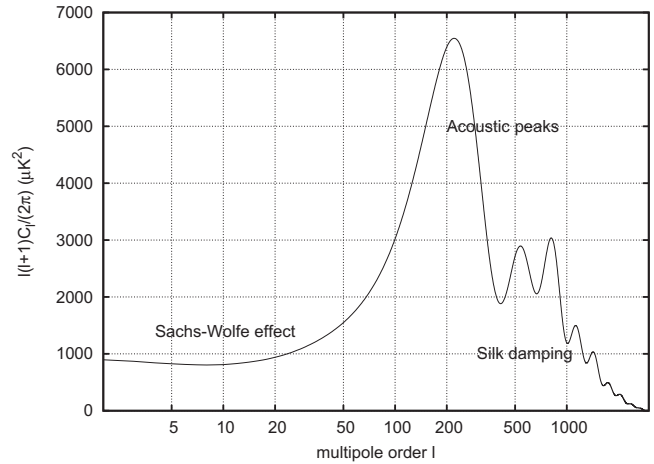


FIG. 7. Schematic appearance of the CMB power spectrum due to the three dominating physical effects defining its shape: the Sachs-Wolfe effect on largest scales, the Silk damping on smallest scales, and the acoustic oscillations in between.

being scattered toward the observer. Thus, if the electron is irradiated by a quadrupolar intensity pattern, scattered radiation will be partially linearly polarized. The polarized intensity is expected to be of order 10% of the total intensity. Polarized radiation must reflect the same physical effects as unpolarized radiation, and the two must be cross correlated. Much additional information on the physical state of the early Universe is thus contained in the polarized component of the CMB, apart from the fact that the mere detection of polarization supports the physical picture of the CMB's origin.

5. The CMB power spectrum

Fourier transformation is impossible on the sphere, but analysis of the CMB proceeds in a completely analogous way by decomposing the relative temperature fluctuations into spherical harmonics, finding the spherical-harmonic coefficients

$$a_{lm} = \int d^2\theta \frac{\delta T}{T} Y_{lm}(\vec{\theta}), \quad (184)$$

and from them the power spectrum

$$C_l \equiv \frac{1}{2l+1} \sum_{m=-l}^l |a_{lm}|^2, \quad (185)$$

which is the equivalent on the sphere to the three-dimensional power spectra defined in Eq. (27). The average over m expresses the expectation of statistical isotropy. If parts of the observed sky need to be masked, care has to be taken to orthonormalize the spherical harmonics on the remaining domain (see Fig. 7).

The shape of the CMB power spectrum reflects the three physical mechanisms identified above: at small l (on large scales), the Sachs-Wolfe effect causes a featureless plateau, followed by pronounced maxima and minima due to the acoustic oscillations, damped on the smallest scales (largest l) by Silk damping.

The detailed shape of the CMB power spectrum depends sensitively on the cosmological parameters, which can in turn be determined by fitting the theoretically expected to the measured C_l . This is the main reason for the detailed and sensitive CMB measurements pioneered by COBE, continued by ground-based and balloon experiments, and culminating recently in the spectacular results obtained by the Wilkinson microwave anisotropy probe (WMAP) satellite.

6. Secondary anisotropies and foregrounds

By definition, the CMB is the oldest visible source of photons because all possible earlier sources could not shine through the hot cosmic plasma. Therefore, every source that produced microwave photons since or that produced photons which became redshifted into the microwave regime by now must appear superposed on the CMB. The CMB is thus covered by layers of foreground emission that have to be unveiled before the CMB can be observed.

Broadly, the CMB foregrounds can be grouped into point sources and diffuse sources. The most important among the point sources are infrared galaxies at high redshift and bodies in the Solar System such as the major planets and even some of the asteroids.

The population of infrared sources at high redshift is poorly known, but the angular resolution of CMB measurements has so far been too low to be significantly contaminated by them. Future CMB observations will have to remove them carefully (Toffolatti *et al.*, 1998).

Microwave radiation from bodies in the Solar System has so far been used to calibrate microwave detectors. CMB observations at an angular resolution below $\sim 10'$ are expected to detect hundreds of minor planets.

Diffuse CMB foregrounds are mainly caused by our Galaxy itself. There are three main components: synchrotron emission, emission from warm dust, and bremsstrahlung (Haslam *et al.*, 1982; Schlegel *et al.*, 1998; Dame *et al.*, 2001; Finkbeiner, 2003).

Synchrotron radiation is emitted by relativistic electrons in the Galaxy's magnetic field. It is highly linearly polarized and has a power-law spectrum falling steeply from radio toward microwave frequencies. It is centered on the Galactic plane but shows filamentary extensions from the Galactic center toward the Galactic poles.

The dust in the Milky Way is also concentrated in the Galactic plane. It is between 10 and 20 K warm and thus substantially warmer than the CMB itself. It has a thermal spectrum modified by frequency-dependent self-absorption. Due to its higher temperature, the warm dust has a spectrum rising with increasing frequency in the frequency window where the CMB is usually observed.

Bremsstrahlung radiation is emitted by ionized hydrogen clouds (HII regions) in the galactic plane. Its spectrum has the shape typical for thermal free-free radiation, falling exponentially at photon energies near and above the gas temperature, but it is flat at CMB frequencies. Further sources of microwave radiation in the Gal-

axy are less prominent. Among them are line emission from CO molecules embedded in cool gas clouds.

The falling synchrotron spectrum, the flat spectrum of the free-free radiation, and the rising spectrum of the warm dust create a window for CMB observations between ~ 100 and 200 GHz. The different spectra of the foregrounds and their non-Planckian character are crucial for their proper removal from the CMB data. Therefore, CMB measurements have to be carried out in multiple frequency bands.

Secondary anisotropies are caused by propagation effects rather than photon emission. The most important are the integrated Sachs-Wolfe effect and the (thermal and kinetic) Sunyaev-Zel'dovich effects in galaxy clusters.

The integrated Sachs-Wolfe effect is caused by gravitational potential wells deepening while crossed by CMB photons. It is determined by the line-of-sight integral of the time derivative of the potential fluctuations caused by the density fluctuations between us and the CMB. By cross-correlating CMB temperature fluctuations with structures in the galaxy distribution, the integrated Sachs-Wolfe effect has indeed been detected (Gaztañaga *et al.*, 2006; Giannantonio *et al.*, 2006). It constrains the ratio $D_+(a)/a$.

The Sunyaev-Zel'dovich effect (Sunyaev and Zeldovich, 1972) is due to inverse Compton scattering of CMB photons off hot electrons in the intracluster plasma. On average, the photons gain energy and are thus moved from the low- to the high-frequency part of the spectrum. When observed through a galaxy cluster, the CMB therefore appears fainter at low and brighter at high frequencies, with the transition at 217 GHz. This gives galaxy clusters a peculiar spectral signature in the microwave regime as they cast shadows below, emit above, and vanish at 217 GHz. Once the angular resolution of CMB detectors will drop toward a few arcminutes, a large number of galaxy clusters are expected to show up in this way. Besides this thermal Sunyaev-Zel'dovich effect, there is the *kinetic* effect caused by the bulk motion of the cluster as a whole, which causes CMB radiation to be scattered by the electrons moving with the cluster. Very few clusters have so far been detected in CMB data, but thousands are expected to be found in future missions.

7. Measurements of the CMB

Wien's law [Eq. (114)] shows that the CMB spectrum peaks at $\lambda_{\max} \approx 0.11$ cm or at a frequency of $\nu_{\max} \approx 282$ GHz. As we saw, Silk damping sets in below $\sim 10'$ arc min; thus most of the structures in the CMB are resolvable for rather small telescopes. According to

$$\Delta\theta \approx 1.44\lambda/D \quad (186)$$

relating the diffraction-limited angular resolution $\Delta\theta$ to the ratio between wavelength and telescope diameter D , we find that mirrors with

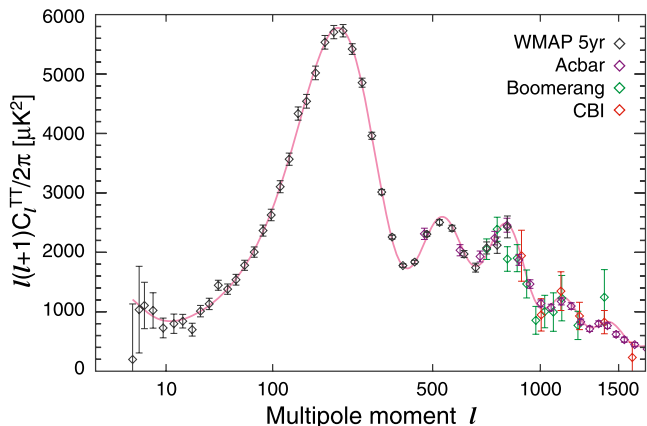


FIG. 8. (Color online) Power spectrum of CMB temperature fluctuations as measured from the 5-yr data of WMAP and several additional ground-based experiments. From [Nolta et al., 2009](#).

$$D \lesssim 1.44\lambda_{\max}/\theta_D \approx 55 \text{ cm} \quad (187)$$

are sufficient to achieve sufficient angular resolution up to the Silk damping scale θ_D . Detectors are needed which are sensitive to millimeter and submillimeter radiation and reach μK sensitivity, while the telescope optics can be kept rather small and simple (see Fig. 8).

Two types of detector are commonly used. The first are bolometers, which measure the energy of the absorbed radiation by the temperature increase it causes. They have to be cooled to very low temperatures, typically in the mK regime. The second are so-called high electron mobility detectors, in which the currents caused by the incoming electromagnetic field are measured directly. They measure amplitude and phase of the waves and are thus polarization sensitive by construction, which bolometers are not. Polarization measurements with bolometers are possible with suitably shaped so-called *feed horns* guiding the radiation into the detectors.

Since water vapor in the atmosphere both absorbs and emits microwave radiation through molecular lines, CMB observations need to be carried out at high dry and cold sites on the ground (e.g., in the Chilean Andes or at the South Pole), from balloons rising above the troposphere, or from satellites in space.

After the breakthrough achieved with COBE ([Boggett et al., 1992](#)), progress was made with balloon experiments and with ground-based interferometers. The balloons covered a small fraction of the sky (typically $\sim 1\%$) at frequencies between 90 and 400 GHz, while the interferometers observe even smaller fields at somewhat lower frequencies (typically around 30 GHz).

The first discovery of the CMB polarization and its cross correlation with the CMB temperature was achieved with the degree angular scale interferometer (DASI) ([Kovac et al., 2002](#)). The existence, location, and height of the first acoustic peak had been firmly established ([Wang et al., 2003](#)) before the NASA satellite WMAP was launched, but the increased sensitivity and

the full-sky coverage of WMAP produced breath-taking results ([Spergel et al., 2007](#)). WMAP is still operating, measuring the CMB temperature at frequencies between 23 and 94 GHz with an angular resolution of $\geq 15'$. The sensitivity of WMAP is barely high enough for polarization measurements.

By now, data from the first five years of operation have been published, and cosmological parameters have been obtained fitting theoretically expected to the measured temperature-fluctuation power spectrum and the temperature-polarization power spectrum. Results are given in Table I, adapted from [Komatsu et al. \(2009\)](#).

Although the CMB provides insight into the cosmological parameters on its own, it is most powerful when combined with other data sets. In particular, the Hubble constant is not an independent measurement from the CMB alone. Only by assuming a flat ΛCDM universe, it can be inferred from the location of the first acoustic peak in the CMB power spectrum to be $H_0 = 70.1 \pm 1.3 \text{ km s}^{-1} \text{ Mpc}^{-1}$, which agrees perfectly with the results of the Hubble key project and at least one interpretation of the gravitational-lens time delays.

A European CMB satellite mission is under way: the European Space Agency's Planck satellite has been launched in May 2009. It will observe the microwave sky in nine frequency bands between 30 and 857 GHz with about ten times higher sensitivity than WMAP and an angular resolution of $\geq 5'$ ([Tauber, 2004](#)). Its wide frequency coverage will be important for substantially improved foreground subtraction. It will also have sufficient sensitivity to precisely measure the CMB polarization in some of its frequency bands ([Lamarre et al., 2003](#); [Valenziano et al., 2007](#)). Moreover, it is expected that Planck will detect a large number of galaxy clusters through their thermal Sunyaev-Zel'dovich effect.

VII. COSMIC STRUCTURES

A. Quantifying structures

1. Introduction

We have seen before that there is a very specific prediction for the power spectrum of cold dark matter-density fluctuations in the Universe, characterized by Eq. (28). Recall that its shape was inferred from the simple assumption that the rms mass of density fluctuations entering the horizon should be independent of the time when they enter the horizon and from the fact that perturbation modes entering during the radiation era are suppressed until matter begins dominating. Given the simplicity of the argument and the corresponding strength of the prediction, it is important for cosmology to find out whether the actual power spectrum of matter-density fluctuations does in fact have the expected *shape*, and if it has, to determine the only remaining parameter, i.e., the *normalization* of the power spectrum.

Since the comoving wave number k_{eq} of the peak in the power spectrum is set by the comoving horizon radius at matter-radiation equality [Eq. (26)],

$$k_{\text{eq}} \propto \frac{2\pi}{w_{\text{eq}}} \propto \left(\frac{\Omega_{m0}}{a_{\text{eq}}} \right)^{1/2} = \frac{\Omega_{m0}}{\sqrt{\Omega_{r0}}}, \quad (188)$$

it is proportional to the matter-density parameter Ω_{m0} . A measurement of k_{eq} would thus provide an independent and very elegant determination of Ω_{m0} .

Since the power spectrum is defined in Fourier space, it is not obvious how it should be measured. The correlation function is related to the power spectrum by

$$\xi(x) = \frac{1}{2\pi^2} \int_0^\infty P(k) \frac{\sin kx}{kx} k^2 dk, \quad (189)$$

whose inverse transform is

$$P(k) = 4\pi \int_0^\infty \xi(x) \frac{\sin kx}{kx} x^2 dx. \quad (190)$$

The power spectrum can thus in principle be determined from a measured correlation function $\xi(x)$.

2. Measuring the correlation function

The correlation function of the three-dimensional density field cannot be measured directly. Gravitational lensing by large-scale structures comes close by measuring the weighed line-of-sight projection of the matter power spectrum (see Sec. VIII). Starting from the assumption that galaxies may be tracers of the underlying density field, we can use their correlation function as an estimate for that of the matter.

Suppose we divide space into cells of volume dV small enough to contain at most a single galaxy. Then, the probability of finding one galaxy in dV_1 and another in dV_2 is

$$dP = \langle n(\vec{x}_1)n(\vec{x}_2) \rangle dV_1 dV_2, \quad (191)$$

where n is the number density of the galaxies as a function of position. If we introduce a density contrast for the galaxies in analogy to the density contrast for the matter,

$$\delta n \equiv n/\bar{n} - 1, \quad (192)$$

and assume for now that $\delta n = \delta$, we find from Eq. (191) with $n = \bar{n}(1 + \delta)$,

$$\begin{aligned} dP &= \bar{n}^2 \langle (1 + \delta_1)(1 + \delta_2) \rangle dV_1 dV_2 \\ &= \bar{n}^2 [1 + \xi(x)] dV_1 dV_2, \end{aligned} \quad (193)$$

where x is the comoving distance between the two volume elements. This shows that the correlation function quantifies the excess probability above random for finding galaxy pairs at a given distance.

Thus, the correlation function can be measured by counting galaxy pairs and comparing the result to the Poisson expectation, i.e., to the pair counts expected in a *random* point distribution. Symbolically,

$$1 + \xi = \langle DD \rangle / \langle RR \rangle, \quad (194)$$

where D and R represent the data and the random point set, respectively. Several other estimators for ξ have been proposed which are all equivalent in the ideal situation of an infinitely extended point distribution. For finite point sets, their noise properties differ (Hamilton, 1993b; Landy and Szalay, 1993). The recipes for measuring $\xi(x)$ are thus to count pairs separated by x in the data D and in the random point set R or between the data and the random point set and to use one of the estimators proposed.

The obvious question is then how accurately ξ can be determined. The simple expectation in the absence of clustering is

$$\langle \xi \rangle = 0, \quad \langle \xi^2 \rangle = 1/N_p, \quad (195)$$

where N_p is the number of pairs found. Thus, the Poisson error on the correlation function is

$$\Delta \xi / (1 + \xi) = 1/\sqrt{N_p}. \quad (196)$$

This is a lower limit to the actual error, however, because the galaxies are in fact correlated. It turns out that the result (196) should be multiplied with $1 + 4\pi\bar{n}J_3$, where J_3 is the volume integral over ξ within the galaxy-survey volume (Peebles, 1973). The true error bars on ξ are therefore hard to estimate.

Having measured the correlation function, it would in principle suffice to carry out the Fourier transform [Eq. (190)] to find $P(k)$, but this is difficult in reality because of the inevitable sample limitations. Consider Eq. (189) and an underlying power spectrum of CDM shape, falling off $\propto k^{-3}$ for large k , i.e., on small scales. For fixed x , the integrand in Eq. (189) falls off very slowly, which means that a considerable amount of small-scale power is mixed into the correlation function. Since ξ at large x is small and most affected by measurement errors, any uncertainty in the large-scale correlation function is propagated to the power spectrum even on small scales.

A further problem is the uncertainty in the mean galaxy number density \bar{n} . Since $1 + \xi \propto \bar{n}^{-1}$ according to Eq. (193), the uncertainty in ξ due to an uncertainty in \bar{n} is

$$\Delta \xi / (1 + \xi) \approx \Delta \bar{n} / \bar{n}, \quad (197)$$

showing that ξ cannot be measured with an accuracy better than the relative accuracy of the mean galaxy density.

3. Measuring the power spectrum

Given these problems with real data, it seems appropriate to estimate the power spectrum directly. The function to be transformed is the density field sampled by the galaxies, which can be represented by a sum of Dirac delta functions centered on the locations of the N galaxies,

$$n(\vec{x}) = \sum_{i=1}^N \delta_D(\vec{x} - \vec{x}_i). \quad (198)$$

The Fourier transform of the galaxy density contrast is then

$$\hat{\delta}_g(\vec{k}) = \frac{1}{N} \sum_{i=1}^N e^{i\vec{k}\cdot\vec{x}_i}. \quad (199)$$

In the absence of correlations, the Fourier phases of the individual terms are independent, and the variance of the Fourier amplitude for a single mode becomes

$$\langle \hat{\delta}_g(\vec{k}) \hat{\delta}_g^*(\vec{k}) \rangle = \frac{1}{N^2} \sum_{i=1}^N e^{i\vec{k}\cdot\vec{x}_i} e^{-i\vec{k}\cdot\vec{x}_i} = \frac{1}{N}. \quad (200)$$

This is the so-called shot noise present in the power spectrum due to the discrete sampling of the density field. The shot-noise contribution needs to be subtracted from the power spectrum of the real correlated galaxy distribution,

$$P(k) = \frac{1}{m} \sum |\hat{\delta}_g(\vec{k})|^2 - \frac{1}{N}, \quad (201)$$

where the sum extends over all m Fourier modes with wave number k contained in the survey.

This is not the final result yet because any real survey typically covers an irregularly shaped volume from which parts need to be excised because they are overhauled by stars or unusable for any other reason. The combined effect of mask and irregular survey volume is described by a window function $f(\vec{x})$ which multiplies the galaxy density,

$$n(\vec{x}) \rightarrow f(\vec{x})n(\vec{x}), \quad (1 + \delta_g) \rightarrow f(\vec{x})(1 + \delta_g), \quad (202)$$

implying that the Fourier transform of the mask needs to be subtracted.

Moreover, the Fourier convolution theorem says that the Fourier transform of the *product* $f(\vec{x})\delta_g(\vec{x})$ is the *convolution* of the Fourier transforms $\hat{f}(\vec{k})$ and $\hat{\delta}_g(\vec{k})$,

$$\widehat{f\delta} = \hat{f} * \hat{\delta}_g \equiv \int \hat{f}(\vec{k}') \hat{\delta}_g(\vec{k} - \vec{k}') d^3k'. \quad (203)$$

If the Fourier phases of \hat{f} and $\hat{\delta}_g$ are uncorrelated, which is the case if the dimensions of the survey are large enough compared to the size $2\pi/k$ of the density mode, this translates to a convolution of the power spectrum,

$$P_{\text{obs}} = P_{\text{true}} * |\hat{f}(\vec{k})|^2. \quad (204)$$

This convolution smoothes the observed compared to the true power spectrum and changes its amplitude.

If the Poisson error dominates in the survey, the different modes $\hat{\delta}_g(\vec{k})$ can be shown to be uncorrelated, and the standard deviation after summing over the m modes with wave number k is $\sqrt{2m}/N$, which yields the minimal error bar to be attached to the power spectrum.

Thus, the shot-noise contribution and the Fourier transform of the window function need to be subtracted,

the window function needs to be deconvolved, and the amplitude needs to be corrected for the effective volume covered by the window function before the measured power spectrum can be compared to the theoretical expectation.

4. Biasing

What we have determined so far is the power spectrum of the galaxy number-density contrast δn rather than that of the matter-density contrast δ . Both are related by a possibly scale-dependent bias factor $b(k)$, such that

$$\widehat{\delta n}(\vec{k}) = b(k) \hat{\delta}_g(\vec{k}). \quad (205)$$

Clearly, different types of objects sample the underlying matter-density field in different ways. Galaxy clusters, for instance, are much more rare than galaxies and are thus expected to have a substantially higher bias factor than galaxies. Obviously, the bias factor enters the power spectrum squared, e.g.,

$$P_{\text{gal}} = b_{\text{gal}}^2(k) P(k). \quad (206)$$

It constitutes a major and possibly systematic uncertainty in the determination of the matter power spectrum from the galaxy power spectrum.

5. Redshift-space distortions

For any quantification of three-dimensional structures in galaxy surveys, the three-dimensional positions \vec{x}_i of the galaxies in the survey need to be known. Distances can be inferred only from the galaxy redshifts and thus from galaxy velocities. These, however, are composed of the Hubble velocities, from which the distances can be determined, and the peculiar velocities,

$$\mathbf{v} = \mathbf{v}_{\text{Hubble}} + \mathbf{v}_{\text{pec}}, \quad (207)$$

which are caused by local density perturbations and are unrelated to the galaxy densities. Since observations of individual galaxies do not allow any separation between the two velocity components, distances are inferred from the total velocity v rather than the Hubble velocity as they should be,

$$D = \frac{v}{H_0} = \frac{v_{\text{Hubble}} + v_{\text{pec}}}{H_0} = D_{\text{true}} + \Delta D, \quad (208)$$

giving rise to a distance error $\delta D = v_{\text{pec}}/H_0$, the so-called redshift-space distortion.

The redshift-space distortions create a peculiar pattern through which they can be corrected (Kaiser, 1987; Hamilton 1993a). Consider a matter overdensity such as a galaxy cluster, containing galaxies moving with random virial velocities in it. The virial velocities of order 1000 km s^{-1} scatter around the systemic cluster velocity and thus broaden the redshift distribution of the cluster galaxies. In redshift space, therefore, the cluster appears stretched along the line of sight, which is called the *finger-of-god* effect.

In addition, the cluster is surrounded by an infall region where the galaxies are not virialized yet but move in an ordered radial pattern toward the cluster. Galaxies in front of the cluster thus have higher recession velocities and galaxies behind the cluster have lower recession velocities compared to the Hubble velocity, leading to a flattening of the infall region in redshift space.

A detailed analysis shows that the redshift-space power spectrum P_z is related to the real-space power spectrum P by

$$P_z(k) = P(k)(1 + \beta\mu^2)^2, \quad (209)$$

where μ is the direction cosine between the line of sight and the wave vector \vec{k} and β is related to the bias parameter b through

$$\beta \equiv f(\Omega_m)/b. \quad (210)$$

$f(\Omega_m)$ is the logarithmic derivative of the growth factor $D_+(a)$,

$$f(\Omega_m) \equiv d \ln D_+(a)/d \ln a \approx \Omega_m^{0.6}. \quad (211)$$

Thus, the characteristic pattern of the redshift-space distortions around overdensities allows a measurement of the bias factor (Hawkins *et al.*, 2003). Another way of measuring b is based on gravitational lensing (Hoekstra, van Waerbeke, *et al.*, 2002; Simon *et al.*, 2007). Measurements of b show that it is in fact only weakly scale dependent, near unity for “ordinary” galaxies, but depends mildly on galaxy luminosity and type (Norberg *et al.*, 2001; Lahav *et al.*, 2002; Cole *et al.*, 2005).

6. Baryonic acoustic oscillations

As seen in the discussion of the CMB, the cosmic fluid underwent acoustic oscillations on comoving scales smaller than the sound horizon [Eq. (176)] $w_s = 163.3$ Mpc, corresponding to a comoving wave number $k_s = 2\pi/w_s = 0.038$ Mpc⁻¹. When the CMB decoupled, the oscillations ceased, leaving structures in the cosmic matter distribution with a fundamental wavelength of w_s and its overtones. The other scale characterizing the cosmic structures is the horizon radius at matter-radiation equality (26), which was responsible to set the peak location of the matter-fluctuation power spectrum at $k_{\text{eq}} = 0.01$ Mpc⁻¹.

Thus, at wave numbers ≈ 3.8 times the peak scale and above, we expect the wavelike imprint of these baryonic acoustic oscillations (BAOs) on top of the otherwise smooth dark-matter power spectrum. Mode coupling due to nonlinear evolution of cosmic structures must have stretched and distorted this pattern to some degree. As we see below, the BAOs have indeed been discovered in the largest galaxy surveys. They play an important role in attempts to recover the history of the cosmic expansion rate [see Eisenstein (2005) for a recent review].

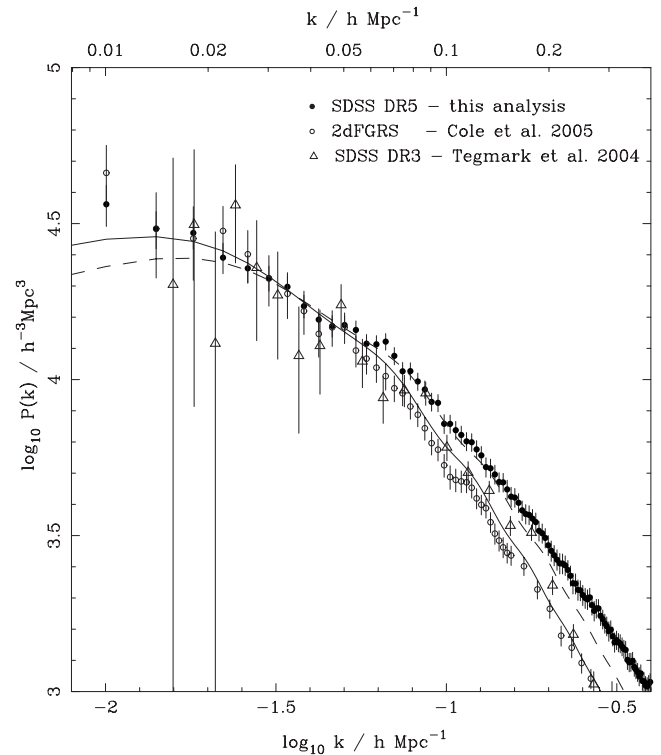


FIG. 9. Galaxy power spectra obtained from the 2dFGRS (Cole *et al.*, 2005) and two releases of the SDSS (Tegmark *et al.*, 2004; Percival *et al.*, 2007). The expected shape of the CDM power spectrum is well reproduced, and the difference in amplitudes may be attributed to scale-dependent galaxy biasing. From Percival *et al.*, 2007.

B. Measurements and results

1. The power spectrum

Successful measurements of the galaxy power spectrum became recently possible with the two largest galaxy surveys to date, the *Two-Degree Field Galaxy Redshift Survey* (2dFGRS) (Colless 1999) and the *Sloan Digital Sky Survey* (SDSS) (York *et al.*, 2000). As anticipated in the preceding discussion, an enormous effort had to be made to identify galaxies, measure their redshifts, select homogeneous galaxy subsamples by luminosity and color as a function of redshift so as not to compare and correlate apples with oranges, estimate the window function of the survey, determine the average galaxy number density, correct for the convolution with the window function and for the bias, and so forth (see Fig. 9).

Moreover, numerical calibration experiments were carried out in which all measurement and correction techniques were applied to simulated data in the same way as to the real data to determine reliable error estimates and to test whether the full sequence of analysis steps ultimately yields an unbiased result.

Based on 221 414 galaxies, the 2dFGRS consortium derived a power spectrum of superb quality (Cole *et al.*, 2005). First and foremost, it agrees well with the power-spectrum shape expected for cold dark matter on the

small-scale side of the peak. This is a remarkable result on its own. The 2dFGRS power spectrum also shows a turnover toward larger scales, signaling the presence of the peak. The survey is still not quite large enough to clearly show the peak, but the peak location can be estimated from the flattening of the power spectrum. Its proportionality to Ω_{m0} allows an independent determination of the matter-density parameter. Finally the power spectrum shows the baryonic acoustic oscillations, whose amplitude allows an independent determination of the ratio between the density parameters of baryons and dark matter.

Apart from the fact that the galaxy power spectrum supports the CDM shape on small scales, the results obtained from the 2dFGRS can be summarized as follows:

$$\Omega_{m0} = 0.233 \pm 0.022, \quad \Omega_{b0}/\Omega_{m0} = 0.185 \pm 0.046. \quad (212)$$

A Hubble constant of $h=0.72$ is assumed here. Indirectly, the baryon density is constrained to be $\Omega_{b0} \approx 0.04$, which is in perfect agreement with the value derived from primordial nucleosynthesis and the measured abundances of the light elements.

Based on 522 280 galaxies, the power spectrum inferred from the SDSS (Percival *et al.*, 2007) is also well compatible with the CDM shape. The estimate for the matter-density parameter overlaps with that from the 2dFGRS on large scales, $\Omega_{m0}=0.22 \pm 0.04$, but increases when small scales are included.

It should be kept in mind, however, that the assumption of linear biasing may turn out to be too simplistic for precise cosmological inferences to be drawn from galaxy power spectra. Nonetheless, power spectra for different types of galaxies will provide invaluable information on the physics of galaxy formation.

VIII. COSMOLOGICAL WEAK LENSING

A. Cosmological light deflection

1. Deflection angle, convergence, and shear

Gravitational lensing was mentioned twice before: first in Sec. III.B as a means for measuring the Hubble constant through the time delay caused by gravitational light deflection and second as a means for measuring cluster masses in Sec. V.B.3. For cosmology as a whole, gravitational lensing has also developed into an increasingly important tool [see Mellier (1999), Bartelmann and Schneider (2001), and Refregier (2003) for reviews].

Matter inhomogeneities deflect light. Working out this effect in the limit of a small Newtonian gravitational potential, $\Phi \ll c^2$, leads to the deflection angle

$$\vec{\alpha}(\vec{\theta}) = \frac{2}{c^2} \int_0^w dw' \frac{f_K(w-w')}{f_K(w)} \vec{\nabla}_\perp \Phi[f_K(w') \vec{\theta}]. \quad (213)$$

The angle is determined by a weighted integral over the gradient of the Newtonian gravitational potential Φ perpendicular to the line of sight into direction $\vec{\theta}$ on the

observer's sky, and the weight is given by the comoving angular-diameter distance $f_K(w)$ defined in Eq. (2). The integral extends along the comoving radial distance w' along the line of sight to the distance w of the source.

Equation (213) can be intuitively understood. Light is deflected due to the pull of the dimensionless Newtonian gravitational field $\vec{\nabla}_\perp \Phi/c^2$ perpendicular to the otherwise unperturbed line of sight, and the effect is weighed by the ratio between the angular-diameter distances from the deflecting potential to the source $f_K(w-w')$ and from the observer to the source $f_K(w)$. Thus, a lensing mass distribution close to the observer gives rise to a large deflection, while a lens near the source, $w' \approx w$, has very little effect. The factor of 2 is a relic from general relativity and is due to space-time curvature, which is missing in Newtonian gravity. Assuming $K=0$, we can replace $f_K(w)$ by w .

It is important to realize that the deflection itself is not observable. If all light rays emerging from a source were deflected by the same angle on their way to the observer, no noticeable effect remained. What is important, therefore, is not the deflection angle itself but its change from one light ray to the next. This is quantified by the derivative of the deflection angle with respect to the direction $\vec{\theta}$,

$$\frac{\partial \alpha_i}{\partial \theta_j} = \frac{2}{c^2} \int_0^w dw' \frac{(w-w')w'}{w} \frac{\partial^2 \Phi}{\partial x_i \partial x_j}(w' \vec{\theta}). \quad (214)$$

The additional factor w' in the weight function arises because the derivative of the potential is taken with respect to comoving coordinates x_i rather than the angular components θ_i . Obviously, the complete weight function

$$W(w', w) \equiv (w-w')w'/w \quad (215)$$

vanishes at the observer, $w'=0$, and at the source, $w'=w$, and peaks approximately half-way in between.

For applications of gravitational lensing, it is important to distinguish the trace-free part of matrix (214) from its trace,

$$\text{tr} \left(\frac{\partial \alpha_i}{\partial \theta_j} \right) = \frac{2}{c^2} \int_0^w dw' W(w', w) \left(\frac{\partial^2 \Phi}{\partial x_1^2} + \frac{\partial^2 \Phi}{\partial x_2^2} \right)(w' \vec{\theta}). \quad (216)$$

The derivatives of Φ can be combined to the two-dimensional Laplacian, which can be replaced by the three-dimensional Laplacian because the derivatives parallel to the line of sight do not contribute to integral (216). Thus, we find

$$\text{tr} \left(\frac{\partial \alpha_i}{\partial \theta_j} \right) = \frac{2}{c^2} \int_0^w dw' W(w', w) \Delta \Phi. \quad (217)$$

Next, we can use Poisson's equation to replace the Laplacian of Φ by the density. In fact, we have to take into account that light deflection is caused by density *perturbations* and that we need the Laplacian in terms of *comoving* rather than *physical* coordinates. Thus,

$$a^{-2}\Delta\Phi = 4\pi G\bar{\rho}\delta, \quad (218)$$

where δ is the density contrast and

$$\bar{\rho} = \bar{\rho}_0 a^{-3} = \rho_{\text{cr}} \Omega_{m0} a^{-3} = \frac{3H_0^2}{8\pi G} \Omega_{m0} a^{-3} \quad (219)$$

is the mean matter density. Thus, Poisson's equation reads

$$\Delta\Phi = \frac{3}{2}H_0^2\Omega_{m0}\delta/a, \quad (220)$$

and Eq. (217) becomes

$$\text{tr}\left(\frac{\partial\alpha_i}{\partial\theta_j}\right) = \frac{3H_0^2\Omega_{m0}}{c^2} \int_0^w dw' W(w', w) \frac{\delta}{a} \equiv 2\kappa, \quad (221)$$

where we have introduced the (effective) convergence κ .

The trace-free part of matrix (214) is

$$\frac{\partial\alpha_i}{\partial\theta_j} - \frac{1}{2}\delta_{ij} \text{tr}\left(\frac{\partial\alpha_i}{\partial\theta_j}\right) = \frac{\partial\alpha_i}{\partial\theta_j} - \delta_{ij}\kappa \equiv \begin{pmatrix} \gamma_1 & \gamma_2 \\ \gamma_2 & -\gamma_1 \end{pmatrix}, \quad (222)$$

which defines the so-called shear components γ_i . Specifically,

$$\gamma_1 = \frac{1}{c^2} \int_0^w dw' W(w', w) \left(\frac{\partial^2\Phi}{\partial x_1^2} - \frac{\partial^2\Phi}{\partial x_2^2} \right), \quad (223)$$

$$\gamma_2 = \frac{2}{c^2} \int_0^w dw' W(w', w) \left(\frac{\partial^2\Phi}{\partial x_1 \partial x_2} \right).$$

Combining results, we can write the matrix of deflection-angle derivatives as

$$\left(\frac{\partial\alpha_i}{\partial\theta_j} \right) = \begin{pmatrix} \kappa + \gamma_1 & \gamma_2 \\ \gamma_2 & \kappa - \gamma_1 \end{pmatrix}. \quad (224)$$

This matrix contains the important information on how an image is magnified and distorted. In the limit of weak gravitational lensing, the size of a lensed image is changed by the relative magnification

$$\delta\mu = 2\kappa, \quad (225)$$

while the image distortion is given by the shear components. In fact, an originally circular source with radius r will appear as an ellipse with major and minor axes,

$$a = r/(1 - \kappa - \gamma), \quad b = r/(1 - \kappa + \gamma), \quad (226)$$

where $\gamma \equiv (\gamma_1^2 + \gamma_2^2)^{1/2}$. The ellipticity of the observed image of a circular source thus provides an estimate for the shear,

$$\epsilon \equiv \frac{a-b}{a+b} = \frac{\gamma}{1-\kappa} \approx \gamma. \quad (227)$$

2. Power spectra

Of course, the exact light deflection expected along a particular line of sight cannot be predicted because the mass distribution along that light path is unknown. However, we can predict the *statistical properties* of weak lensing from those of the density-perturbation field. We

are thus led to the following problem: Suppose the power spectrum $P(k)$ of a Gaussian random density-perturbation field δ is known, what is the power spectrum of any weighed projection of δ along the line of sight? The answer is given by Limber's equation. Suppose the weight function is $q(w)$ and the projection is

$$g(\vec{\theta}) = \int_0^w dw' q(w') \delta(w' \vec{\theta}). \quad (228)$$

If $q(w)$ is smooth compared to δ , i.e., if the weight function changes on scales much larger than typical scales in the density contrast, then the power spectrum of g is

$$P_g(l) = \int_0^w dw' \frac{q^2(w')}{w'^2} P\left(\frac{l}{w'}\right), \quad (229)$$

where \vec{l} is a two-dimensional wave vector which is the Fourier conjugate variable to the two-dimensional position $\vec{\theta}$ on the sky.

Strictly speaking, Fourier transforms are inappropriate because the sky is not an infinite two-dimensional plane. Instead, the appropriate set of orthonormal base functions are the spherical harmonics. However, lensing effects are usually observed in areas whose solid angle is very small compared to the full sky. If this is so, the survey area can be approximated by a section of the plane locally tangent to the sky, and Fourier transforms can be used in this so-called flat-sky approximation.

Equation (221) is clearly of form (228) with the weight function

$$q(w') = \frac{3}{2}\Omega_{m0} \frac{H_0^2}{c^2} \frac{W(w', w)}{a}, \quad (230)$$

thus the power spectrum of the convergence is, according to Limber's equation,

$$P_\kappa(l) = \frac{9\Omega_{m0}^2 H_0^4}{4 c^4} \int_0^w dw' \bar{W}^2(w', w) P\left(\frac{l}{f_k(w')}\right), \quad (231)$$

with a new weight function

$$\bar{W}(w', w) \equiv W(w', w)/aw'. \quad (232)$$

While it requires huge data sets and careful data analysis to observe the differential magnification $\delta\mu$ or the convergence κ (Scranton *et al.*, 2005), image distortions can in principle be measured in a more straightforward way. With a brief excursion through Fourier space, it can easily be shown that the power spectrum of the shear is exactly identical to that of the convergence,

$$P_\gamma(l) = P_\kappa(l). \quad (233)$$

Thus, the statistics of the image distortions caused by cosmological weak lensing contains integral information on the power spectrum of the matter fluctuations.

Since the shear is defined on the two-spheres (the observer's sky), its power spectrum is related to its correlation function ξ_γ through the two-dimensional Fourier transform

$$\xi_\gamma(\phi) = \int \frac{d^2l}{(2\pi)^2} P_\gamma(l) e^{i\vec{\phi}\vec{l}} = \int_0^\infty \frac{ldl}{2\pi} P_\gamma(l) J_0(l\phi), \quad (234)$$

where J_ν is the ordinary Bessel function of order ν .

3. Correlation functions

In principle, shear correlation functions are measured by comparing the ellipticity of one galaxy with the ellipticity of other galaxies at an angular distance ϕ from the first. Ellipticities are oriented, of course, and one has to specify against what other direction the direction of, say, the major axis of a given ellipse is to be compared with. Since correlation functions are measured comparing the shear of galaxy pairs, a preferred direction is defined by the line connecting the two galaxies of the pair under consideration.

Let α be the angle between this direction and the major axis of the ellipse, then the tangential and cross components of the shear are defined by

$$\gamma_+ \equiv \gamma \cos 2\alpha, \quad \gamma_\times \equiv \gamma \sin 2\alpha. \quad (235)$$

The factor 2 is important because it accounts for the fact that an ellipse is mapped onto itself when rotated by an angle π . This illustrates that the shear is a spin-2 field: it returns into its original orientation when rotated by π rather than 2π .

The correlation functions of the tangential and cross components of the shear are

$$\begin{aligned} \xi_{++}(\phi) &= \langle \gamma_+(\theta) \gamma_+(\theta + \phi) \rangle \\ &= \frac{1}{2} \int_0^\infty \frac{ldl}{2\pi} P_\kappa(l) [J_0(l\phi) + J_4(l\phi)] \end{aligned} \quad (236)$$

and

$$\begin{aligned} \xi_{\times\times}(\phi) &= \langle \gamma_\times(\theta) \gamma_\times(\theta + \phi) \rangle \\ &= \frac{1}{2} \int_0^\infty \frac{ldl}{2\pi} P_\kappa(l) [J_0(l\phi) - J_4(l\phi)], \end{aligned} \quad (237)$$

while the cross correlation between the tangential and cross components must vanish, $\xi_{+\times}(\phi) = 0$. This suggests to define the correlation functions $\xi_\pm = \xi_{++} \pm \xi_{\times\times}$, which are related to the power spectrum through $\xi_\pm = \xi_\gamma$ and

$$\xi_- = \int_0^\infty \frac{ldl}{2\pi} P_\kappa(l) J_4(l\phi). \quad (238)$$

The principle of all measures for cosmic shear is the same: they are integrals of the weak-lensing power spectrum times filter functions describing the specific response of the measurement to the underlying power spectrum of density fluctuations. The width of the filter functions controls the range of density-perturbation modes \vec{k} contributing to one specific mode \vec{l} of weak lensing on the sky.

We can now estimate typical numbers for the cosmological weak-lensing effect. The power Δ_κ in the weak-

lensing quantities such as the cosmic shear is given by the power spectrum $P_\kappa(l)$ found in Eq. (231) times the volume in l space,

$$\Delta_\kappa(l) \approx l^2 P_\kappa(l). \quad (239)$$

Assuming a cosmological model with $\Omega_{m0}=0.3$ and $\Omega_{\Lambda 0}=0.7$, the CDM power spectrum and a reasonable source redshift distribution $\Delta_\kappa^{1/2}(l)$ are found to peak on scales l corresponding to angular scales $2\pi/l$ of $2'-3'$, and the peak reaches values of 0.04–0.05. This shows that cosmological weak lensing will typically cause source ellipticities of a few percent, and correlations have a typical angular scale of a few arcminutes. Details depend on the measure chosen through the filter function.

B. Cosmic-shear measurements

1. Typical scales and requirements

How can cosmic gravitational-lensing effects be measured? As shown in Eq. (227), the ellipticity of a hypothetical circular source is an *unbiased estimator* for the shear. However, typical sources are not circular but to first approximation elliptical themselves. Thus, measuring their ellipticities yields their intrinsic ellipticities in the first place.

Let $\epsilon^{(s)}$ be the intrinsic source ellipticity. It is a two-component spin-2 quantity. The cosmic shear adds to that ellipticity, such that the observed ellipticity is

$$\epsilon \approx \epsilon^{(s)} + \gamma \quad (240)$$

in the weak-lensing approximation. What is observed is therefore the sum of the signal γ and the intrinsic noise component $\epsilon^{(s)}$.

On sufficiently deep observations, $\lesssim 20$ galaxies/arc min² are routinely detected. Since the full moon has half a degree diameter, it covers a solid angle of $15^2\pi = 700$ arc min² or $\lesssim 14\,000$ of such distant faint galaxies. From this point of view, the sky is covered by densely patterned “wallpaper” of distant galaxies. Thus, it is possible to average observed galaxy ellipticities. Assuming their shapes are intrinsically independent, the intrinsic ellipticities will average out, and the shear will remain,

$$\langle \epsilon \rangle \approx \langle \epsilon^{(s)} \rangle + \langle \gamma \rangle \approx \langle \gamma \rangle. \quad (241)$$

It is a fortunate coincidence that the typical angular scale of cosmic lensing, which we found to be of order a few arcminutes, is large compared to the mean distance between background galaxies, which is of order $\sqrt{1/20} \approx 0.2'$. This enables averages over background galaxies without canceling the cosmic-shear signal. If γ varied on scales comparable to or smaller than the mean galaxy separation, any average over galaxies would remove the lensing signal as well.

The intrinsic ellipticities of the faint background galaxies have a distribution with a standard deviation of $\sigma_\epsilon \approx 0.3$. Averaging over N of them, and assuming Poisson statistics, yields expectation values of

$$\langle \epsilon^{(s)} \rangle = 0, \quad \delta\epsilon = \langle (\epsilon^{(s)})^2 \rangle^{1/2} = \sigma_\epsilon / \sqrt{N} \quad (242)$$

for the mean and its intrinsic fluctuation.

A rough estimate for the signal-to-noise ratio of a cosmic-shear measurement can proceed as follows. Suppose the correlation function ξ is measured by counting pairs of galaxies with a separation within $\delta\theta$ of θ . As long as θ is small compared to the side length of the survey area A , the number of pairs will be

$$N_p = \frac{1}{2} n^2 A 2\pi\theta\delta\theta, \quad (243)$$

and thus the Poisson noise due to the intrinsic ellipticities will be

$$\text{noise} \approx 2\sigma_\epsilon n \sqrt{\pi A \theta \delta\theta}, \quad (244)$$

where the factor of 2 arises because of the two galaxies involved in each pair. The signal is the square root of the correlation function ξ given by

$$\xi \approx l^2 P_\kappa(l) \delta \ln l \approx l^2 P_\kappa(l) \frac{\delta l}{l} \approx l^2 P_\kappa(l) \frac{\delta\theta}{\theta}, \quad (245)$$

where we have used in the last step that $\theta = 2\pi/l$. Thus, the signal-to-noise ratio is estimated to be

$$\frac{S}{N} \approx \frac{\sqrt{\xi}}{\text{noise}} \approx \frac{\ln \delta\theta \sqrt{\pi A P_\kappa}}{2\sigma_\epsilon} = \frac{n \sqrt{\pi^3 A P_\kappa} \delta\theta}{\sigma_\epsilon \theta}. \quad (246)$$

Evidently, the signal-to-noise ratio, and thus the significance of any cosmic-lensing detection, grows with the survey area and decreases with the intrinsic ellipticity of the source galaxies. In evaluating Eq. (246) numerically, we have to take into account that $l^2 P_\kappa(l)$ must be a dimensionless number, which implies that the power spectrum P_κ must have the dimension steradian. Therefore, either the survey area A and the number density n in Eq. (246) must be converted to steradians or P_κ must be converted to square arcminutes first.

The signal-to-noise ratio increases approximately linearly with scale. Assuming $\delta\theta/\theta = 0.1$, it is $S/N \approx 5$ on a scale of $0.5'$ for a survey of 1 sq deg area. This shows that, if the cosmic shear should be measured on such small scales with an accuracy of, say, 5%, a survey area of $A \approx (20/5)^2 \approx 16$ sq deg is needed since the signal-to-noise ratio scales like the square root of the survey area. On such an area, the ellipticities of $16 \times 3600 \times 30 \approx 2 \times 10^6$ background galaxies have to be accurately measured.

Matters are more complicated in reality, but the orders of magnitude are well represented by this rough estimate. Bearing in mind that typical fields of view of telescopes large enough for detecting sufficiently many faint background galaxies reach one-tenth of 1 sq deg up to 1 sq deg and that typical exposure times are of order 1 h for that purpose, the total amount of telescope time for a weak-lensing survey of about 100 sq deg is estimated to be several hundred telescope hours. With perhaps 5 h of telescope time per night and perhaps half of the nights per year usable, it is easy to see that the time needed for such surveys is measured in months.

Since typical sizes of the faint background galaxies measure fractions of arcseconds, shape measurements require a pixel resolution of, say, $0.1''$. A total survey area of 100 sq deg must therefore be resolved into $100 \times 3600 \times 3600 / 0.1^2 \approx 1.3 \times 10^{11}$ pixels.

These estimates neglect all sources of noise other than the shot noise caused by the finite number of galaxies. On angular scales below a few arcminutes, the cosmic variance caused by field-to-field variations in the shear signal due to the large-scale cosmic structures must be added (Kilbinger and Schneider, 2004).

2. Ellipticity measurements

The determination of image ellipticities is straightforward in principle but difficult in practice (Kaiser *et al.*, 1995). Often, the surface-brightness quadrupole

$$Q_{ij} = \frac{\int I(\vec{x}) x_i x_j d^2x}{\int I(\vec{x}) d^2x} \quad (247)$$

is measured, from whose principal axes the ellipticity can be read off. Real galaxy images, however, are typically far from ideally elliptical. They are structured or otherwise irregular. In addition, if they are small, they are coarsely resolved into just a few pixels, so that only a crude approximation to the integral in Eq. (247) can be found.

How the image of a pointlike source, such as a star, appears on the detector is described by the point-spread function (PSF). The PSF may be anisotropic if the telescope optics is slightly astigmatic, and this anisotropy may, and will in general, depend on the location in the focal plane. The image is a convolution of the ideal image shape prior to any distortion by the atmosphere and the telescope optics. Any accurate measurement of image ellipticities requires a PSF correction or deconvolution, for which the PSF must of course be known. It is commonly measured off the images of stars in the field.

Many other effects may distort the PSF and thus the images in systematic ways. For instance, if the CCD chips are not exactly perpendicular to the optical axis of the telescope, if the individual chips of a CCD mosaic are not exactly coplanar, or if the telescope is slightly out of focus, systematic image deformations may result which typically vary across the focal plane. They have to be measured and corrected. This is commonly achieved by fitting the measured PSF by low-order two-dimensional polynomials on the focal plane. Since part of the image distortions may depend on time due to thermal deformation, changing atmospheric conditions and such, PSF corrections will also depend on time and have to be determined and applied with much care.

Even if the surface-brightness quadrupole of the image on the detector can be accurately determined, the image appears affected by imperfections of the telescope optics and by the turbulence in the atmosphere, the so-called *seeing*. Due to the wave nature of light and the

finite size of the telescope mirror, the telescope will have finite resolution. The angular resolution limit is given by Eq. (186). With $\lambda \approx 6 \times 10^{-5}$ cm and $D = 400$ cm, the angular resolution is $\Delta\theta \approx 0.04''$, much smaller than needed for our purposes.

The turbulence of the Earth's atmosphere effectively convolves images with a Gaussian whose width depends on the site, the weather, and other conditions. Typical seeing ranges around $1''$. Under very good conditions, it can shrink to $\sim 0.5''$ or even less. Clearly, if an image of subarcsecond size is convolved with a Gaussian of similar width, any ellipticity is substantially reduced.

Systematic effects may remain which need to be detected and quantified. Any coherent image distortions caused by gravitational lensing must be describable by the tidal gravitational field, i.e., by second-order derivatives of a scalar potential. In analogy to the \vec{E} field in electromagnetism, such distortion patterns are called E modes. Similarly, distortion patterns which are described as the curl of a vector field are called B modes. They cannot be due to gravitational lensing and thus signal systematic effects remaining in the data. Such B -mode contaminations could recently be strongly reduced or suppressed by improved algorithms for PSF correction (Hoekstra, 2004). Absence of B -mode contamination does not allow the implication that the results are free of systematics, though, because optical distortions also tend to create spurious E modes.

3. Results

Despite the smallness of the effect and the many difficulties in measuring it, much progress in cosmic-shear observations has been achieved in the past few years (Heymans *et al.*, 2006; Massey *et al.*, 2007a). Current and ongoing surveys, in particular the Canada-France-Hawaii Legacy Survey (CFHLS) (Semboloni *et al.*, 2006; Fu *et al.*, 2008), combined with well-developed largely automatic data-analysis pipelines, have succeeded in producing cosmic-shear correlation functions with very small error bars covering angular scales from below an arcminute to several degrees. The best correlation functions could be shown to be at most negligibly contaminated by B modes.

The power spectrum $P_\kappa(l)$ depends crucially on the nonlinear evolution of the dark-matter power spectrum. This and the exact redshift distribution of the background galaxies are the major uncertainties now remaining in the interpretation of cosmic-shear surveys. Apart from that, the measured cosmic-shear correlation functions agree very well with the theoretical expectation from CDM density fluctuations in a spatially flat low-density universe.

As Eq. (231) shows, the weak-lensing power spectrum $P_\kappa(l)$ depends on the product of a factor Ω_{m0}^2 due to the Poisson equation times the amplitude A of the matter power spectrum. An additional weak dependence on cosmological parameters is caused by the geometric weight function $\bar{W}(w', w)$. The cosmic-shear correlation

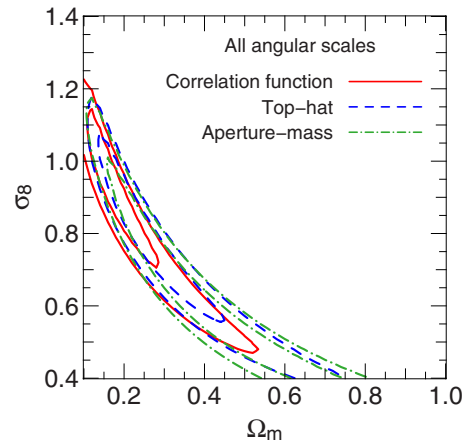


FIG. 10. (Color online) Constraints in the Ω_{m0} - σ_8 plane from weak lensing on large angular scales in the CFHTLS. The Universe is assumed spatially flat here. From Fu *et al.*, 2008.

function thus measures approximately the product $A\Omega_{m0}^{2\alpha}$, $\alpha \lesssim 1$, which means that the amplitude of the power spectrum is nearly degenerate with the matter density parameter. Only if it is possible to constrain Ω_{m0} or A in any other way can the degeneracy be broken.

We see later how this may work. The amplitude of the power spectrum A is conventionally described by a parameter σ_8^2 which will be described in Sec. X. Weak lensing thus constrains the product $\sigma_8\Omega_{m0}^\alpha$, and latest measurements find $\sigma_8(\Omega_{m0}/0.25)^{0.64} \approx 0.784 \pm 0.043$ (Fu *et al.*, 2008) (see Fig. 10).

Weak gravitational lensing is a fairly new field of cosmological research. Within a few years, it has considerably matured and returned cosmologically interesting constraints. Considerable potential is attributed to weak lensing in wide-area surveys in particular when combined with photometric redshift information because this is expected to allow constraints on the growth of cosmic structures.

IX. SUPERNOVAE OF TYPE Ia

A. Standard candles and distances

1. The principle

Before discussing supernovae of type Ia and their cosmological relevance, we set the stage with a few illustrative considerations. Suppose we had a standard candle whose luminosity L we knew precisely. Then, according to the definition of the luminosity distance in Eq. (20), the distance can be inferred from the measured flux S through

$$D_{\text{lum}} = \sqrt{L/4\pi S}. \quad (248)$$

Besides the redshift z , the luminosity distance will depend on the cosmological parameters,

$$D_{\text{lum}} = D_{\text{lum}}(z; \Omega_{m0}, \Omega_{\Lambda0}, H_0, \dots), \quad (249)$$

which can in principle be used to determine cosmological parameters from a set of distance measurements from a class of standard candles.

For this to work, the standard candles must be at a suitably high redshift for the luminosity distance to depend on the cosmological model. As seen in Eq. (21), all distance measures share the low- z limit

$$D \approx cz/H_0 \quad (250)$$

and lose their sensitivity to all cosmological parameters except H_0 .

In reality, we rarely know the absolute luminosity L even of cosmological standard candles. The problem is that they need to be calibrated first, which is only possible from a flux measurement once the distance is known by other means, such as from parallaxes in case of the Cepheids. Supernovae, however, which are the subject of this section, are typically found at distances which are way too large to allow direct distance measurements. Therefore, the only way out is to combine distant supernovae with local ones, for which the approximate distance relation (250) holds.

Any measurement of flux S_i and redshift z_i of the i th standard candle in a sample then yields an estimate for the luminosity L in terms of the squared inverse Hubble constant,

$$L = 4\pi S_i (cz_i/H_0)^2. \quad (251)$$

Since all cosmological distance measures are proportional to the Hubble length c/H_0 , the dependence on H_0 on both sides of Eq. (248) cancels, and the determination of cosmological parameters other than the Hubble constant becomes possible. Thus, the first lesson to learn is that cosmology from distant supernovae requires a sample of nearby supernovae for calibration.

Of course, this nearby sample must satisfy the same criterion as the distance indicators used for the determination of the Hubble constant: their redshifts must be high enough for the peculiar velocities to be negligible, thus $z \gtrsim 0.02$. If the redshifts are low enough for the linear approximation (250) to hold, the interpretation of the nearby sample is independent of the cosmological model.

It is important to note that it is not necessary to know the absolute luminosity L even up to the uncertainty in H_0 . If L is truly independent of redshift, cosmological parameters could still be determined through Eq. (248) from the *shape* of the measured relation between flux and redshift even though its precise *amplitude* may be unknown. It is only important that the objects used are standard candles, but not how *bright* they are.

2. Requirements and degeneracies

We now collect several facts about cosmological inference from standard candles. Since we aim at the determination of cosmological parameters, say Ω_{m0} , it is important to estimate the accuracy that we can achieve

from measurements of the luminosity distance. Suppose we restrict the attention to spatially flat cosmological models, for which $\Omega_{\Lambda0} = 1 - \Omega_{m0}$. Then, because the dependence on the Hubble constant was canceled, Ω_{m0} is the only remaining relevant parameter. We estimate the accuracy through first-order Taylor expansion,

$$\Delta D_{\text{lum}} \approx \frac{dD_{\text{lum}}}{d\Omega_{m0}} \Delta\Omega_{m0}, \quad (252)$$

about a fiducial model, such as a Λ CDM model with $\Omega_{m0} = 0.3$.

At a fiducial redshift of $z \approx 0.8$, we find numerically

$$d \ln D_{\text{lum}} / d\Omega_{m0} \approx -0.5, \quad (253)$$

which shows that a *relative* distance accuracy of

$$\Delta D_{\text{lum}} / D_{\text{lum}} \approx -0.5 \Delta\Omega_{m0} \quad (254)$$

is required to achieve an absolute accuracy of $\Delta\Omega_{m0}$. For $\Delta\Omega_{m0} \approx 0.02$, say, distances thus need to be known to $\approx 1\%$.

This accuracy requires sufficiently large supernova samples. Assuming Poisson statistics for simplicity and distance measurements to N supernovae, the combined accuracy is

$$|\Delta\Omega_{m0}| \approx \frac{2}{\sqrt{N}} \frac{\Delta D_{\text{lum}}}{D_{\text{lum}}}. \quad (255)$$

That is, an accuracy of $\Delta\Omega_{m0} \approx 0.02$ can be achieved from ≈ 100 supernovae whose individual distances are known to $\approx 10\%$.

Anticipating physical properties of type-Ia supernovae, their intrinsic peak luminosities in blue light are $L \approx 3.3 \times 10^{43} \text{ erg s}^{-1}$, with a relative scatter of order 10% .³ Given uncertainties ΔL in the luminosity L and ΔS in the flux measurement S , error propagation on Eq. (248) yields the relative distance uncertainty

$$\frac{\Delta D_{\text{lum}}}{D_{\text{lum}}} = \frac{1}{2} \left[\left(\frac{\Delta L}{L} \right)^2 + \left(\frac{\Delta S}{S} \right)^2 \right]^{1/2}. \quad (256)$$

Even if the flux could be measured precisely, the intrinsic luminosity scatter currently forbids distance determinations to better than 10% .

Fluxes have to be inferred from photon counts. For various reasons to be clarified later, supernova light curves should be determined until ~ 35 days after the peak when the luminosity has typically dropped to $\approx 2.5 \times 10^{42} \text{ erg s}^{-1}$. The luminosity distance to $z \approx 0.8$ is $\approx 5 \text{ Gpc}$, which implies fluxes $S \approx 1.1 \times 10^{-14} \text{ erg s}^{-1} \text{ cm}^{-2}$ at peak and $S \approx 8.7 \times 10^{-16} \text{ erg s}^{-1} \text{ cm}^{-2}$ 35 days later.

Dividing by an average photon energy of $5 \times 10^{-12} \text{ erg}$, multiplying with the area of a typical telescope mirror with 4 m diameter, and assuming a total

³As we see later, type-Ia supernovae are *standardizable* rather than standard candles, and the standardizing procedure is currently not able to reduce the scatter further.

quantum efficiency of 30%, we find detected photon fluxes of $S_\gamma \approx 85 \text{ s}^{-1}$ at peak and $S_\gamma \approx 7 \text{ s}^{-1}$ 35 days afterwards. These fluxes are typically distributed over a few CCD pixels.

Supernovae need to be identified against the background of their host galaxies and the sky brightness. For distant supernovae, the sky brightness on the area of the supernova image is typically 10–1000 times higher than the supernova itself, dominating the noise budget. Let N_{SN} and N_{sky} the numbers of photons received from the supernova and the sky, respectively, on the supernovae image, and assume for simplicity $N_{\text{sky}} \approx 100N_{\text{SN}}$. Then, an estimate for the signal-to-noise ratio for the detection is

$$\frac{S}{N} \approx \frac{N_{\text{SN}}}{\sqrt{N_{\text{SN}} + N_{\text{sky}}}} \approx \frac{N_{\text{SN}}}{\sqrt{100N_{\text{SN}}}} \approx \frac{\sqrt{N_{\text{SN}}}}{10}. \quad (257)$$

Signal-to-noise ratios of ≥ 10 –35 days after the maximum thus require $N_{\text{SN}} \approx 10^4$ photons from the supernova. This implies exposure times of order $10^4/7 \approx 1400 \text{ s}$ or about 20 min. Typical exposure times are thus of order 15–30 min to capture supernovae out to redshifts $z \sim 1$. Then, the photometric error around peak luminosity is certainly less than the remaining scatter in the intrinsic luminosity, and relative distance accuracies of order 10% are within reach.

However, a major difficulty is the fact that the identification of type-Ia supernovae requires spectroscopy. Sufficiently accurate spectra typically require exposures lasting 1–3 h/spectrum on the world’s largest telescopes, such as European Southern Observatory’s (ESO’s) Very Large Telescope which consists of four individual mirrors with 8 m diameter each.

In order to see what we can hope to constrain by measuring luminosity distances, we form the gradient of D_{lum} in the Ω_{m0} - $\Omega_{\Lambda0}$ plane,

$$\vec{g} \equiv (\partial D_{\text{lum}}/\partial \Omega_{m0}, \partial D_{\text{lum}}/\partial \Omega_{\Lambda0})^T, \quad (258)$$

at a fiducial Λ CDM model with $\Omega_{m0}=0.3$. When normalized to unit length, it turns out to point into the direction

$$\vec{g} = \begin{pmatrix} -0.76 \\ 0.65 \end{pmatrix}. \quad (259)$$

This vector rotated by 90° then points into the direction in the Ω_{m0} - $\Omega_{\Lambda0}$ plane along which the luminosity distance does not change. Thus, near the fiducial Λ CDM model, the parameter combination

$$P \equiv \vec{g} \cdot \begin{pmatrix} \Omega_{m0} \\ \Omega_{\Lambda0} \end{pmatrix} = -0.76\Omega_{m0} + 0.65\Omega_{\Lambda0} \quad (260)$$

is degenerate. The degeneracy direction, characterized by the vector $\mathcal{R}(\pi/2)\vec{g}=(0.65, 0.76)^T$, encloses an angle of $\arctan(0.76/0.65)=49.5^\circ$ with the Ω_{m0} axis almost along the diagonal from the lower left to the upper right corner of the parameter plane. Thus, it is almost perpendicular to the degeneracy direction obtained from the curvature constraint due to the CMB. This illustrates how parameter degeneracies can efficiently be broken

by combining suitably different types of measurement. Moreover, combining supernova data from a wide redshift range partially lifts the parameter degeneracy obtained from them already.

B. Supernovae

1. Types and classification

Supernovae are “eruptively variable” stars. A sudden rise in brightness is followed by a gentle decline. They are unique events which at peak brightness reach luminosities comparable to those of an entire galaxy or $(10^{10}–10^{11})L_\odot$. They reach their maxima within days and fade within several months.

Supernovae are traditionally characterized by their early spectra (Filippenko, 1997). If hydrogen lines are missing, they are of type I, otherwise of type II. Type-Ia supernovae show silicon lines, unlike type-Ib/c supernovae, which are distinguished by the prominence of helium lines. Normal type-II supernovae have spectra dominated by hydrogen. They are subdivided according to their light-curve shape into type IIL and type IIP. Type-IIB supernova spectra are dominated by helium instead.

Except for type Ia, supernovae arise due to the collapse of a massive stellar core, followed by a thermonuclear explosion which disrupts the star by driving a shock wave through it. Core-collapse supernovae of type II arise from stars with masses between $8M_\odot$ and $30M_\odot$, those of type I (i.e., types Ib/c) from more massive stars (Woosley *et al.*, 2002).

Type-Ia supernovae, which we are dealing with here, arise when a white dwarf is driven toward the Chandrasekhar mass limit by mass overflowing from a companion star. In a binary system, the more massive star evolves faster and can reach its white-dwarf stage before its companion leaves the main sequence and becomes a red giant. When this happens, and the stars are close enough, matter will flow from the expanding red giant on the white dwarf.

Electron degeneracy pressure can stabilize white dwarfs up to the Chandrasekhar mass limit of $\sim 1.4M_\odot$ (Chandrasekhar, 1984; Hillebrandt and Niemeyer, 2000). Because the core material is degenerate, its pressure is independent of its temperature. The mass accreted from the companion star increases the pressure until nuclear burning can begin in isolated places somewhere in the core. The electron degeneracy is lifted, the temperature rises dramatically, and the thermonuclear runaway sets in. Neutrinos produced in inverse beta decays carry away much of the explosion energy unnoticed because they can leave the supernova essentially without further interaction.

This thermonuclear runaway destroys the white dwarf. Since this type of explosion (more precisely, deflagration) involves an approximately fixed amount of mass, it is physically plausible that the explosion releases a fixed amount of energy. Thus, the Chandrasekhar mass

limit is the main responsible for type-Ia supernovae to be approximate standard candles.

The nuclear fusion processes in type-Ia supernovae convert the carbon and oxygen in the core of the white dwarf into ^{56}Ni , which later decays through ^{56}Co into stable ^{56}Fe . According to detailed numerical explosion models, the nuclear fusion is started at random points near the center of the white dwarf (Röpke *et al.*, 2007).

The presence of silicon lines in the type-Ia spectra indicates that not all of the white dwarf's material is converted into ^{56}Ni . This shows that there is no explosion, but a deflagration, in which the flame front propagates at velocities below the sound speed. The deflagration can burn the material fast enough if it is turbulent because the turbulence dramatically increases the surface of the flame front and thus the amount of material burnt per unit time. Theoretical models predict that $\sim 0.5M_{\odot}$ of ^{56}Ni is typically produced.

The peak brightness is reached when the deflagration front reaches the former white dwarf's surface and drives it as a rapidly expanding envelope into the surrounding space. The γ photons released in the nuclear fusion processes are redshifted by scattering off the expanding material and finally leave the explosion site as x-ray, UV, optical, and infrared photons.

Once the thermonuclear fusion has ended, additional energy is released by the β decay of ^{56}Co into ^{56}Fe with a half-life of 77.12 days. The exponential nature of the radioactive decay causes the typical exponential decline phase in supernova light curves (Truran *et al.*, 1967; Colgate and McKee, 1969). Since the supernova light has to propagate through the expanding envelope before we can see it, the opacity of the envelope and thus its metallicity are important for the appearance of the supernova (Blinnikov *et al.*, 2006).

2. Observations

Since supernovae are transient phenomena, they can only be detected by sufficiently frequent monitoring of selected areas in the sky. Typically, fields are selected by their accessibility for the telescope to be used and the least degree of absorption by the Galaxy. Since a type-Ia supernova event lasts for about a month, monitoring is required every few days.

Supernovae are then detected by differential photometry, in which the average of all preceding images is subtracted from the last image taken. Since the seeing varies, the images appear convolved with point-spread functions of variable width even if they are taken with identical optics; thus the objects on them appear more or less blurred. Before they can be meaningfully subtracted, they therefore have to be convolved with the same effective point-spread function. This causes several complications in the later analysis procedure, in particular with the photometry.

Of course, this detection procedure returns many variable stars and supernovae of other types, which are not standard candles and have to be removed from the sample. Preselection of type-Ia candidates is done by

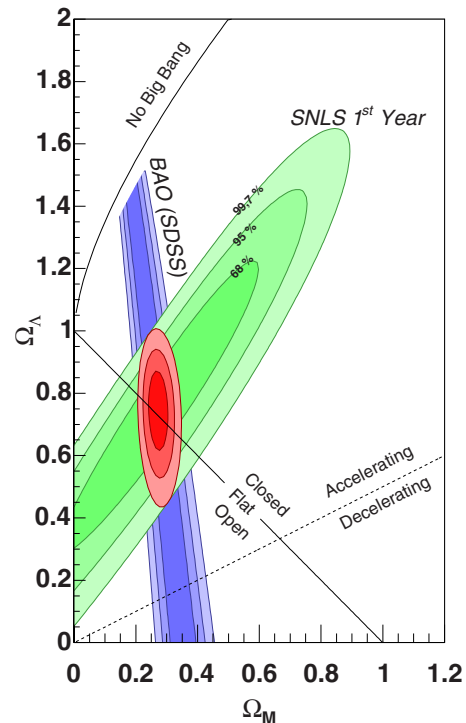


FIG. 11. (Color online) Constraints in the Ω_{m0} - $\Omega_{\Lambda 0}$ plane obtained from type-Ia supernovae in the SNLS. From Astier *et al.*, 2006.

color and the light-curve shape, but the identification of type-Ia supernovae requires spectroscopy in order to identify the decisive silicon lines at 6347 and 6371 Å. Since these lines move out of the optical spectrum at redshifts $z \geq 0.5$, near-infrared observations are crucially important for the high-redshift supernovae relevant for cosmology (see Fig. 11).

Nearby supernovae, which are needed for calibration, reveal that type-Ia supernovae are not standard candles but show a substantial scatter in luminosity. It turned out that there is an empirical relation between the duration of the supernova event and its peak brightness in that brighter supernovae last longer (Phillips *et al.*, 1999). This relation between the light-curve shape and the brightness can be used to standardize type-Ia supernovae. It was seen as a major problem for their cosmological interpretation that the origin for this relation was unknown and that its application to high-redshift supernovae was based on the untested assumption that the relation found and calibrated with local supernovae would also hold there. Recent simulations indicate that the relation is an opacity effect (Kasen and Woosley, 2007): brighter supernovae produce more ^{56}Ni and thus have a higher metallicity, which causes the envelope to be more opaque, the energy transport through it to be slower, and therefore the supernova to last longer.

Thus, before a type-Ia supernova can be used as a standard candle, its duration must be determined, which requires the light curve to be observed over sufficiently long time. It must be taken into account here that the cosmic expansion leads to a time dilation, due to which

supernovae at redshift z appear longer by a factor of $1+z$. We note in passing that the confirmation of this time dilation effect indirectly supports the cosmic expansion. After the standardization, the scatter in the peak brightnesses of nearby supernovae is substantially reduced. This encourages (and justifies) their use as standardizable candles for cosmology.

The remaining relative uncertainty is now typically between 10% and 15% for individual supernovae. Since, as seen following Eq. (254), we require relative distance uncertainties at the percent level, of order a hundred distant, supernovae are needed before meaningful cosmological constraints can be placed, which justifies the remark after Eq. (255).

An example for the several currently ongoing supernova surveys is the Supernova Legacy Survey (SNLS) (Astier *et al.*, 2006) in the framework of the CFHLS, which is carried out with the 4-m Canada-France-Hawaii telescope on Mauna Kea. It monitors four fields of 1 sq deg each five times during the 18 days of dark time between two full moons (lunations).

Differential photometry is performed to find out variables, and candidate type-Ia supernovae are selected by light-curve fitting after removing known variable stars. Spectroscopy on the largest telescopes (mostly ESO's Very Large Telescope, but also the Keck and Gemini telescopes) is then needed to identify type-Ia supernovae. To give a few characteristic numbers, the SNLS has taken 142 spectra of type-Ia candidates during its first year of operation, of which 91 were identified as type-Ia supernovae.

The light curves of these objects are observed in several different filter bands. This is important to correct for interstellar absorption. Any dimming by intervening material makes supernovae appear fainter and thus more distant and will bias the cosmological results toward faster expansion. Since the intrinsic colors of type-Ia supernovae are characteristic, any deviation of the observed from the intrinsic colors signals interstellar absorption which is corrected by adapting the amount of absorption such that the observed is transformed back into the intrinsic color.

This correction procedure is expected to work well unless there is material on the way which absorbs equally at all wavelengths, so-called "gray dust" (Aguirre, 1999). This could happen if the absorbing dust grains are large compared to the wavelength. Currently, it is quite difficult to conclusively rule out gray dust, although it is implausible based on the interstellar absorption observed in the Galaxy (Riess *et al.*, 2004; Östman and Mörtzell, 2005).

After applying the corrections for absorption and duration, each supernova yields an estimate for the luminosity distance to its redshift. Together, the supernovae in the observed sample constrain the evolution of the luminosity distance with redshift, which is then fit varying the cosmological parameters except for H_0 , i.e., typically Ω_{m0} and $\Omega_{\Lambda0}$. This yields an "allowed" region in the Ω_{m0} - $\Omega_{\Lambda0}$ plane compatible with the measurements which is degenerate in the direction calculated before.

More information or further assumptions are necessary to break the degeneracy. The most common assumption, justified by the CMB measurements, is that the Universe is spatially flat. Based on it, the SNLS data yield a matter-density parameter of

$$\Omega_{m0} = 0.263 \pm 0.037. \quad (261)$$

This is a remarkable result. First, this result confirms the other independent measurements already discussed, which were based on kinematics, cluster evolution, and the CMB. Second, it shows that, in the assumed spatially flat universe, the dominant contribution to the total energy density must come from something else than matter, possibly the cosmological constant.

It is important for later discussion to realize in what way the parameter constraints from supernovae differ from those from the CMB. The fluctuations in the latter show that the Universe is at least nearly spatially flat, and the density parameters in dark and baryonic matter are near 0.24 and 0.04, respectively. The rest must be the cosmological constant or the dark energy. Arising early in the cosmic history, the CMB itself is almost insensitive to the cosmological constant, and thus it can only constrain it indirectly.

Type-Ia supernovae, however, measure the angular-diameter distance during the late cosmic evolution when the cosmological constant is much more important. As Eq. (260) shows, the luminosity distance constrains the difference between the two parameters,

$$\Omega_{\Lambda0} = 1.17\Omega_{m0} + P, \quad (262)$$

where the degenerate parameter P is determined by the measurement. Assuming $\Omega_{\Lambda0} = 1 - \Omega_{m0}$ as in a spatially flat universe yields

$$P = (1 - 2.17)\Omega_{m0} \approx 0.43 \quad (263)$$

from the SNLS first-year result [Eq. (261)], illustrating that the survey has constrained the density parameters to follow

$$\Omega_{\Lambda0} \approx 1.17\Omega_{m0} + 0.43. \quad (264)$$

The relative *acceleration* of the Universe \ddot{a}/a is given by Eq. (7), which can be simplified to read

$$\frac{\ddot{a}}{a} = H_0^2 \left(\Omega_{\Lambda0} - \frac{\Omega_{m0}}{2a^3} \right) \quad (265)$$

if matter is pressureless. Thus, the expansion of the Universe accelerates today ($a=1$) if $\ddot{a} = H_0^2(\Omega_{\Lambda0} - \Omega_{m0}/2) > 0$ or $\Omega_{\Lambda0} > \Omega_{m0}/2$. Given measurement (264), the conclusion seems inevitable that the Universe's expansion does indeed accelerate today (Riess *et al.*, 1998; Perlmutter *et al.*, 1999; Leibundgut and Blondin, 2005; Astier *et al.*, 2006).

If the Universe is indeed spatially flat, then the transition between decelerated and accelerated expansion happened at

$$1 - 0.263 \approx 0.263/2a^3 \Rightarrow a = 0.56 \quad (266)$$

or at redshift $z \approx 0.78$. Luminosity distances to supernovae at higher redshifts should show this transition, and in fact they do (Riess *et al.*, 2004).

3. Potential problems

The problem with possible gray dust has already been mentioned: While the typical colors of type-Ia supernovae allow the detection and correction of the reddening coming with typical interstellar absorption, gray dust would leave no trace in the colors and remain undetectable. However, gray dust would re-emit the absorbed radiation in the infrared and add to the infrared background, which is quite well constrained. It thus seems that gray dust is not an important contaminant if it exists.

Gravitational lensing is inevitable for distant supernovae (Holz and Wald, 1998). Depending on the line of sight, they are either magnified or demagnified. Since high magnifications due to nonlinear structures may occasionally happen, the magnification distribution must be skewed toward demagnification to keep the mean of unit magnification. Thus, the most probable magnification experienced by supernova is below unity. In other words, lensing may lead to a slight demagnification if lines of sight toward type-Ia supernovae are random with respect to the matter distribution. In any case, the rms cosmic magnification adds to the intrinsic scatter of the supernova luminosities. It may become significant for redshifts $z \gtrsim 1$.

It is a difficult and debated question whether supernovae at high redshifts are intrinsically the same as at low redshifts where they are calibrated. Should there be undetected systematic differences, cosmological inferences could be wrong. In particular, it may be natural to assume that metallicities at high redshifts are lower than at low redshifts. Since supernovae last longer if their atmospheres are more opaque, lower metallicity may imply shorter supernova events, leading to underestimated luminosities and overestimated distances. Simulations of type-Ia supernovae, however, seem to show that such an effect is probably not significant. For this and other systematic effects, see Leibundgut (2001).

It was also speculated that distant supernovae may be intrinsically bluer than nearby ones due to their possibly lower metallicity. Should this be so, the extinction correction, which is derived from reddening, would be underestimated, causing intrinsic luminosities to be underestimated and luminosity distances to be overestimated. Thus, this effect would lead to an *underestimate* of the expansion rate and counteract the cosmological constant. There is currently no indication of such a color effect.

Supernovae of types Ib/c may be mistaken for those of type Ia if the identification of the characteristic silicon lines fails for some reason. Since they are typically fainter than type-Ia supernovae, they would contaminate the sample and bias results toward higher luminosity distances and thus toward a higher cosmological con-

stant. It seems, however, that the possible contamination by non-type-Ia supernovae is so small that it has no noticeable effect.

Several more potential problems exist. It has been argued for a while that, if the evidence for a cosmological constant was based exclusively on type-Ia supernovae, it would probably not be considered entirely convincing. However, since the supernova observations come to conclusions compatible with virtually all independent cosmological measurements, they add substantially to the persuasiveness of the cosmological standard model. Moreover, recent supernova simulations reveal good physical reasons why they should in fact be reliable standardizable candles.

X. THE NORMALIZATION OF THE POWER SPECTRUM

A. Introduction

We saw in Sec. VII.B that the measured power spectrum of the galaxy distribution follows the CDM expectation in the range of wave numbers where current large surveys allow its measurement. This range can be extended to some degree toward smaller scales by measuring the autocorrelation of hydrogen absorption lines in the spectra of distant quasars. Such observations of the power spectrum of the so-called Lyman- α forest lines show that the power spectrum does indeed turn toward the asymptotic behavior $\propto k^{-3}$ (McDonald *et al.*, 2005; Viel *et al.*, 2008). In addition, we have seen that the peak location agrees with the expectation for a universe with $\Omega_{m0} \approx 0.3$ and $h \approx 0.72$. This indicates that the CDM expectation for the dark-matter power spectrum is indeed at least very close to its real shape, which is a remarkable finding.

Although the shape of the power spectrum could thus be quite well established, its amplitude still poses a surprisingly obstinate problem. We see in this section why it is so difficult to measure. For this purpose, we discuss four ways of measuring σ_8 ; the amplitude of large-scale temperature fluctuations in the CMB, the cosmic-shear autocorrelation function, the abundance and evolution of the galaxy-cluster population, and the statistics of Lyman- α forest lines.

For historical reasons, the amplitude of the dark-matter power spectrum is characterized by the variance of the density fluctuations within spheres of $8h^{-1}$ Mpc radius. More generally, one imagines placing spheres of radius R randomly and measuring the density-contrast variance within them. Since the variance in Fourier space is characterized by the power spectrum, it can be written as

$$\sigma_R^2 = \int_0^\infty \frac{d^3k}{(2\pi)^3} P_\delta(k) W_R^2(k), \quad (267)$$

where $W_R(k)$ is a window function selecting the k modes contributing to the variance within the spheres.

Imagining spheres of radius R in real space, the window function should be the Fourier transform of a step

function, which is inconvenient because it extends to infinite wave numbers. It is thus more common to use either Gaussians since they Fourier transform to Gaussians or step functions in Fourier space. For simplicity of the following illustrative calculations, we use the latter choice, thus

$$W_R(k) = \Theta(k_R - k) = \Theta\left(\frac{2\pi}{R} - k\right). \quad (268)$$

This is a step function dropping to zero at $k=2\pi/R$. Inserting this into Eq. (267) gives

$$\sigma_R^2 = \int_0^{2\pi/R} \frac{k^2 dk}{2\pi^2} P_\delta(k). \quad (269)$$

All modes larger than R contribute to the density fluctuations in spheres of radius R because all smaller modes average to zero. The normalization of the power spectrum is usually expressed in terms of σ_8 , fixing R to its historical value of $8h^{-1}$ Mpc.

B. Fluctuations in the CMB

1. The large-scale fluctuation amplitude

We saw in Sec. VI.B.3 that the long-wavelength (low- k) tail of the CMB power spectrum is caused by the Sachs-Wolfe effect, giving rise to relative temperature fluctuations [Eq. (172)] in terms of the Newtonian potential fluctuations $\delta\Phi$. The three-dimensional temperature-fluctuation power spectrum is then

$$P_\tau(k) = P_\Phi(k)/9c^4. \quad (270)$$

The Poisson equation in its form (220) implies that the power spectra of potential and density fluctuations are related through

$$P_\Phi(k) = \frac{9H_0^4}{4} \Omega_{m0}^2 \left(\frac{D_+(a_{\text{rec}})}{a_{\text{rec}}}\right)^2 \frac{P_\delta(k)}{k^4}, \quad (271)$$

where the linear growth factor $D_+(a_{\text{rec}})$ was introduced to relate the potential-fluctuation power spectrum at the time of decoupling to the present density-fluctuation power spectrum $P_\delta(k)$.

Now we need to account for projection effects. A three-dimensional mode with comoving wave number k and comoving wavelength $\lambda=2\pi/k$ appears under an angle $\theta=\lambda/w_{\text{rec}}$, where $w_{\text{rec}}\equiv w(a_{\text{rec}})$ is the comoving angular-diameter distance (177) to the CMB. The angular wave number under which the mode appears is thus

$$l \approx 2\pi/\theta \approx w_{\text{rec}}k. \quad (272)$$

Expressing now the power spectrum (270) in terms of the angular wave number l yields, with Eq. (271),

$$P_\tau(l) \propto \left(\frac{H_0}{c}\right)^4 \Omega_{m0}^2 \left(\frac{D_+(a_{\text{rec}})}{a_{\text{rec}}}\right)^2 \frac{1}{w_{\text{rec}}^2} \frac{w_{\text{rec}}^4}{l^4} P_\delta\left(\frac{l}{w_{\text{rec}}}\right), \quad (273)$$

where the factor w_{rec}^{-2} arises because of the transformation from spatial to angular wave numbers l [cf. Limber's equation (229)], and the factor w_{rec}^4/l^4 expresses the factor k^{-4} from the squared Laplacian. This shows that the angular power spectrum $P_\tau(l)$ of the large-scale CMB temperature fluctuations can only be translated into the amplitude of the dark-matter power spectrum A if the cosmological parameters are already known well enough.

A further complication is added by the integrated Sachs-Wolfe effect introduced in Sec. VI.B.6. It depends on $D_+(a)/a$ and adds secondary anisotropies to the CMB unless $D_+(a)=a$. The primordial CMB fluctuations are then lower than measured and need to be corrected by subtracting the integrated Sachs-Wolfe contribution, which adds a further dependence on the cosmological parameters.

2. Translation to σ_8

Two more complications arise in the translation of the large-scale amplitude A to σ_8 . Since structures with wave numbers larger than the peak location k_{eq} in the power spectrum contribute to σ_8 , the dependence of k_{eq} on the cosmological parameters comes in. Finally, the spectral index n_s may affect the extrapolation from large to small scales substantially because of the long lever arm between the scales involved.

Of course, one could also use the small-scale part of the CMB power spectrum for normalizing the dark-matter power spectrum. Due to the acoustic oscillations, however, this part depends in a much more complicated way on additional cosmological parameters, such as the baryon density. Reading σ_8 off the low-order multipoles is thus a safer albeit intricate procedure.

Even if the cosmological parameters are now known well enough to translate the low-order CMB multipoles to σ_8 , an additional uncertainty remains. We know that although the Universe became neutral $\sim 400\,000$ years after the Big Bang, it must have been reionized after the first stars and other sources of UV radiation formed. Since then, CMB photons are traveling through ionized material again and experience Thomson (or Compton) scattering. The optical depth for Thomson scattering is

$$\tau = \int n_e \sigma_T c dt, \quad (274)$$

where n_e is the number density of free electrons and σ_T is the Thomson scattering cross section. After propagating through the optical depth τ , the CMB fluctuation amplitude is reduced by $\exp(-\tau)$.

Of course, the CMB photons cannot disappear through Thomson scattering; thus the CMB's overall intensity cannot change in this way, but the fluctuation amplitudes are lowered in this diffusion process. The optical depth τ depends on the path length through ionized material. In view of the CMB, this means that the degree of fluctuation damping depends on the reionization redshift, i.e., the redshift after which the cosmic baryons

were transformed back into a plasma. Unless the reionization redshift is known, we cannot know by how much the CMB fluctuations were suppressed.

So far, the reionization redshift can be estimated in two ways. First, as discussed in Sec. VI.B.4, Thomson scattering creates linear polarization. Of course, the polarization due to reionized material appears superposed on the primordial polarization but on different angular scales. The characteristic scale for secondary polarization is the horizon size at the reionization redshift, which is much larger than the typical scales of the primordial polarization. Thus, the reionization redshift can be inferred from large-scale features in the CMB polarization, provided the cosmological parameters are known well enough to translate angular scales into physical scales (Zaldarriaga, 1997). Modern cosmological parameter estimates aim at fitting the available data simultaneously for all relevant parameters mostly by Monte Carlo Markov chain techniques, as explained in, Durrer (2008).

Unfortunately, this is aggravated by the polarized microwave radiation from the Milky Way. Synchrotron and dust emission can be substantially polarized and masked the CMB polarization, which can only be measured reliably if the foregrounds of galactic origin can be accurately subtracted (Page *et al.*, 2007). Thus, the degree to which the foreground polarization is known directly determines the accuracy of the σ_8 parameter derived from the CMB fluctuations. This contributes considerably to the remaining uncertainty in the σ_8 derived from the 5-yr WMAP data given in Table I.

The other way to constrain the reionization redshift uses the spectra of distant quasars. Light with wavelengths shorter than the Lyman- α wavelength cannot propagate through neutral hydrogen because it is immediately absorbed. Therefore, quasar spectra released before the reionization redshift must be completely absorbed blueward of the Lyman- α emission line. The appearance of this so-called Gunn-Peterson effect (Gunn and Peterson, 1965) at high redshift thus signals the transition from ionized into neutral material. Using this technique, the reionization was estimated to end at redshifts $\sim 6-8$ (Fan *et al.*, 2006), while the secondary polarization of the CMB implies a reionization redshift of 11.0 ± 1.4 if instantaneous reionization is assumed (Dunkley *et al.*, 2008). These apparently discrepant values do not contradict each other because a small admixture of neutral hydrogen is enough to produce the Gunn-Peterson effect, which therefore persists until reionization has completed.

C. Cosmological weak lensing

Compared to the outlined procedure to obtain σ_8 from the CMB, it appears completely straightforward to derive it from the cosmic-shear measurements. As discussed in (Sec. VIII.B.3), the cosmic-shear power spectrum is proportional to $\Omega_{m0}^{2\alpha}$ times the amplitude A of the dark-matter power spectrum, which leads to the ap-

proximate degeneracy $\Omega_{m0}^\alpha \sigma_8 \approx \text{const}$ between σ_8 and the matter-density parameter Ω_{m0} .

A more subtle dependence on Ω_{m0} and to some degree also on other cosmological parameters is introduced by the geometrical weight function $\bar{W}(w', w)$ shown in Eq. (232) and by the growth of the power spectrum along the line of sight. This slightly modifies the form of the $\sigma_8 - \Omega_{m0}$ degeneracy but does not lift it. Knowing Ω_{m0} well enough, we should be able to read σ_8 off the cosmic-shear correlation function. However, there are three problems associated with that.

First, the cosmic shear measured on angular scales below $\sim 10'$ is heavily influenced by the onset of nonlinear structure growth and the effect of this has on the dark-matter power spectrum. While the linear growth factor can be straightforwardly calculated analytically, nonlinear growth can only be quantified by means of large numerical simulations and recipes derived from them (Peacock and Dodds, 1996; Smith, Peacock, *et al.*, 2003). Insufficient knowledge of the nonlinear dark-matter power spectrum is a major uncertainty in the cosmological interpretation of cosmic shear.

Second, the amplitude of cosmological weak-lensing effects depends on the redshift distribution of the sources used for measuring ellipticities. Since these background galaxies are typically very faint, it is demanding to measure their redshifts. Two methods have typically been used. One adapts the known redshift distribution of sources in narrow very deep observations such as the Hubble deep field to the characteristics of the observation to be analyzed. The other relies on photometric redshifts, i.e., redshift estimates based on multi-band photometry. Yet, the precise redshift distribution of the background sources adds additional uncertainty to estimates of σ_8 .

Third, it is possible that systematic effects remain in weak-lensing measurements because the effect is so small, and many corrections have to be applied to measured ellipticities before the cosmic shear can be extracted. Advanced correction methods have been developed which made the B -mode contamination almost or completely disappear. This is good news, but it does not yet guarantee the absence of other systematic effects in the data.

Nonetheless, cosmic lensing, combined with estimates of the matter-density parameter, is perhaps the most promising method for precisely determining σ_8 . Table II lists values of σ_8 derived from some cosmic-shear measurements under the assumption of $\Omega_{m0}=0.30$ in a spatially flat universe.

The systematic deviations between them are probably due to three different uncertainties. First, the redshift distribution of the background sources needs to be known; second, nonlinear evolutions of the matter power spectrum need to be accurately modeled; and third, all kinds of PSF distortions need to be corrected.

TABLE II. Values for σ_8 derived from cosmic-shear measurements under the assumption of a spatially flat universe with $\Omega_{m0}=0.3$.

σ_8	Data	Reference
$0.86^{+0.09}_{-0.13}$	RCS	Hoekstra, Yee, and Gladders, 2002
$0.71^{+0.12}_{-0.16}$	CTIO	Jarvis <i>et al.</i> , 2003
0.72 ± 0.09	Combo-17	Brown <i>et al.</i> , 2003
0.97 ± 0.13	Keck-II	Bacon <i>et al.</i> , 2003
1.02 ± 0.16	HST/STIS	Rhodes <i>et al.</i> , 2004
0.83 ± 0.07	Virgos-Descart	Van Waerbeke <i>et al.</i> , 2005
0.68 ± 0.13	GEMS	Heymans <i>et al.</i> , 2005
0.85 ± 0.06	CFHTLS-wide	Hoekstra <i>et al.</i> , 2006
0.80 ± 0.1	GaBoDS	Hetterscheidt <i>et al.</i> , 2007
$0.866^{+0.085}_{-0.068}$	COSMOS	Massey <i>et al.</i> , 2007b
0.74 ± 0.04	100 sq. deg combined	Benjamin <i>et al.</i> , 2007
0.70 ± 0.04	CFHTLS wide	Fu <i>et al.</i> , 2008

D. Galaxy clusters

1. The mass function

Based on the assumption that the density contrast is a Gaussian random field and the spherical-collapse model (Press and Schechter, 1974) derived a mass function for dark-matter halos. It compares the standard deviation σ_R of the density-fluctuation field to the linear density-contrast threshold $\delta_c \approx 1.686$ for collapse in the spherical-collapse model. The mean mass contained in spheres of radius R sets the halo mass, which brings the mean (dark-)matter density $\bar{\rho}$ into the game.

The standard deviation σ_R is related to the power spectrum. For convenience, we introduce an effective slope

$$n = d \ln P(k) / d \ln k \quad (275)$$

for the power spectrum, which will of course be scale dependent. On large scales, $n \approx 1$, while $n \rightarrow -3$ on small scales, i.e., for small halo masses. For galaxy clusters, $n \approx -1$.

We introduce the nonlinear mass scale M_* as the mass contained in spheres of radius R chosen such that $\sigma_R = 1$. Since σ_R grows with the linear growth factor $D_+(a)$, the nonlinear mass grows with time. It is convenient here to express the amplitude of the power spectrum, and thus σ_8 , in terms of M_* . In sufficient approximation,

$$\sigma_R = (M_*/M)^\alpha, \quad \alpha \equiv \frac{1}{2}(1 + n/3). \quad (276)$$

In terms of the dimensionless mass $m \equiv M/M_*$, the Press-Schechter mass function can be cast into the form

$$N(m,a)dm = \sqrt{\frac{2}{\pi}} \frac{\bar{\rho} \delta_c}{M_*^2 D_+(a)} \alpha m^{\alpha-2} \times \exp\left(-\frac{\delta_c^2}{2D_+^2(a)} m^{2\alpha}\right) dm. \quad (277)$$

The Press-Schechter mass function and some improved variants of it (Jenkins *et al.*, 2001; Sheth and Tormen, 2002) have been confirmed by numerical simulations (Springel *et al.*, 2005). It shows that the mass function is a power law with an exponential cutoff near the nonlinear mass scale M_* . For galaxy clusters, $n \approx -1$, thus $\alpha \approx 1/3$, and

$$N(m,a)dm \propto m^{-5/3} \exp\left(-\frac{\delta_c^2}{2D_+^2(a)} m^{2/3}\right) dm, \quad (278)$$

with an amplitude characterized by M_* , the mean dark-matter density $\bar{\rho}$, and the growth factor $D_+(a)$.

This opens a way to constrain cosmological parameters as well as σ_8 with galaxy clusters: if the abundance and evolution of the cluster mass function can be measured, they can be determined from the mass scale of the exponential cutoff and the amplitude of the power-law end. Today, the nonlinear mass scale is a few times $10^{13} M_\odot$. Therefore, the exponential cutoff in the halo mass will not be seen in the galaxy mass function. Clusters, however, show a pronounced exponential cutoff (Rosati *et al.*, 2002), and thus their population is very sensitive to changes in σ_8 . In principle, therefore, σ_8 should be well constrained by the cluster population.

2. What is a cluster's mass?

The main problem here is how observable cluster properties should be related to quantities used in theory. Cluster masses, as used in the theoretical mass function (278), are not observables. Cluster observables are the x-ray temperature and flux, the optical luminosity and the velocity distribution of their galaxies, and their gravitational-lensing effects. Before we discuss their relation to mass, we first see what the ‘‘mass of a galaxy cluster’’ could be.

It is easy to define masses of gravitationally bound, well localized objects, such as planets or stars. They have

TABLE III. Values of σ_8 derived from the galaxy-cluster population based on different observational data.

σ_8	Data	Reference
1.02 ± 0.07	<i>M-T</i> relation	Pierpaoli <i>et al.</i> , 2001
0.77 ± 0.07	<i>M-T</i> relation	Seljak, 2002
$0.68^{+0.11}_{-0.09}$	<i>M-L</i> relation	Reiprich and Böhringer, 2002
0.75 ± 0.16	Lensing masses	Smith, Edge, <i>et al.</i> , 2003
$0.79^{+0.06}_{-0.07}$	Luminosity function	Pierpaoli <i>et al.</i> , 2003
$0.77^{+0.05}_{-0.04}$	Temperature function	Pierpaoli <i>et al.</i> , 2003
0.69 ± 0.03	Lensing masses	Allen <i>et al.</i> , 2003
0.78 ± 0.17	Optical richness	Eke <i>et al.</i> , 2006
$0.67^{+0.04}_{-0.05}$	Lensing masses	Dahle, 2006

a well-defined boundary, e.g., the planetary surfaces or the stellar photospheres. This is markedly different for objects such as galaxies and galaxy clusters. As far as we know, their densities drop smoothly toward zero like power laws, $\propto r^{-(2-3)}$. Thus, although they are gravitationally bound, it is less obvious what should be seen as their outer boundary. Strictly speaking, there is none.

The only way out is then to define an outer boundary in such a way that it is well defined in theory and identifiable in observational data. A common choice was introduced in Sec. V.A.2: it defines the boundary by the mean overdensity it encloses. Although this is problematic as well, it may be as good as it gets. Three immediately obvious problems created by this definition are that objects such as galaxy clusters are often irregularly shaped rather than spherical, that the overdensity of 200 is as arbitrary as any other even if it is inspired by virial equilibrium in the spherical-collapse model, and that its measurement requires a sufficiently accurate density profile to be known or assumed.

How could standardized radii such as R_{200} be measured? This could for instance be achieved applying equations such as Eq. (148) after measuring the slope β and the core radius of the x-ray surface-brightness profile together with the x-ray temperature, by calibrating an assumed density profile with galaxy kinematics based on the virial theorem, or by constraining the cluster mass profile with gravitational lensing.

Obviously, all these measurements have their own problems. Being sensitive to all mass along the line of sight, gravitational lensing cannot distinguish between mass bound to a cluster or just projected onto it. Any measurement based on the virial theorem must of course rely on virial equilibrium, which takes time to be established and is often perturbed in real clusters because of merging and accretion. The common interpretation of x-ray measurements requires the assumption that the x-ray gas be in hydrostatic equilibrium with the host cluster's gravitational potential.

This illustrates that it may be fair to say that there is no such thing as the mass of a galaxy cluster. Even if measurements of cluster “radii” were less dubious, it remained unclear whether they mean the same as those

assumed in theory, which are related to the spherical-collapse model. Interestingly, but not surprisingly, cluster masses obtained from numerical simulations suffer from the same poor definition of the concept of a “cluster radius.”

How can we make progress then? Observables such as the cluster temperature T_X or its x-ray luminosity L_X should be related to the depth of the gravitational potential they are embedded in, which should in turn be related to some measure of the total mass. If we can calibrate such expected temperature-mass or luminosity-mass relations, e.g., using numerical simulations of galaxy clusters, a direct comparison between theory and observations seems possible. This is sometimes called an *external calibration* of the required relations.

Internal or *self-calibrations*, i.e., calibrations based on cluster data alone, have become increasingly fashionable over the past years. Here empirical temperature-mass and luminosity-mass relations are obtained based on one or more of the mass estimates sketched above.

The result of both procedures is qualitatively the same. It allows the conversion of observables to mass and thus of the observed cluster temperature or luminosity functions to mass functions, which can then be compared to theory. The shape and amplitude of the power spectrum and the growth factor can then be adapted to optimize the agreement between observed and expected mass functions. Clusters at moderate or high redshift constrain the evolution of the mass function and allow an independent estimate of the matter-density parameter Ω_{m0} , as sketched in Sec. V.C.

In view of the many difficulties listed, it is an astonishing fact that, when applied to cluster samples rather than individual clusters, the determination of the cluster mass function and its evolution seems to work quite well. Values for σ_8 derived therefrom are given in Table III. Systematic differences between these values are most likely due to the uncertainties of the calibration procedures applied to the relations between cluster masses and observables.

TABLE IV. Selection of σ_8 values obtained from Lyman- α forest data alone.

σ_8	Data	Reference
0.73 ± 0.04	Keck spectra	Croft <i>et al.</i> , 2002
0.94 ± 0.08	LUQAS sample, Keck	Viel <i>et al.</i> , 2004
0.91 ± 0.07	SDSS spectra	Viel and Haehnelt, 2006
0.92 ± 0.09	LUQAS sample	Zaroubi <i>et al.</i> , 2006

E. The Lyman- α forest

The Lyman- α forest lines mentioned before arise from absorption in neutral-hydrogen clouds. It is reasonable to assume that they are located where the dark matter is overdense, such that fluctuations in the neutral-hydrogen density are proportional to the dark-matter-density contrast δ . Then, observations of the Lyman- α forest lines, in particular their number per unit redshift, equivalent-width distribution and correlation properties, must contain information on the shape and the normalization of the dark-matter power spectrum.

Retrieving this information would be straightforward if the biasing relation between the neutral-hydrogen and dark-matter densities was known and simple, the gas temperature was known, redshifts were unaffected by peculiar motions, and nonlinear structure evolution could be neglected. While this is not the case in reality, these perturbing effects can be calibrated with numerical simulations and corrected. Two different methods have been proposed; one inverts the Lyman- α forest directly (Nusser and Haehnelt, 1999), while the other adapts power spectra of numerical simulations to those recovered from Lyman- α forest observations (Croft *et al.*, 1998). Both methods have allowed interesting constraints which are summarized in Table IV.

The method is young but promising. Values of σ_8 obtained so far seem to be typically systematically higher than those derived from other observables. Possible sources of systematic error are the onset of nonlinear structure growth and, perhaps most importantly, the temperature of the hydrogen gas and its relation to the gas density (often called its equation of state).

XI. INFLATION AND DARK ENERGY

A. Cosmological inflation

1. Motivation

In the preceding sections, we have seen the remarkable success of the cosmological standard model, which is built upon the two symmetry assumptions underlying the class of Friedmann-Lemaître-Robertson-Walker models which experienced a Big Bang a finite time ago. We now discuss a fundamental problem of these models and a possible way out. Historically, the problem was raised in a different way, but it intrudes with the very straightforward realization that it is by no means obvious why the CMB should appear as isotropic as it is, and why there should be large coherent structures in it.

We begin with the so-called *comoving particle horizon*, which is the comoving distance that light can travel between the Big Bang and time t . It is given by Eq. (176) with the sound speed c_s replaced by the light speed c ,

$$w_H = \int_0^{t_{\text{rec}}} \frac{cdt}{a} = \frac{2c\sqrt{a_{\text{rec}}}}{H_0\sqrt{\Omega_{m0}}}(\sqrt{1+\alpha}-\sqrt{\alpha}) = 282.8 \text{ Mpc}, \quad (279)$$

with $\alpha \approx 0.33$ as defined below Eq. (165). On the other hand, we have seen in Eq. (177) that the comoving angular-diameter distance to the CMB is

$$w(a_{\text{rec}}) = 3.195 \frac{c}{H_0} \left(\frac{\Omega_{m0}}{0.3} \right)^{-0.4} \text{ Gpc}, \quad (280)$$

which implies that the angular size of the particle horizon is

$$\theta_{\text{rec}} = w_H/w(a_{\text{rec}}) \approx 1.14^\circ (\Omega_{m0}/0.3)^{-0.1}. \quad (281)$$

The physical meaning of the particle horizon is that no event between the Big Bang and recombination can exert any influence on a given particle if it is more than the horizon length away. Our simple calculation thus shows that we can understand how causal processes could establish identical physical conditions in patches of the sky with about 1° radius. Points on the CMB separated by larger angles were never causally connected before the CMB was released. It is therefore not at all plausible how the CMB could have attained almost the same temperature across the entire sky. The simple fact that the CMB is almost entirely isotropic across the sky thus possesses a problem which the standard cosmological model is apparently unable to solve. Moreover, the formation of coherent structures larger than the particle horizon remains mysterious. This is one way to state the *horizon problem*. It is sometimes called the *causality problem*: How can coherent structures in the CMB be larger than the particle horizon was at recombination?

Another uncomfortable problem of the standard cosmological model is the flatness or at least the near flatness of spatial hypersurfaces of our Universe. To see this, we write Friedmann's equation [Eq. (6)] in the form

$$H^2(a) = H^2(a)[\Omega_{\text{tot}}(a) - Kc^2/a^2H^2], \quad (282)$$

which is equivalent to

$$\Omega_{\text{tot}}(a) - 1 = Kc^2/a^2H^2. \quad (283)$$

The right-hand side typically grows as some power of the time t ,

$$(a^2 H^2)^{-1} = \dot{a}^{-2} \propto t^\beta, \quad (284)$$

e.g., $\beta=2/3$ in a matter-dominated universe without cosmological constant. Then,

$$\Omega_{\text{tot}}(a) - 1 \propto t^\beta. \quad (285)$$

This shows that any deviation of the total density parameter Ω_{tot} from unity tends to grow with time. Thus, (spatial) flatness is an unstable property. If it is not very precisely flat in the beginning, the Universe will develop away from flatness. Since we know that spatial hypersurfaces are now almost flat, $|\Omega_{\text{tot}}(a) - 1| \lesssim 1\%$ (cf. Table 1), the deviation from flatness must have been of order

$$|\Omega_{\text{tot}}(a_{\text{rec}}) - 1| \lesssim 1\% \times (t_{\text{rec}}/t_0)^\beta \approx 10^{-5} \quad (286)$$

or ten parts per million at the time of recombination. Clearly, this requires enormous fine tuning. This is called the *flatness problem*: How can we understand flatness in the late Universe without assuming an extreme degree of fine tuning at early times?

2. The idea of inflation

Since c/H is the Hubble radius, the quantity $r_H \equiv c/aH$ is the comoving Hubble radius. According to Eq. (284), it typically grows with time as $r_H \propto t^{\beta/2}$. Since we can write Eq. (283) as

$$\Omega_{\text{tot}}(a) - 1 = Kr_{\text{H}}^2, \quad (287)$$

this is equivalent to the flatness problem.

This motivates the idea that at least the flatness problem may be solved if the comoving Hubble radius could, at least for some sufficiently long period, *shrink* with time. If that could be arranged, any deviation of $\Omega_{\text{tot}}(a)$ from unity would be driven toward zero.

Conveniently, such an arrangement would also remove or at least alleviate the causality problem. Possibly, the Hubble radius, characterizing the radius of the observable Universe, could be driven inside the horizon and thus move the entire observable Universe into a causally connected region. When the hypothesized epoch of a shrinking comoving Hubble radius is over, it starts expanding again, but if the reduction was sufficiently large, it could remain within the causally connected region at least until the present.

How could such a *shrinking* comoving Hubble radius be arranged? Obviously, we require

$$\frac{d}{dt} \frac{c}{aH} = - \frac{c}{(aH)^2} (\dot{a}H + a\dot{H}) = - \frac{c\ddot{a}}{(aH)^2} < 0, \quad (288)$$

which is possible if and only if $\ddot{a} > 0$, in other words, if the expansion of the Universe *accelerates*. This appears counterintuitive because the cosmic expansion is dominated by gravity, which should be attractive and thus necessarily *decelerate* the expansion. Friedmann's equation (7) implies the matter condition

$$\rho c^2 + 3p < 0 \Rightarrow p < -\rho c^2/3. \quad (289)$$

In other words, cosmic acceleration is possible if and only if the dominant ingredient of the cosmic fluid has

sufficiently negative pressure. Equation (8) implies the density evolution

$$\frac{\dot{\rho}}{\rho} = -3 \frac{\dot{a}}{a} \left(1 + \frac{p}{\rho c^2} \right) < -2 \frac{\dot{a}}{a} \quad (290)$$

for a cosmic fluid satisfying Eq. (289), showing that its density would fall off flatter than a^{-2} and thus less steeply than the matter or radiation densities. Thus, once a component of the cosmic fluid with sufficiently negative pressure reaches a density comparable to the densities of matter or radiation, it quickly starts dominating the cosmic expansion. In the limiting case $\dot{\rho}=0$ or $p=-\rho c^2$, Eq. (7) reduces to

$$\frac{\ddot{a}}{a} = \frac{8\pi G}{3} \rho = \text{const} > 0, \quad (291)$$

which implies the exponential expansion or inflation

$$a \propto \exp \left[\left(\frac{8\pi G}{3} \rho \right)^{1/2} t \right]. \quad (292)$$

3. Slow roll, structure formation, and observational constraints

We have seen that we need inflation to solve the flatness and causality problems, and inflation needs a form of matter with negative pressure. What could that be? Consider a scalar field ϕ with a self-interaction potential $V(\phi)$. Then, field theory shows that pressure and density of the scalar field are related by the equation of state

$$p_\phi = w\rho_\phi c^2 \quad \text{with} \quad w \equiv \frac{\frac{1}{2}\dot{\phi}^2 - V}{\frac{1}{2}\dot{\phi}^2 + V}. \quad (293)$$

Evidently, negative pressure is possible if the kinetic energy of the scalar field is sufficiently smaller than its potential energy. For the cosmological-constant case, $\dot{\phi}=0$, we have $w=-1$ or $p=-\rho c^2$, in agreement with the conclusion from Eq. (290). In other words, a suitably strongly self-interacting scalar field has exactly the properties we need.

Inflation, i.e., accelerated expansion, broadly requires $\dot{\phi}^2$ to be sufficiently smaller than V . Moreover, we need inflation to operate long enough to drive the total matter-density parameter sufficiently close to unity for it to remain there to the present day. These two conditions are conventionally cast into the form

$$\epsilon \equiv \frac{1}{24\pi G} \left(\frac{V'}{V} \right)^2 \ll 1 \quad \text{and} \quad \eta \equiv \frac{1}{8\pi G} \frac{V''}{V} \ll 1 \quad (294)$$

[see Liddle and Lyth (2000)]. They are called the slow-roll conditions. The first assures that inflation can set in because if it is satisfied, the potential has a small gradient and cannot drive rapid changes of the scalar field. The second restricts the curvature of the potential and thus assures that the inflationary condition is satisfied long enough.

Estimates show that inflation needs to expand the Universe by $\sim 50\text{--}60$ e foldings (Alabidi and Lyth, 2006) (i.e., by a factor of $e^{50\text{--}60}$) for it to solve the causality and flatness problems. Inflation ends once the slow-roll conditions are violated. By then, the Universe will have become extremely cold. While the density of the inflaton field ϕ will be approximately the same as at the onset of inflation (as for the cosmological constant, this is a consequence of the negative pressure), all other matter and radiation fields will have their energy densities lowered by factors of $a^{-3\text{--}4}$, i.e., by ≤ 100 orders of magnitude.

Once ϵ approaches unity, the kinetic term $\dot{\phi}^2$ will dominate the potential, and the scalar field will start oscillating rapidly. It is assumed that the scalar field then decays into ordinary matter which fills or *reheats* the Universe after inflation is over.

It is an extremely interesting aspect of inflation that it also provides a mechanism for seeding structure formation (Mukhanov and Chibisov, 1981). As any other quantum field, the inflaton field ϕ must have undergone vacuum oscillations because the zero-point energy of a quantum harmonic oscillator cannot vanish due to Heisenberg's uncertainty principle. These vacuum oscillations cause the spontaneous creation and annihilation of particle-antiparticle pairs. Once inflation sets in, vacuum fluctuation modes are quickly driven out of the horizon and lose causal connection. Then, they cannot decay any more and “freeze in.” Thus, inflation introduces the breath-taking notion that density fluctuations in our Universe today may have been seeded by vacuum fluctuations of the inflaton field before inflation set in and enlarged them to cosmological scales.

This idea has precisely quantifiable consequences (Guth and Pi, 1982; Pagels, 1983; Brandenberger, 1984; Halliwell and Hawking, 1985). First, linear density fluctuations created by the inflaton field must be adiabatic and, by the central limit theorem, they should form a Gaussian random field. This is because they arise from incoherent superposition of extremely many independent fluctuation modes whose amplitude and wave number are all drawn from the same probability distribution. Under these circumstances, the central limit theorem shows that the result, i.e., the superposition of all these modes, must be a Gaussian random field.

Second, it implies that the statistics of density fluctuations in the Universe today must be explicable by the statistics of vacuum fluctuations in a scalar quantum field. This is indeed the case. The power spectrum resulting from this consideration is very close to the scale-free Harrison-Zel'dovich-Peebles shape introduced in Sec. I.C.2,

$$P_{\delta}(k) \propto k^{n_s}, \quad (295)$$

with $n_s \approx 1$. The spectral index n_s would be precisely unity if inflation lasted forever. Since this was obviously not so, n_s must deviate slightly from unity, and detailed calculations show that it must be slightly smaller (Liddle and Lyth, 2000; Alabidi and Lyth, 2006),

$$n_s = 1 + 2\eta - 6\epsilon. \quad (296)$$

The latest WMAP measurements (Komatsu *et al.*, 2009) do in fact show that

$$n_s = 0.960^{+0.014}_{-0.013} \quad (297)$$

(cf. Table I). The completely scale-invariant spectrum, $n_s=1$, is thus excluded at more than 3σ . The measured deviation of n_s from unity also restricts the number N of e foldings completed by inflation. Under fairly general assumptions,

$$N = 54 \pm 7 \quad (298)$$

(Alabidi and Lyth, 2006) based on the three-year WMAP data.

Another prediction of inflation is that it may excite not only scalar but also tensor perturbations (Liddle and Lyth, 2000). Scalar perturbations lead to the density fluctuations; tensor perturbations correspond to gravitational waves. Vector perturbations do not play any role because they decay quickly as the Universe expands. Simple models of inflation predict that the ratio r between the amplitudes of tensor and scalar perturbations, taken in the limit of small wave numbers, is

$$r = 16\epsilon. \quad (299)$$

An inflationary background of gravitational waves is in principle detectable through the polarization of the CMB (Seljak and Zaldarriaga, 1997). Limits of order $r \leq 0.05$ are expected from the upcoming Planck satellite (Kinney, 1998; Kamionkowski and Jaffe, 2001). Together with the result $n_s \neq 1$ from WMAP, it will then be possible to constrain viable inflation models, i.e., to constrain the shape of the inflaton potential.

B. Dark energy

1. Motivation

The CMB shows us that the Universe is at least nearly spatially flat. Constraints from kinematics, from cluster evolution, and from the CMB show that the matter density alone cannot be responsible for flattening space, and primordial nucleosynthesis and the CMB show that baryons contribute at a very low level only. Something is missing, and it even dominates today's cosmic fluid.

From structure formation, we know that this remaining constituent cannot clump on the scales covered by the galaxy surveys and below. It is thus different from dark matter. The terms *dark energy*, *kosmon*, or *quintessence* have been coined for it (Peebles and Ratra, 1988, 2003; Wetterich, 1988). The type-Ia supernovae tell us that it behaves at least very similar to a cosmological constant in the recent cosmic past. Maybe the dark energy is a cosmological constant? Nothing currently indicates any deviation from this “simplest” assumption (see, e.g., Komatsu *et al.*, 2009). So far, the cosmological constant is a perfectly viable description for all observational evidence we have. However, this is deeply dissatisfactory from the point of view of theoretical physics.

The problem is the value of $\Omega_{\Lambda 0}$. As we have seen above, a self-interacting scalar field with negligible kinetic energy behaves like a cosmological constant. Then, its density should simply be given by its potential V . Simple arguments suggest that V should be the Planck mass divided by the third power of the Planck length, which turns out to be 120 orders of magnitude larger than the cosmological constant derived from observations. Since this fails, it seems natural to expect that the cosmological constant should vanish, but it does not. The main problem with the cosmological constant is therefore why is it not zero if it is so small?

Anthropic arguments suggest that we observe the Universe as it is because it needs to be that way for us to exist. The Universe needs to be old enough for stars to have produced carbon, on which life must be based to the best of our knowledge. Yet, it must not be too old for the majority of stars to have evolved past their main-sequence life for the stability of benign conditions for life. If the cosmological constant was much larger, inflationary expansion would have prohibited structure formation and thus also the formation of life. It may thus be that the cosmological parameters have the values we measure because otherwise we would not exist to measure them.

The explanation of inflation by means of an inflaton field suggests another way out. As we have seen there, accelerated expansion can be driven by a self-interacting scalar field while its potential energy dominates. Moreover, it can be shown that if the potential V has an appropriate shape, the dark energy has attractor properties in the sense that a vast range of initial density values can evolve toward the same value today (Zlatev *et al.*, 1999). At this point at the latest, we leave the realm of what may be considered the established cosmological standard model and enter into the very controversial discussion of dark energy.

2. Observational constraints?

If the dark energy is indeed dynamical and provided by a self-interacting scalar field, how can we find out more about it? Reviewing the cosmological measurements we have discussed so far, it becomes evident that they are all derived from constraints on cosmic time, as in the age of the Galaxy or of globular clusters, or in primordial nucleosynthesis; distances, as in the spatial flatness derived from the CMB, the type-Ia supernovae or the geometry of cosmological weak lensing; or the growth of cosmic structures, as in the acoustic oscillations in the CMB, the evolution of the cluster population, the structures in the galaxy distribution, or the source of cosmological weak-lensing effects.

We must therefore seek to constrain the dark energy by measurements of distances, times, and structure growth. Since they can all be traced back to the expansion behavior of the Universe as described by Friedmann's equation, we must see how the dark energy enters there and what effects it can seed through it.

We therefore assume that the dark energy is a suitably self-interacting homogeneous scalar field. Then, its pressure can be described by

$$p = w(a)\rho c^2, \quad (300)$$

where the equation-of-state parameter w is some function of a . According to Eq. (289), accelerated expansion needs $w < -1/3$, and the cosmological constant corresponds to $w = -1$. Since all cosmological measurements to date are in agreement with the assumption of a cosmological constant, we need to arrange things such that $w \rightarrow -1$ today. Suppose we had some function $w(a)$, which could be obtained either from a phenomenological choice, a model for the self-interaction potential $V(\phi)$ through Eq. (293) or from a suitable ad hoc parameterization. Then, Eq. (290) implies

$$\dot{\rho}/\rho = -3(1+w)\dot{a}/a \quad (301)$$

or

$$\rho(a) = \rho_0 \exp\left\{-3 \int_1^a [1+w(a')] \frac{da'}{a'}\right\} \equiv \rho_0 f(a). \quad (302)$$

For constant w , this simplifies to

$$\rho(a) = \rho_0 \exp[-3(1+w)\ln a] = \rho_0 a^{-3(1+w)}. \quad (303)$$

If $w = -1$, we recover the cosmological-constant case $\rho = \rho_0 = \text{const}$ for pressureless material, $w = 0$ and $\rho \propto a^{-3}$, and for radiation, $w = 1/3$ and $\rho \propto a^{-4}$.

Therefore, we can take account of the dynamical dark energy by replacing the term $\Omega_{\Lambda 0}$ in the Friedmann equation (10) by $\Omega_{\text{DE}0}f(a)$, and the expansion function $E(a)$ turns into

$$E(a) = [\Omega_{r0}a^{-4} + \Omega_{m0}a^{-3} + \Omega_{\text{DE}0}f(a) + \Omega_{K0}a^{-2}]^{1/2}, \quad (304)$$

where $\Omega_{K0} = 1 - \Omega_{r0} - \Omega_{m0} - \Omega_{\text{DE}0}$ is a density parameter assigned to the spatial curvature.

We thus see that the equation-of-state parameter enters the expansion function in integrated form. Since all cosmological observables are integrals over the expansion function, including the growth factor $D_+(a)$, this implies that cosmological observables measure integrals over the integrated equation-of-state function $w(a)$ (see Fig. 12). Note that in cosmological models with dynamical dark energy, the growth factor is more complicated than described by Eq. (23) because dark-energy clustering needs to be taken into account (see, e.g., Kunz and Sapone, 2007). Needless to say, the dependence of cosmological measurements on the exact form of $w(a)$ will be extremely weak, which in turn implies that extremely accurate measurements will be necessary for constraining the nature of the dark energy.

In order to illustrate the required accuracies, consider by how much the angular-diameter distance and the growth factor change compared to Λ CDM upon changes in w away from -1 ,

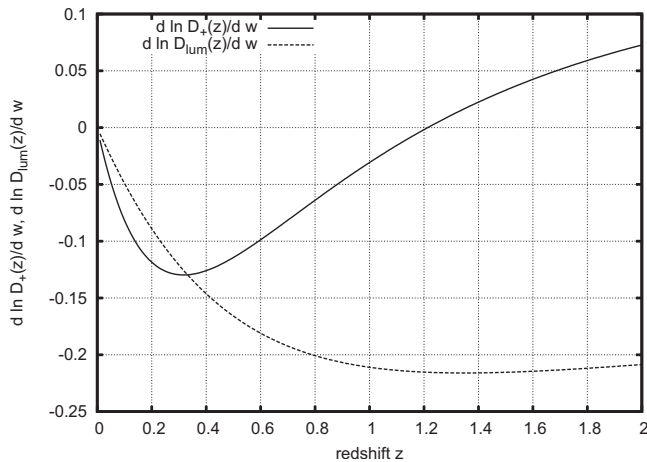


FIG. 12. Relative changes of the growth factor D_+ and the luminosity distance D_{lum} with w as functions of redshift, assuming constant w .

$$d \ln D_{\text{ang}}(z)/dw, \quad d \ln D_+(z)/dw, \quad (305)$$

as a function of redshift z . Assuming $\Omega_{m0}=0.3$ and $\Omega_{\Lambda 0}=0.7$, we find typical values between -0.1 and -0.2 at most. Since we currently expect deviations of w from -1 at most at the $\sim 10\%$ level, accurate constraints on the dark energy require relative accuracies of distances and the growth factor at the percent level.

Clearly, all models for dynamical dark energy proposed so far are purely phenomenological. The most straightforward question to be addressed in this situation may be whether a cosmological constant can be ruled out in some way. All suitable cosmological information will need to be combined in order to progress.

Currently, the largest hope is put on the BAOs (see Sec. VII.A.6) and on so-called *tomographic* measurements. BAOs have a characteristic physical scale whose angular scale depends on the angular-diameter distance, which is in turn sensitive to the dark energy. Tomography attempts to trace the evolution of structures throughout cosmic history (Hu, 2002a, 2002b). An example is given by weak gravitational lensing: since its geometrical sensitivity peaks approximately half-way between the sources and the observer, sources at higher redshift also probe more distant and thus less evolved cosmic structures. If lensing effects can be measured for subsamples of sources in different redshift shells, the growth factor can be probed differentially. First examples for this technique have been published. They give rise to the expectation that clarifying the nature of the dark energy may indeed be feasible in the near future.

ACKNOWLEDGMENTS

I am most grateful to many colleagues for inspiring and clarifying discussions, in particular to Peter Schneider, Achim Weiß, and Simon White, whose detailed comments helped improving this review substantially. Three anonymous referees contributed numerous

thoughtful and constructive comments. This work was supported in part by the German Science Foundation (DFG) through the Collaborative Research Centres (Grants No. SFB 439 and No. TRR 33).

REFERENCES

- Abell, G. O., J. H. G. Corwin, and R. P. Olowin, 1989, *Astrophys. J., Suppl. Ser.* **70**, 1.
- Aguirre, A., 1999, *Astrophys. J.* **525**, 583.
- Alabidi, L., and D. H. Lyth, 2006, *J. Cosmol. Astropart. Phys.* **8**, 13.
- Alcock, C., *et al.*, 2000, *Astrophys. J.* **542**, 281.
- Allen, S. W., R. W. Schmidt, A. C. Fabian, and H. Ebeling, 2003, *Mon. Not. R. Astron. Soc.* **342**, 287.
- Alpher, R. A., and R. C. Herman, 1949, *Phys. Rev.* **75**, 1089.
- Asplund, M., D. L. Lambert, P. E. Nissen, F. Primas, and V. V. Smith, 2006, *Astrophys. J.* **644**, 229.
- Astier, P., *et al.*, 2006, *Astron. Astrophys.* **447**, 31.
- Baade, W., 1926, *Astron. Nachr.* **228**, 359.
- Baade, W., 1956, *Publ. Astron. Soc. Pac.* **68**, 5.
- Bacon, D. J., R. J. Massey, A. R. Refregier, and R. S. Ellis, 2003, *Mon. Not. R. Astron. Soc.* **344**, 673.
- Barnes, J., and P. Hut, 1986, *Nature (London)* **324**, 446.
- Bartelmann, M., and P. Schneider, 2001, *Phys. Rep.* **340**, 291.
- Benjamin, J., C. Heymans, E. Semboloni, L. van Waerbeke, H. Hoekstra, T. Erben, M. D. Gladders, M. Hettterscheidt, Y. Mellier, and H. K. C. Yee, 2007, *Mon. Not. R. Astron. Soc.* **381**, 702.
- Blandford, R., and R. Narayan, 1986, *Astrophys. J.* **310**, 568.
- Blinnikov, S. I., F. K. Röpkke, E. I. Sorokina, M. Gieseler, M. Reinecke, C. Travaglio, W. Hillebrandt, and M. Stritzinger, 2006, *Astron. Astrophys.* **453**, 229.
- Boggess, N. W., *et al.*, 1992, *Astrophys. J.* **397**, 420.
- Bond, J. R., and G. Efstathiou, 1984, *Astrophys. J., Lett. Ed.* **285**, L45.
- Brandenberger, R. H., 1984, *Nucl. Phys. B* **245**, 328.
- Brown, M. L., A. N. Taylor, D. J. Bacon, M. E. Gray, S. Dye, K. Meisenheimer, and C. Wolf, 2003, *Mon. Not. R. Astron. Soc.* **341**, 100.
- Cayrel, R., *et al.*, 2001, *Nature (London)* **409**, 691.
- Chaboyer, B., 1998, *Phys. Rep.* **307**, 23.
- Chaboyer, B., P. Demarque, P. J. Kernan, and L. M. Krauss, 1998, *Astrophys. J.* **494**, 96.
- Chandrasekhar, S., 1984, *Rev. Mod. Phys.* **56**, 137.
- Charbonnel, C., and F. Primas, 2005, *Astron. Astrophys.* **442**, 961.
- Ciardi, B., and A. Ferrara, 2005, *Space Sci. Rev.* **116**, 625.
- Cole, S., *et al.*, 2005, *Mon. Not. R. Astron. Soc.* **362**, 505.
- Coles, P., and F. Lucchin, 2002, *Cosmology: The Origin and Evolution of Cosmic Structure*, 2nd ed. (Wiley-VCH, New York), p. 512.
- Colgate, S. A., and C. McKee, 1969, *Astrophys. J.* **157**, 623.
- Colless, M., 1999, *Philos. Trans. R. Soc. London, Ser. A* **357**, 105.
- Cool, A. M., G. Piotto, and I. R. King, 1996, *Astrophys. J.* **468**, 655.
- Cowan, J. J., F.-K. Thielemann, and J. W. Truran, 1987, *Astrophys. J.* **323**, 543.
- Cowan, J. J., F.-K. Thielemann, and J. W. Truran, 1991, *Phys. Rep.* **208**, 267.
- Croft, R. A. C., D. H. Weinberg, M. Bolte, S. Burles, L. Hernquist, N. Katz, D. Kirkman, and D. Tytler, 2002, *Astrophys. J.*

- 581**, 20.
- Croft, R. A. C., D. H. Weinberg, N. Katz, and L. Hernquist, 1998, *Astrophys. J.* **495**, 44.
- Cypriano, E. S., L. J. Sodré, J.-P. Kneib, and L. E. Campusano, 2004, *Astrophys. J.* **613**, 95.
- Dahle, H., 2006, *Astrophys. J.* **653**, 954.
- Dame, T. M., D. Hartmann, and P. Thaddeus, 2001, *Astrophys. J.* **547**, 792.
- Davis, M., G. Efstathiou, C. S. Frenk, and S. D. M. White, 1985, *Astrophys. J.* **292**, 371.
- Djorgovski, S., and M. Davis, 1987, *Astrophys. J.* **313**, 59.
- Dodelson, S., 2003, *Modern Cosmology* (Academic, Amsterdam), Vol. XIII, p. 440.
- Doroshkevich, A. G., 1970, *Astrofizika* **6**, 581.
- Dressler, A., D. Lynden-Bell, D. Burstein, R. L. Davies, S. M. Faber, R. Terlevich, and G. Wegner, 1987, *Astrophys. J.* **313**, 42.
- Dunkley, J., *et al.*, 2009, *Astrophys. J., Suppl. Ser.* **180**, 306.
- Durrer, R., 2008, *The Cosmic Microwave Background* (Cambridge University Press, Cambridge).
- Efstathiou, G., M. Davis, S. D. M. White, and C. S. Frenk, 1985, *Astrophys. J., Suppl. Ser.* **57**, 241.
- Eisenstein, D. J., 2005, *New Astron. Rev.* **49**, 360.
- Eke, V. R., C. M. Baugh, S. Cole, C. S. Frenk, and J. F. Navarro, 2006, *Mon. Not. R. Astron. Soc.* **370**, 1147.
- Fan, X., C. L. Carilli, and B. Keating, 2006, *Annu. Rev. Astron. Astrophys.* **44**, 415.
- Feast, M. W., and R. M. Catchpole, 1997, *Mon. Not. R. Astron. Soc.* **286**, L1.
- Feast, M. W., and A. R. Walker, 1987, *Annu. Rev. Astron. Astrophys.* **25**, 345.
- Filippenko, A. V., 1997, *Annu. Rev. Astron. Astrophys.* **35**, 309.
- Finkbeiner, D. P., 2003, *Astrophys. J., Suppl. Ser.* **146**, 407.
- Fixsen, D. J., E. S. Cheng, J. M. Gales, J. C. Mather, R. A. Shafer, and E. L. Wright, 1996, *Astrophys. J.* **473**, 576.
- Fixsen, D. J., and J. C. Mather, 2002, *Astrophys. J.* **581**, 817.
- Fowler, W. A., 1989, *Ann. N.Y. Acad. Sci.* **571**, 68.
- Freedman, W. L., *et al.*, 1994, *Astrophys. J.* **427**, 628.
- Freedman, W. L., *et al.*, 2001, *Astrophys. J.* **553**, 47.
- Fu, L., *et al.*, 2008, *Astron. Astrophys.* **479**, 9.
- Gamow, G., 1948, *Phys. Rev.* **74**, 505.
- Gaztañaga, E., M. Manera, and T. Multamäki, 2006, *Mon. Not. R. Astron. Soc.* **365**, 171.
- Giannantonio, T., R. G. Crittenden, R. C. Nichol, R. Scranton, G. T. Richards, A. D. Myers, R. J. Brunner, A. G. Gray, A. J. Connolly, and D. P. Schneider, 2006, *Phys. Rev. D* **74**, 063520.
- Gould, A., 1995, *Astrophys. J.* **452**, 189.
- Grundahl, F., D. A. VandenBerg, R. A. Bell, M. I. Andersen, and P. B. Stetson, 2000, *Astron. J.* **120**, 1884.
- Gunn, J. E., and J. R. I. Gott, 1972, *Astrophys. J.* **176**, 1.
- Gunn, J. E., and B. A. Peterson, 1965, *Astrophys. J.* **142**, 1633.
- Guth, A. H., and S.-Y. Pi, 1982, *Phys. Rev. Lett.* **49**, 1110.
- Halliwel, J. J., and S. W. Hawking, 1985, *Phys. Rev. D* **31**, 1777.
- Hamilton, A. J. S., 1993a, *Astrophys. J. Lett.* **406**, L47.
- Hamilton, A. J. S., 1993b, *Astrophys. J.* **417**, 19.
- Hansen, B. M. S., and J. Liebert, 2003, *Annu. Rev. Astron. Astrophys.* **41**, 465.
- Hansen, B. M. S., H. B. Richer, G. G. Fahlman, P. B. Stetson, J. Brewer, T. Currie, B. K. Gibson, R. Ibata, R. M. Rich, and M. M. Shara, 2004, *Astrophys. J., Suppl. Ser.* **155**, 551.
- Harrison, E. R., 1970, *Phys. Rev. D* **1**, 2726.
- Haslam, C. G. T., C. J. Salter, H. Stoffel, and W. E. Wilson, 1982, *Astron. Astrophys. Suppl. Ser.* **47**, 1.
- Hawkins, E., *et al.*, 2003, *Mon. Not. R. Astron. Soc.* **346**, 78.
- Herschel, W., 1786, *Philos. Trans. R. Soc. London* **76**, 457.
- Herschel, W., 1789, *Philos. Trans. R. Soc. London* **79**, 212.
- Hetterscheidt, M., P. Simon, M. Schirmer, H. Hildebrandt, T. Schrabback, T. Erben, and P. Schneider, 2007, *Astron. Astrophys.* **468**, 859.
- Heymans, C., *et al.*, 2005, *Mon. Not. R. Astron. Soc.* **361**, 160.
- Heymans, C., *et al.*, 2006, *Mon. Not. R. Astron. Soc.* **368**, 1323.
- Hillebrandt, W., and J. C. Niemeyer, 2000, *Annu. Rev. Astron. Astrophys.* **38**, 191.
- Hockney, R. W., and J. W. Eastwood, 1988, *Computer Simulation using Particles* (Hilger, Bristol).
- Hoekstra, H., 2004, *Mon. Not. R. Astron. Soc.* **347**, 1337.
- Hoekstra, H., 2007, *Mon. Not. R. Astron. Soc.* **379**, 317.
- Hoekstra, H., Y. Mellier, L. van Waerbeke, E. Semboloni, L. Fu, M. J. Hudson, L. C. Parker, I. Tereno, and K. Benabed, 2006, *Astrophys. J.* **647**, 116.
- Hoekstra, H., L. van Waerbeke, M. D. Gladders, Y. Mellier, and H. K. C. Yee, 2002, *Astrophys. J.* **577**, 604.
- Hoekstra, H., H. K. C. Yee, and M. D. Gladders, 2002, *Astrophys. J.* **577**, 595.
- Holz, D. E., and R. M. Wald, 1998, *Phys. Rev. D* **58**, 063501.
- Hu, W., 2002a, *Phys. Rev. D* **66**, 083515.
- Hu, W., 2002b, *Phys. Rev. D* **65**, 023003.
- Hu, W., and N. Sugiyama, 1996, *Astrophys. J.* **471**, 542.
- Hubble, E., and M. L. Humason, 1931, *Astrophys. J.* **74**, 43.
- Hui, X., H. C. Ford, R. Ciardullo, and G. H. Jacoby, 1993, *Astrophys. J.* **414**, 463.
- Izotov, Y. I., and T. X. Thuan, 2004, *Astrophys. J.* **602**, 200.
- Jacoby, G. H., 1980, *Astrophys. J., Suppl.* **42**, 1.
- Jarvis, M., G. M. Bernstein, P. Fischer, D. Smith, B. Jain, J. A. Tyson, and D. Wittman, 2003, *Astron. J.* **125**, 1014.
- Jenkins, A., C. S. Frenk, S. D. M. White, J. M. Colberg, S. Cole, A. E. Evrard, H. M. P. Couchman, and N. Yoshida, 2001, *Mon. Not. R. Astron. Soc.* **321**, 372.
- Kaiser, N., 1987, *Mon. Not. R. Astron. Soc.* **227**, 1.
- Kaiser, N., G. Squires, and T. Broadhurst, 1995, *Astrophys. J.* **449**, 460.
- Kamionkowski, M., and A. H. Jaffe, 2001, *Int. J. Mod. Phys. A* **16**, 116.
- Kasen, D., and S. E. Woosley, 2007, *Astrophys. J.* **656**, 661.
- Kilbinger, M., and P. Schneider, 2004, *Astron. Astrophys.* **413**, 465.
- Kinney, W. H., 1998, *Phys. Rev. D* **58**, 123506.
- Klessen, R., and A. Burkert, 1996, *Mon. Not. R. Astron. Soc.* **280**, 735.
- Kochanek, C. S., 2002, *Astrophys. J.* **578**, 25.
- Kochanek, C. S., 2003, *Astrophys. J.* **583**, 49.
- Komatsu, E., *et al.*, 2009, *Astrophys. J., Suppl. Ser.* **180**, 330.
- Korn, A. J., F. Grundahl, O. Richard, P. S. Barklem, L. Mashonkina, R. Collet, N. Piskunov, and B. Gustafsson, 2006, *Nature (London)* **442**, 657.
- Kovac, J. M., E. M. Leitch, C. Pryke, J. E. Carlstrom, N. W. Halverson, and W. L. Holzapfel, 2002, *Nature (London)* **420**, 772.
- Kregel, M., and P. C. van der Kruit, 2004, *Mon. Not. R. Astron. Soc.* **352**, 787.
- Kunz, M., and D. Sapone, 2007, *Phys. Rev. Lett.* **98**, 121301.
- Lahav, O., *et al.*, 2002, *Mon. Not. R. Astron. Soc.* **333**, 961.
- Lamarre, J. M., *et al.*, 2003, *New Astron. Rev.* **47**, 1017.
- Landy, S. D., and A. S. Szalay, 1993, *Astrophys. J.* **412**, 64.

- Lasserre, T., *et al.*, 2000, *Astron. Astrophys.* **355**, L39.
- Leibundgut, B., 2001, *Annu. Rev. Astron. Astrophys.* **39**, 67.
- Leibundgut, B., and S. Blondin, 2005, *Nucl. Phys. B (Proc. Suppl.)* **138**, 10.
- Liddle, A. R., and D. H. Lyth, 2000, *Cosmological Inflation and Large-Scale Structure* (Cambridge University Press, Cambridge), p. 414.
- Madgwick, D. S., *et al.*, 2002, *Mon. Not. R. Astron. Soc.* **333**, 133.
- Madore, B. F., and W. L. Freedman, 1991, *Publ. Astron. Soc. Pac.* **103**, 933.
- Massey, R., *et al.*, 2007a, *Mon. Not. R. Astron. Soc.* **376**, 13.
- Massey, R., *et al.*, 2007b, *Astrophys. J., Suppl. Ser.* **172**, 239.
- Mather, J. C., *et al.*, 1994, *Astrophys. J.* **420**, 439.
- McDonald, P., *et al.*, 2005, *Astrophys. J.* **635**, 761.
- Mellier, Y., 1999, *Annu. Rev. Astron. Astrophys.* **37**, 127.
- Meyer, B. S., and D. N. Schramm, 1986, *Astrophys. J.* **311**, 406.
- Monaghan, J. J., 2005, *Rep. Prog. Phys.* **68**, 1703.
- Mukhanov, V. F., and G. V. Chibisov, 1981, *JETP Lett.* **33**, 532.
- Nolta, M. R., *et al.*, 2009, *Astrophys. J., Suppl. Ser.* **180**, 296.
- Norberg, P., *et al.*, 2001, *Mon. Not. R. Astron. Soc.* **328**, 64.
- Nusser, A., and M. Haehnelt, 1999, *Mon. Not. R. Astron. Soc.* **303**, 179.
- Östman, L., and E. Mörtzell, 2005, *J. Cosmol. Astropart. Phys.* **2**, 5.
- Oswalt, T. D., J. A. Smith, M. A. Wood, and P. Hintzen, 1996, *Nature (London)* **382**, 692.
- Padmanabhan, T., 1993, *Structure Formation in the Universe* (Cambridge University Press, Cambridge), p. 499.
- Page, L., *et al.*, 2007, *Astrophys. J., Suppl. Ser.* **170**, 335.
- Pagels, H. R., 1983, *Astrophys. Lett.* **23**, 151.
- Panagia, N., R. Gilmozzi, F. Macchetto, H.-M. Adorf, and R. P. Kirshner, 1991, *Astrophys. J. Lett.* **380**, L23.
- Patterson, C., 1956, *Geochim. Cosmochim. Acta* **10**, 230.
- Peacock, J. A., 1999, *Cosmological Physics* (Cambridge University Press, Cambridge), p. 704.
- Peacock, J. A., and S. J. Dodds, 1996, *Mon. Not. R. Astron. Soc.* **280**, L19.
- Peebles, P. J., and B. Ratra, 2003, *Rev. Mod. Phys.* **75**, 559.
- Peebles, P. J. E., 1973, *Astrophys. J.* **185**, 413.
- Peebles, P. J. E., 1982, *Astrophys. J., Lett. Ed.* **263**, L1.
- Peebles, P. J. E., 1993, *Principles of Physical Cosmology*, Princeton Series in Physics (Princeton University Press, Princeton, NJ).
- Peebles, P. J. E., and B. Ratra, 1988, *Astrophys. J., Lett. Ed.* **325**, L17.
- Peebles, P. J. E., and J. T. Yu, 1970, *Astrophys. J.* **162**, 815.
- Peimbert, M., V. Luridiana, and A. Peimbert, 2007, *Astrophys. J.* **666**, 636.
- Penzias, A. A., and R. W. Wilson, 1965, *Astrophys. J.* **142**, 419.
- Percival, W. J., *et al.*, 2007, *Astrophys. J.* **657**, 645.
- Perlmutter, S., *et al.*, 1999, *Astrophys. J.* **517**, 565.
- Pettini, M., and D. V. Bowen, 2001, *Astrophys. J.* **560**, 41.
- Phillips, M. M., P. Lira, N. B. Suntzeff, R. A. Schommer, M. Hamuy, and J. Maza, 1999, *Astron. J.* **118**, 1766.
- Pierpaoli, E., S. Borgani, D. Scott, and M. White, 2003, *Mon. Not. R. Astron. Soc.* **342**, 163.
- Pierpaoli, E., D. Scott, and M. White, 2001, *Mon. Not. R. Astron. Soc.* **325**, 77.
- Pinsonneault, M. H., G. Steigman, T. P. Walker, and V. K. Narayanan, 2002, *Astrophys. J.* **574**, 398.
- Press, W. H., and P. Schechter, 1974, *Astrophys. J.* **187**, 425.
- Refregier, A., 2003, *Annu. Rev. Astron. Astrophys.* **41**, 645.
- Refsdal, S., 1964, *Mon. Not. R. Astron. Soc.* **128**, 307.
- Reiprich, T. H., and H. Böhringer, 2002, *Astrophys. J.* **567**, 716.
- Renzini, A., and F. Fusi Pecci, 1988, *Annu. Rev. Astron. Astrophys.* **26**, 199.
- Rhodes, J., A. Refregier, N. R. Collins, J. P. Gardner, E. J. Groth, and R. S. Hill, 2004, *Astrophys. J.* **605**, 29.
- Riess, A. G., L. Macri, S. Casertano, M. Sosey, H. Lampeitl, H. C. Ferguson, A. V. Filippenko, S. W. Jha, W. Li, R. Chornock, and D. Sarkar, 2009, *Astrophys. J.* **699**, 539.
- Riess, A. G., *et al.*, 1998, *Astron. J.* **116**, 1009.
- Riess, A. G., *et al.*, 2004, *Astrophys. J.* **607**, 665.
- Rix, H.-W., and G. Lake, 1993, *Astrophys. J. Lett.* **417**, L1.
- Röpke, F. K., W. Hillebrandt, W. Schmidt, J. C. Niemeyer, S. I. Blinnikov, and P. A. Mazzali, 2007, *Astrophys. J.* **668**, 1132.
- Rosatì, P., S. Borgani, and C. Norman, 2002, *Annu. Rev. Astron. Astrophys.* **40**, 539.
- Sachs, R. K., and A. M. Wolfe, 1967, *Astrophys. J.* **147**, 73.
- Salaris, M., S. degl'Innocenti, and A. Weiss, 1997, *Astrophys. J.* **484**, 986.
- Salaris, M., I. Dominguez, E. Garcia-Berro, M. Hernanz, J. Isern, and R. Mochkovitch, 1997, *Astrophys. J.* **486**, 413.
- Salaris, M., and A. Weiss, 2001, *Astron. Astrophys.* **376**, 955.
- Salpeter, E. E., 1955, *Astrophys. J.* **121**, 161.
- Sandage, A., and C. Cacciari, 1990, *Astrophys. J.* **350**, 645.
- Sandage, A., and G. A. Tammann, 1974, *Astrophys. J.* **190**, 525.
- Sandage, A., G. A. Tammann, A. Saha, B. Reindl, F. D. Macchetto, and N. Panagia, 2006, *Astrophys. J.* **653**, 843.
- Schechter, P., 1976, *Astrophys. J.* **203**, 297.
- Schlegel, D. J., D. P. Finkbeiner, and M. Davis, 1998, *Astrophys. J.* **500**, 525.
- Schmidt, B. P., R. P. Kirshner, and R. G. Eastman, 1992, *Astrophys. J.* **395**, 366.
- Schneider, P., J. Ehlers, and E. E. Falco, 1992, *Gravitational Lenses* (Springer-Verlag, Berlin), Vol. XIV, p. 112.
- Scranton, R., *et al.*, 2005, *Astrophys. J.* **633**, 589.
- Seljak, U., 2002, *Mon. Not. R. Astron. Soc.* **337**, 769.
- Seljak, U., and M. Zaldarriaga, 1996, *Astrophys. J.* **469**, 437.
- Seljak, U., and M. Zaldarriaga, 1997, *Phys. Rev. Lett.* **78**, 2054.
- Semboloni, E., Y. Mellier, L. van Waerbeke, H. Hoekstra, I. Tereno, K. Benabed, S. D. J. Gwyn, L. Fu, M. J. Hudson, R. Maoli, and L. C. Parker, 2006, *Astron. Astrophys.* **452**, 51.
- Sheth, R. K., and G. Tormen, 2002, *Mon. Not. R. Astron. Soc.* **329**, 61.
- Silk, J., 1968, *Astrophys. J.* **151**, 459.
- Simon, P., M. Hettterscheidt, M. Schirmer, T. Erben, P. Schneider, C. Wolf, and K. Meisenheimer, 2007, *Astron. Astrophys.* **461**, 861.
- Slipher, V. M., 1927, *Publ. Astron. Soc. Pac.* **39**, 143.
- Smith, G. P., A. C. Edge, V. R. Eke, R. C. Nichol, I. Smail, and J.-P. Kneib, 2003, *Astrophys. J. Lett.* **590**, L79.
- Smith, R. E., J. A. Peacock, A. Jenkins, S. D. M. White, C. S. Frenk, F. R. Pearce, P. A. Thomas, G. Efstathiou, and H. M. P. Couchman, 2003, *Mon. Not. R. Astron. Soc.* **341**, 1311.
- Sofue, Y., and V. Rubin, 2001, *Annu. Rev. Astron. Astrophys.* **39**, 137.
- Spergel, D. N., *et al.*, 2007, *Astrophys. J., Suppl. Ser.* **170**, 377.
- Spite, F., and M. Spite, 1982, *Astron. Astrophys.* **115**, 357.
- Springel, V., and L. Hernquist, 2002, *Mon. Not. R. Astron. Soc.* **333**, 649.
- Springel, V., *et al.*, 2005, *Nature (London)* **435**, 629.
- Steigman, G., 2007, *Annu. Rev. Nucl. Part. Sci.* **57**, 463.
- Steigman, G., D. N. Schramm, and J. E. Gunn, 1977, *Phys.*

- Lett. B **66**, 202.
- Steigman, G., and T. P. Walker, 1992, *Astrophys. J. Lett.* **385**, L13.
- Straniero, O., and A. Chieffi, 1991, *Astrophys. J., Suppl. Ser.* **76**, 525.
- Sunyaev, R. A., and Y. B. Zeldovich, 1970, *Astrophys. Space Sci.* **7**, 3.
- Sunyaev, R. A., and Y. B. Zeldovich, 1972, *Comments Astrophys. Space Phys.* **4**, 173.
- Tauber, J. A., 2004, *Adv. Space Res.* **34**, 491.
- Tegmark, M., *et al.*, 2004, *Astrophys. J.* **606**, 702.
- Toffolatti, L., F. Argueso Gomez, G. de Zotti, P. Mazzei, A. Franceschini, L. Danese, and C. Burigana, 1998, *Mon. Not. R. Astron. Soc.* **297**, 117.
- Tonry, J., and D. P. Schneider, 1988, *Astron. J.* **96**, 807.
- Tonry, J. L., J. P. Blakeslee, E. A. Ajhar, and A. Dressler, 1997, *Astrophys. J.* **475**, 399.
- Tonry, J. L., J. P. Blakeslee, E. A. Ajhar, and A. Dressler, 2000, *Astrophys. J.* **530**, 625.
- Truran, J. W., W. D. Arnett, and A. G. W. Cameron, 1967, *Can. J. Phys.* **45**, 2315.
- Tully, R. B., and J. R. Fisher, 1977, *Astron. Astrophys.* **54**, 661.
- Udalski, A., M. Szymanski, M. Kubiak, G. Pietrzynski, I. Soszynski, P. Wozniak, and K. Zebrun, 1999, *Acta Astron.* **49**, 201.
- Uson, J. M., and D. T. Wilkinson, 1984, *Astrophys. J., Lett. Ed.* **277**, L1.
- Valenziano, L., *et al.*, 2007, *New Astron. Rev.* **51**, 287.
- Van Waerbeke, L., Y. Mellier, and H. Hoekstra, 2005, *Astron. Astrophys.* **429**, 75.
- VandenBerg, D. A., 1983, *Astrophys. J., Suppl. Ser.* **51**, 29.
- VandenBerg, D. A., 2000, *Astrophys. J., Suppl. Ser.* **129**, 315.
- Viel, M., G. D. Becker, J. S. Bolton, M. G. Haehnelt, M. Rauch, and W. L. W. Sargent, 2008, *Phys. Rev. Lett.* **100**, 041304.
- Viel, M., and M. G. Haehnelt, 2006, *Mon. Not. R. Astron. Soc.* **365**, 231.
- Viel, M., J. Weller, and M. G. Haehnelt, 2004, *Mon. Not. R. Astron. Soc.* **355**, L23.
- Wambsganss, J., and B. Paczynski, 1992, *Astrophys. J. Lett.* **397**, L1.
- Wang, X., M. Tegmark, B. Jain, and M. Zaldarriaga, 2003, *Phys. Rev. D* **68**, 123001.
- Wasserburg, G. J., F. Tera, D. A. Papanastassiou, and J. C. Huneke, 1977, *Earth Planet. Sci. Lett.* **35**, 294.
- Weinberg, S., 2008, *Cosmology* (Oxford University Press, New York).
- Wesselink, A. J., 1946, *Bull. Astron. Inst. Neth.* **10**, 91.
- Wetterich, C., 1988, *Nucl. Phys. B* **302**, 668.
- White, S. D. M., C. S. Frenk, M. Davis, and G. Efstathiou, 1987, *Astrophys. J.* **313**, 505.
- White, S. D. M., J. F. Navarro, A. E. Evrard, and C. S. Frenk, 1993, *Nature (London)* **366**, 429.
- Woosley, S. E., A. Heger, and T. A. Weaver, 2002, *Rev. Mod. Phys.* **74**, 1015.
- Yang, J., M. S. Turner, D. N. Schramm, G. Steigman, and K. A. Olive, 1984, *Astrophys. J.* **281**, 493.
- York, D. G., *et al.*, 2000, *Astron. J.* **120**, 1579.
- Zaldarriaga, M., 1997, *Phys. Rev. D* **55**, 1822.
- Zaroubi, S., M. Viel, A. Nusser, M. Haehnelt, and T.-S. Kim, 2006, *Mon. Not. R. Astron. Soc.* **369**, 734.
- Zel'dovich, Y. B., 1970, *Astron. Astrophys.* **5**, 84.
- Zeldovich, Y. B., 1972, *Mon. Not. R. Astron. Soc.* **160**, 1P.
- Zlatev, I., L. Wang, and P. J. Steinhardt, 1999, *Phys. Rev. Lett.* **82**, 896.
- Zwicky, F., 1933, *Helv. Phys. Acta* **6**, 110.
- Zwicky, F., 1937, *Astrophys. J.* **86**, 217.